ON THE TRANSMISSION OF FLUID FORCES TO THE ACTIN CYTOSKELETON OF BONE AND ENDOTHELIAL CELLS

by

YUEFENG HAN

A dissertation submitted to the Graduate Faculty in Engineering

in partial fulfillment of the requirements for the degree of

Doctor of Philosophy, The City University of New York

2006

This manuscript has been read and accepted for the
Graduate Faculty in Engineering in satisfaction of the
dissertation requirements for the degree of Doctor of Philosophy.

Date	Dr. Sheldon Weinbaum Chair of Examining Committee
Date	Dr. Mumtaz Kassir Executive Officer

Dr. Stephan C. Cowin

Dr. Susannah P. Fritton

Dr. Mitchell B. Schaffler

Dr. Bingmei Fu
Supervisory Committee

THE CITY UNIVERSITY OF NEW YORK

Abstract

ON THE TRANSMISSION OF FLUID FORCES TO

THE ACTIN CYTOSKELETON OF BONE

AND ENDOTHELIAL CELLS

by

Yuefeng Han

Mentor: Professor Sheldon Weinbaum

Co-mentors**:** Professor Stephen C. Cowin and Professor Mitchell B. Schaffler

This dissertation studies how hydrodynamic forces are transmitted across the membranes of endothelial cells and bone cells (osteocytes) via extracellular matrices. Firstly, I apply large deformation theory for 'elastica' to describe the restoration of the core protein fibers in the endothelial glycocalyx (EG) after being matted by the passage of a white blood cell. By matching the predicted time-dependent thickness of the EG with experiments I obtain an estimate of 490 $pN \bullet nm^2$ for the flexural rigidity of the core protein fibers. Thus, the EG is sufficiently stiff to function as a mechanotransducer. The core proteins are also barely deflected by the physiological motion of red blood cells (RBCs). In contrast, arrested RBCs crush the EG and the viscous draining resistance of the EG layer is essential for preventing adhesive intercellular interactions between endothelial cells and RBCs. Secondly, I model the response of the EG to steady or oscillating shear applied at its edge, and extend this

analysis to apply to the microvilli and cilia on kidney cells. In the case of oscillating shear, I find that the motions of both the fluid and structural elements, including the EG and microvilli and cilia on kidney cells, are in a quasi-steady state at physiological conditions. Thirdly, I develop a realistic 3-D structural model for the core actin bundle in osteocytic processes, and greatly refine the strain amplification model for bone mechanotransduction proposed by You et al. (2001, J. Biomech. **34**: 1375). The new model predicts a cell process that is 3 times stiffer than You et al. (2001), but hoop strains > 0.5 percent for tissue level strains > 1000 μ strain at 1 Hz and > 250 μ strain at frequencies > 10 Hz. This strain amplification model provides a more likely hypothesis for the excitation of osteocytes than the fluid shear hypothesis previously proposed in Weinbaum et al. (1994, J. Biomech. **27:** 339). Finally, I study the fluorescence uptake by osteocyte-like MLO-Y4 cells incubated with agonists and antagonists to purinergic $P2X_7$ receptors. The results suggest the involvement of $P2X_7$ receptors in the signaling pathway for the mechanotransduction of osteocytes.

Acknowledgements

I gratefully acknowledge the guidance, care, and support of my "academic father" Dr. Sheldon Weinbaum. Furthermore, I truly appreciate his pains-taking efforts to correct and improve my writing. Dr. Weinbaum has greatly inspired me with his magical and insightful intuition. I am similarly grateful to my co-mentors ("academic uncles") Dr. Stephen C. Cowin and Dr. Mitchell B. Schaffler for their insightful advising.

I express my gratitude to Dr. Susannah P. Fritton and Dr. Bingmei Fu. Dr. Frittion recruited me to the bone journal club and has shown me an extensive view of the field of bone. Dr. Fu has supported and helped me in many ways, and her big-sister-like warmth is precious to me.

I also want to express my gratitude to Dr. David C. Spray for advising me in experiments. In addition, I want to thank Dr. Mia M. Thi for her tutorship and collaboration in the experimental studies. I also appreciate the help from all other colleagues in the laboratory of Dr. Spray at Albert Einstein School of Medicine.

Likewise, I want to thank Dr. John Tarbell for his generosity to allow me to work in his lab for several months. I also appreciate the help from all of his students especially Jeff S. Garanich, Limary M. Cancel, and Zhongdong Shi.

I would like to thank all other current students in Dr. Weinbaum's lab: Chi Bang, Yi Duan, Yulia Vengrenyuk, Yilin Wang, and Danielle Wu. The experiences with

them are the fun part of my study at CCNY. I also want to thank Dr. Weinbaum's previous students Dr. Qianhong Wu and Dr. Xiaobing Zhang. They made me feel so comfortable when I first joined the lab in January, 2003.

Last but not least, I want to thank Carol Bamberger and Patricia Cupid for their administrative help. Most importantly, they have reminded me innumerable times to complete my timesheets so that I could get my paychecks on time.

Table of Contents

List of Tables

Chapter 3

Chapter 4

Chapter 5

List of Figures

Chapter 1

Chapter 2

Chapter 3

Chapter 4

Chapter 5

Chapter 6

Appendix B

Chapter 1 Introduction

In this dissertation I will study how fluid forces are transmitted by extracellular matrices across the membranes of endothelial cells and bone cells (osteocytes). In particular, I will examine the role of the endothelial glycocalyx in detecting fluid shear and the role of pericellular matrix in producing strain amplification in osteocytic processes.

The endothelial glycocalyx (EG) is a layer of glycoproteins and proteoglycans on the luminal surface of endothelial cells (ECs) in both large arteries (Luft 1966) and microvessels (Vink and Duling 1996). Its multifaceted roles as a transport barrier (Michel 1997; Hu et al. 2000), a porous hydrodynamic interface in the motion of red and white blood cells in microvessels (Feng and Weinbaum 2000; Zhao, Chien and Weinbaum 2001), and a mechanotransducer of fluid shear stress to the actin cortical cytoskeleton (ACC) of the endothelial cell (Weinbaum et al. 2003) are widely recognized. Squire et al. (2001) were able to identify for the first time the quasi-periodic substructure of the EG and its anchoring foci that appear to emanate from the underlying cytoskeleton. The possible existence of an ordered structure had been proposed eighteen years earlier (Michel 1983). Weinbaum et al. (2003) developed this structural model into an idealized mathematical model to explain how the core protein fibers in the endothelial glycocalyx transmit fluid shear to the ACC of ECs and show how the force is amplified if the glycocalyx fibers act as cantilever beams. This idealized model is adapted and shown in Fig. **1-1**. Florian et al. (2003) experimentally demonstrated that enzymatic degradation of heparan sulfate proteoglycan, a major

component of the endothelial glycocalyx, completely inhibits the production of NO by ECs in response to both steady and oscillatory fluid shear. Thi et al. (2004) show that if the glycocalyx is compromised there is no reorganization of the actin cytoskeleton and associated molecules, such as vinculin, in response to fluid shear stresses for durations of up to five hours. This is in sharp contrast to the behavior observed for an intact glycocalyx at the same fluid shear stresses where marked cytoskeleton reorganization is routinely seen.

The endothelial glycocalyx fibers must be sufficiently stiff to perform the mechanotransduction role proposed by Weinbaum et al. (2003). However, very little is known about the mechanical properties of the glycocalyx or the flexural rigidity, *EI*, of the core proteins that comprise it. In an abstract Vink et al. (1999) measured the time-dependent restoration of the endothelial glycocalyx after it is nearly completely compressed by the passage of a WBC in a tightly fitting capillary. This experiment is described in more detail in Chapter 2 and will appear in Han et al. (2006). Using the characteristic time for the restoration measured in this experiment, Weinbaum et al. (2003) predicted that the core proteins have a flexural rigidity EI of 700 $pN{\cdot}nm^2$, which is ~ 1/20 the measured value for an actin filament. However, their analysis assumes small deflections and only the fiber motion is considered. In Chapter 2, I will apply large deformation theory for 'elastica' to describe the restoration of the core protein fibers in a Brinkman medium which imbibes fluid as the endothelial glycocalyx expands. I find that there are two phases in the fiber recoil, an initial phase for large compressions where the EG thickness is < 0.361 its undisturbed thickness, and the ends of the fibers are matted and parallel to the capillary wall, and a second

phase where the fibers assume a shape that is close to the solutions for an elastic bar with linearly distributed vertical loading. The predicted time dependent change in thickness of the endothelial glycocalyx provides remarkably good agreement with experiment and yields an estimate of 490 pN•nm^2 for the flexural rigidity EI of the core protein fibers, which is unexpectedly close to that predicted by the linear theory in Weinbaum et al. (2003). In Chapter 3, I will model the hydrodynamic interactions between the EG and red blood cells when RBCs either glide above the layer when their velocity is > 20 μm/s, or compress the layer when they are brought to rest. I find that the physiological motion of the RBC at a fluid shear stress of 10 dyn/cm^2 induces a small deflection (< 10 nm for an EG of 400nm thickness), which is comparable to the deflection induced by plasma at the same physiological shear stresse. I also find that the viscous draining resistance of the matrix is essential for preventing adhesive molecular interactions between proteins in the endothelial membrane and RBC membrane when RBCs are temporarily brought to rest and crush the EG during intermittency, the periodic stopping and starting of flow in capillary beds.

Some sites in arteries, such as the inner walls of arterial curvature and outer walls of arterial bifurcations (side opposite to the flow divider), experience significant oscillations in shear stress and are more likely to develop atherosclerotic plaques (Ku et al. 1985; Qiu and Tarbell 2000). Moreover, one might be interested in *in vitro* experiments to explore the response of endothelial cells to oscillating fluid shear on their apical surface. Thus, in Chapter 4 I will examine the response of the EG to steady or oscillating shear applied at its outer edge, and extend this analysis to apply to the microvilli and cilia in kidney cells. These cellular protuberances have also been

proposed to play a mechanotransduction role (Guo et al. 2000; Praetorius and Spring 2001; Liu et al. 2003; Du et al. 2004). In the case of oscillating shear, I find that the motions of both the fluid and structural elements, including the EG and microvilli and cilia on kidney cells, are in a quasi-steady state at physiological conditions. No attenuation or phase shift of the torque is induced by the hydrodynamic drag when the applied frequency $\omega < \omega_c$ or ω_r ($= \omega/\omega_c$) <1. Here $\omega_c = \frac{c}{\pi} \frac{EI}{\mu r_f^2 L^2}$ is the natural frequency for the damped vibration of the structural element.

Bone shows remarkable capabilities in modeling and remodeling in response to mechanical loading and it is believed that osteocytes embedded in bone matrix play a mechanosensory role. Thus, it is of great interest to elucidate how osteocytes sense mechanical loading on bone since bone is such a rigid tissue. Its physiological strain is less than 0.2 percent (Fritton, Mcleod and Rubin 2000), which is not sufficient to stimulate bone cells grown on an elastic substrate (You et al. 2000). Weinbaum et al. (1994) used Biot's theory to predict that the fluid shear on the processes of osteocytes is 10-30 dyn/cm^2, the same scale as the fluid shear measured *in vivo* on endothelial cells, and proposed that fluid shear on the cell processes stimulates osteocytes to respond to tissue loading. Numerous *in vitro* experiments have been conducted, which show that osteocytes and osteoblasts respond to fluid shear by release of various second messengers and expression of various genes (Reich and Frangos 1991, Williams et al. 1994, Huang et al. 1995, Klein-Nulend et al. 1997). However, the model in You et al. (2001) predicted that the cell process has a Young's modulus at least two orders of magnitude greater than the cell body. This suggests that the cellular responses observed in the cell cultures must have been due to fluid shear on the much

softer cell bodies. In contrast, *in vivo* the cell bodies experience very small shear stresses since the pericellular space surrounding the cell body in its lacuna is an order of magnitude thicker than the pericellular matrix surrounding cell processes in their canaliculi.

To resolve this paradox You et al. (2001) proposed a new hypothesis and a quantitative intracellular model (adapted and shown in Fig. **1-2**) which predicts that the fluid flow through the pericellular matrix in the lacunar-canlicular porosity due to small whole tissue deformations can induce cellular-level strains in the actin filament bundles of the cell process, which are greatly amplified and sufficient to initiate intracellular signaling. However, when the model was proposed the mechanical properties of the tethering element shown in Fig. **1-2** were unknown and there was only fragmentary or even contradictory evidence as to the key structural components of the osteocytes in the model. In chapter 5 I will refine this strain amplification model using new geometric measurements in You et al. (2004) and the first theoretical estimates of the flexural rigidity of core protein fibers (Weinbaum et al. 2003) for the transverse elements. More importantly, I will construct a more realistic 3-D model for the cell process by using the similarity between the 3-D cytoskeletal organization of the osteocytic process and intestinal microvilli. The new model predicts a cell process that is 3 times stiffer than You et al. (2001), but hoop strains > 0.5 percent for tissue level strains > 1000 μ strain at 1 Hz and > 250 μ strain at frequencies > 10 Hz. These results explain the mystery reported in Rubin and Lanyon (1985) that dynamic tissue strains at 1 Hz with amplitudes ≥ 1000 μ strain induce new bone formation while tissue strains at 1 Hz with amplitudes < 1000 μ strain lead to bone loss, since

osteocytes can not be excited by cellular strains < 0.5 percent (You et al. 2000). This strain amplification model provides a more likely hypothesis for the excitation of osteocytes than the fluid shear hypothesis previously proposed in Weinbaum et al. (1994).

Recent *in vitro* studies suggest that some membrane channels open in response to fluid shearing and this opening allows for the release of certain small molecules, such as ATP and PGE_2, which initiates a further cellular signaling cascade in an autocrine manner. In chapter 6 I will treat osteocyte-like MLO-Y4 cells with typical agonists and antagonists to hemichannels and purinergic P2X receptors, possible candidates for the putative channels, and monitor the opening of these channels by measuring cellular fluorescence uptake. The results show that ATP enhances the cellular fluorescence uptake by opening $P2X_7$ receptors and this enhancement can be negated after the cells are incubated with 10 μM of 1-[N,O-Bis(5-isoquinolinesulfonyl)-N-methyl-L-tyrosyl]-4-phenylpiperazine (KN-62) or brilliant blue G (BBG), antagonists to $P2X_7$ receptors.

Footnotes: Chapters 2-5 are reprinted with permission from my journal papers and are copyrighted by the journals. See the footnotes in each of these chapters for detailed information.

Chapter 2 Large Deformation Analysis of the Elastic Recoil of the core protein in the Endothelial Glycocalyx

2.1. Introduction

The problem of the elastohydrodynamic recoil of a matted layer of initially uniform vertical fibers in a viscous fluid arises in many contexts from the stroking of fur, to the motion of the bristles of a soft brush, to the recoil of the endothelial glycocalyx after the passage of a white blood cell (WBC) in a tightly fitting capillary, the motivation for the present study. The motion of a periodic array of vertical fibers in a plane wall has been studied in a variety of biological applications. Some prominent applications include beating cilia (Liron and Shahar 1978), the flow past brush border microvilli in the proximal tubule (Guo, Weinstein and Weinbaum 2000), cilia in the cortical collecting duct (Liu et al. 2003), and the transmission of fluid shear stress by core proteins comprising the glycocalyx that forms the endothelial surface layer (ESL) (Secomb, Hsu and Pries 2001; Weinbaum et al. 2003). Beating cilia in a channel have been treated using Liron's extension (Liron and Mochon 1976; Liron and Shahar 1978) of Blake's singularity (Blake 1971) for the motion of a Stokeslet near a planar boundary. Since beating cilia is an active process in which the motion is prescribed, one does not need to consider their passive elastohydrodynamic response. In contrast, in problems involving mechanotransduction, such as the flow past brush border microvilli, or primary cilia in the cortical collecting duct, or core proteins in the ESL, the deformation of these cellular protuberances or molecular fibers plays a critical role since it is related to the deformation of the intracellular cytoskeleton and, hence, intracellular signaling.

The fluid flow in the three mechanotransduction problems mentioned above has been examined using effective medium theory (Brinkman equation) and the deformations determined using a theory for the small deflections of a cantilever beam (Gere and Timoshenko 1990). These latter analyses employ the solutions of Sangani and Acrivos (1982) for the local Stokes flow past a two-dimensional hexagonal array of circular cylinders to first determine the local hydrodynamic loading on the protuberances or fibers and then use this loading to determine their deflection. There is no motion of the fibers in these analyses since the external flow is steady and the deformation is constant. These steady flow analyses were recently extended to treat the elastohydrodynamic response of the fibers in a time dependent oscillating flow where the relative motion of the fibers and the fluid is considered (Han, Ganatos and Weinbaum 2005). This theory was limited to small fiber deformations.

A problem that has attracted widespread attention is the role of the ESL in transmitting fluid shear stress due to the flowing blood to the intracellular cytoskeleton of the endothelial cell. This problem raises a fundamental paradox since it is generally agreed that the flow within the ESL is negligible and the shear stress at the level of the cell membrane vanishingly small (Damiano 1998; Feng and Weinbaum 2000; Secomb, Hsu and Pries 1998; Secomb, Hsu and Pries 2001; Weinbaum et al. 2003). Various models have been proposed to explain the mechanism via which the shear stress is transmitted to either the cell membrane or the cell's actin cytoskeleton and why the ESL maintains its structural rigidity under flow (Damiano and Stace 2002; Secomb et al. 2001; Weinbaum, et al. 2003). Secomb et al. (2001) propose that its structural integrity arises from an oncotic force due to trapped plasma proteins. Damiano and

Stace (2002) suggest that this is due to electrochemical effects associated with the negative charge on the glycosaminoglycans (GAG) of the glycocalyx. Weinbaum et al. (2003) propose that it arises from the flexural rigidity EI of the core proteins of the ESL. The merits and deficiencies of each model are summarized at the end of the chapter.

While the existence of the ESL and the first measurements of its thickness *in vivo* were obtained in Vink and Duling (1996), the three-dimensional structural organization of the ESL was not realized till Squire et al. (2001) were able to identify for the first time the quasi-periodic substructure of the glycocalyx and its anchoring foci. The latter appear to emanate from the underlying actin cortical scaffold beneath the membrane which takes the form of an ordered hexagonal array. The model proposed in Squire et al. (2001) was developed into an idealized mathematical model in Weinbaum et al. (2003). This idealized model with its characteristic dimensions is shown in Fig. **1-1**. The basic structural elements of the ESL are assumed to be the core proteins of proteoglycans, the most likely candidate being syndecan I, a transmembrane heparin sulphate proteoglycan (Mulivor and Lipowsky 2004). Hyaluronan and chondroitin sulphate also play an important role in its assembly and sieving properties (Henry and Duling 2000). Recent studies have shown that the primary functions of the ESL are not only to protect the endothelium, but also to serve as a mechanotransducer of fluid shear (Weinbaum et al. 2003, Thi et al. 2004) and a molecular sieve for plasma proteins (Michel 1997, Weinbaum 1998, Hu et al. 2000, Adamson et al. 2004). A review of the state of knowledge of the ESL, its properties and function as of 2000 is given in Pries et al. (2000).

Very little is known about the mechanical properties of the glycocalyx or the flexural rigidity, *EI*, of the core proteins that comprise it. However, Vink et al. (1999) reported an initial experiment from which these properties can be deduced with the aid of a mathematical model. This experiment, which was published as an abstract, is described in detail in Han et al. (2006). In the experiment one measures the time dependent restoration of the ESL after it is nearly completely compressed by the passage of a WBC in a tightly fitting capillary. This restoration is estimated by measuring the gap between the endothelial cell (EC) membrane and the membranes of red blood cells (RBCs) that follow at different distances in the wake of the WBC. Figure **2-1(a)** shows an microscopic image of a transilluminated hamster muscle capillary illustrating the measurement of RBC-EC gaps, and figure **2-1(b)** shows the RBC-EC gap recovery as a function of time after passage of a WBC through a capillary with a diameter of 4.4 μm. One finds that the characteristic time for the restoration is approximately 0.4 s. Damiano and Stace (2002) and Weinbaum et al. (2003) have both attempted to predict this characteristic time using either an electrochemical or elastic mechanism for the recoil of the crushed ESL. The elastic model in Weinbaum et al. (2003), which is the catalyst for the present study, predicts that two characteristic times describe the recoil, a short time associated with the relaxation of the initial shape of the core proteins after their compression, and a long time behavior associated with the final phase of the motion. EI is determined by requiring that the latter time match the measured value 0.4 s required for the ESL to return to its initial undisturbed thickness. Using a time dependent beam equation for

small deflections, in which the local force on the fiber is proportional to its local instantaneous velocity, one predicts that the core proteins have a flexural rigidity EI of 700 pN•nm^2. This is about 1/20 the measured value for an actin filament, the structural element beneath the membrane that anchors the bush-like core protein structure, see Fig. **1-1**.

The foregoing linear analysis in Weinbaum et al. (2003) was intended only as a rough guide for predicting EI. The large initial deformations of the core proteins lie far outside the range of validity of small deflection theory used in their analysis and the fibers were assumed to recoil in a stagnant fluid. No attempt was made to predict the time dependent change in shape of the fibers during their recoil. Furthermore, the analysis in Han et al. (2005) shows that the motion of the fibers induces a motion of comparable magnitude in the fluid in planes parallel to the membrane and the latter was neglected in Weinbaum et al. (2003). In the present paper a more sophisticated non-linear analysis is attempted which is a more realistic representation of the mechanics of the fluid and fiber motion. Large deformation theory for 'elastica' is applied to describe the time dependent motion of the fibers and their changing shape. In addition, the fluid flows in directions both normal and parallel to the wall are considered. The flow normal to the wall is of special interest since the displaced volume occupied by the fibers induces a normal velocity that entrains fluid into the fiber layer as the fibers recoil and the solid fraction decreases. The flow in the direction parallel to the wall is very similar to the analysis in Han et al. (2005). There is very little relative motion of fluid and fiber in this direction except for a thin fiber interaction layer near the edge of the glycocalyx. One finds that there are two phases

in the fiber recoil, an initial phase for large compressions where the glycocalyx thickness is < 0.361 of its uncompressed state and the ends of the fibers overlap and a second phase where the fibers assume a shape that is very similar to the well known solutions for an 'elastica' with a linearly varying load. Using this model for large deformation, we also predict the time-dependent change in shape of the glycocalyx fibers during the recovery of ESL.

The body of this chapter will be divided into four sections, a methods and results section describing the experiments for the glycocalyx recoil, a theoretical section describing the formulation and solution of the non-linear, large deformation equations for the time dependent change in the shape of the fibers, a results section comparing theory and experiment and a discussion section which will explore the plausibility of various mechanisms that have been proposed for the glycocalyx recoil.

2.2. Mathematical model

RBCs produce a slow draining of the ESL when brought to rest, with a characteristic draining time of 0.5 s (Weinbaum et al. 2003), and gradually rise through the ESL as their velocity increases when flow is started again. In contrast, WBCs are much stiffer, in view of their nuclei and cytoskeletal organelles and, as observed in Fig. **2-1**, the initial compression of the ESL by the passing WBC is nearly instantaneous and independent of its velocity. The mechano-electrochemical model in Damiano and Stace (2002) and the elastic recoil model in Weinbaum et al. (2003) were largely concerned with predicting the characteristic time for this restoration and not the detailed time dependent change in the shape of the fibers during their recoil. It

is also clear from the observed structure of the ESL (Squire et al. 2001), and the size of the scattering centers along the core proteins depicted in Fig. **1-1**, that the volume fraction of the solid matrix could approach near close packing for the very large deformations observed in Fig. **2-1(b)**. These observations suggest that a realistic model needs to include both the changing solid fraction c of the expanding glycocalyx and realistic shapes of the core proteins from the initial passage of the WBC till the final restoration of the ESL. Thus, the formulation of the theoretical model is divided into two major subsections, a model for the fluid flow and a model for the instantaneous fiber or core protein shape. The fluid flow model must take account of both the instantaneous x and y components of the velocity of the fluid and the recoiling core proteins and the changing solid fraction, the latter at least in a time average sense. This changing value of c provides a source term for entraining fluid and, thus, adds to the drag on the fibers. The fiber model exploits a realistic family of shapes obtained from known solutions to the 'elastica' equations and simple experiments where the qualitative shape of an 'elastica' is observed when a flat planar surface moves over the fiber.

2.2.1. Model for the fluid

The fluid flow in the recoiling fiber layer is modeled as a flow in a porous medium with an average time dependent solid fraction *c*, as shown in Fig. **2-2**. Physiologically, there is a pressure gradient in the x direction. However, the velocity it generates is < 10 nm/s in the interior of the ESL for the fiber geometry depicted in Fig. **1-1**, and thus negligible compared to the fiber recoil velocity. Furthermore, the fluid

flow varies slowly in the x direction. Thus, we will neglect the pressure gradient in the x direction and the first and second derivatives of the fluid velocities with respect to x in the continuity equation and the Brinkman equation describing the fluid fiber momentum balance. The continuity equation contains a source term with a time varying solid fraction,

$$\frac{\partial(1-c)}{\partial t}+\frac{\partial u_y}{\partial y}=0 \qquad \textbf{[2-1]}$$

Here u_x and u_y are the fluid velocity components in the x and y directions, respectively, and c is the instantaneous average solid fraction of the ESL. The uncompressed ESL has a solid fraction of 0.16 using a structural model with 12 nm diameter spherical scattering centers spaced at 20 nm intervals along the axes of the core proteins as shown in Fig. **1-1**. The inertia of the fluid is negligible. The governing Brinkman equations for the fluid motion, which take account of the quasi-steady relative motion of the fluid and the fibers in the x and y directions, are

$$u_x-\frac{\partial \nu_x}{\partial t}=K_{Px}\frac{\partial^2 u_x}{\partial y^2}, \qquad \textbf{[2-2]}$$

and

$$\frac{\partial P}{\partial y}=\mu\frac{\partial^2 u_y}{\partial y^2}-\frac{\mu}{K_{Py}}\left(u_y+\frac{\partial \nu_y}{\partial t}\right). \qquad \textbf{[2-3]}$$

Here P is the fluid pressure, μ is the fluid viscosity, K_{Px} and K_{Py} are Darcy's permeability of the ESL in the x and y directions, respectively, and ν_x and ν_y are the fiber deflections in the positive x and negative y directions, respectively, and are functions of x, y and t. The applicability of using a Bringkman to describe the fluid motion in the ESL is described at length in Damiano et al. (1996) and Feng, Ganatos

and Weinbaum (1998). Despite its limitation in describing the transition from a Darcy flow in the interior of the ESL to a steady laminar flow outside this layer, it has been used in nearly all recent theoretical studies of this layer. As we shall show shortly, the transition layer is of little importance in the present study and the viscous term can be dropped.

The solid mass is conserved throughout the fiber recoil process. Thus,

$$c = \frac{c_o h_o}{h}, \qquad \textbf{[2-4]}$$

where h is the instantaneous ESL thickness, and c_o and h_o are the uncompressed solid fraction and thickness. Note that Eq. **2-4** neglects the local variation of c as a function of y. The instantaneous solid fraction, c, is treated as an average value for the entire ESL that satisfies the global mass balance for the layer. This approximation greatly simplifies the analysis. Combining Eqs. **2-1** and **2-4**, one obtains

$$u_y = y \cdot \frac{dc}{dt} = -\frac{y c_o h_o}{h^2}\frac{dh}{dt} \qquad \textbf{[2-5]}$$

In Eq. **2-2**, the characteristic length l_c is the uncompressed ESL thickness, 400 nm, and the characteristic velocity in the x direction for both the fluid and the fiber tip is the fluid velocity at the ESL edge. Thus, the term, $K_P \frac{\partial^2 u_x}{\partial y^2}$, in Eq. **2-2** has a scale of K_P / l_c^2 , ~ 10^{-4} since the Darcy's permeability, K_P, of the undeformed ESL is 3.16 nm^2 (Han et al. 2005; Weinbaum et al. 2003). Thus, equation **2-2** can be rewritten as

$$u_x = \frac{\partial v_x}{\partial t} \qquad \textbf{[2-6]}$$

except for a thin tip interaction layer at the edge of the ESL where the higher order derivative term $K_P \frac{\partial^2 u_x}{\partial y^2}$ is required to describe the flow-transition at the ESL edge. The solutions in (Han et al. 2005; Weinbaum et al. 2003) show that this slip velocity is typically a few μm/s when the fluid shear stress at the ESL edge is 10 dyn/cm^2. In the present application this shear stress is much smaller due to the slow velocity of the WBC. In the interior of the fiber layer the fluid flow induced by the edge velocity is negligible. In contrast, the fluid flow induced by the fiber motion is dominant. Thus, equation **2-6** is a good approximation except for the tip interaction boundary layer at the outer edge of the ESL which is described in Guo et al. (2000) and Han et al. (2005). Substituting Eq. **2-5** into Eq. **2-3**, one obtains

$$\frac{\partial P}{\partial y} = \frac{\mu}{K_P}\left(\frac{\partial v_y}{\partial t} - \frac{y c_o h_o}{h^2}\frac{dh}{dt}\right). \qquad \textbf{[2-7]}$$

Equations **2-5~2-7** define the fluid velocity and pressure field except for the tip interaction layer. Both fields depend on the instantaneous ESL thickness h(t), its velocity dh/dt and the local components of the fiber velocity, $\partial v_x/\partial t$ and $\partial v_y/\partial t$.

2.2.2. Time - Dependent Fiber Recoil

Figure **2-3** shows our two-phase fiber recoil model schematically. As alluded to earlier the qualitative shape of a deformed fiber after the passage of a WBC can be deduced from simple experiments in which a planar boundary is passed at different heights over a thin vertical elastic strip rigidly anchored at its base. One finds that the strip takes the shape of an ‘elastica’ that is loaded at its tip up until the point of contact with the planar boundary and that from there to the end of the strip, the strip is parallel

to the planar surface. This is the initial assumed shape of the fibers after the passage of the WBC. In phase I it is assumed that the fibers recoil through a family of shapes which have this same basic geometry with the location of the zero slope shifting towards the end of the fiber as it rises (dashed lines $d\mathrm{v}_y/dx = 0$ in Fig. **2-3**). With closely spaced fibers that overlap near their top surface this geometry is quite realistic. At the transition point at the end of phase I ($h=h_t$), the slope of the fiber at its tip is horizontal. In phase II, the slope at the fiber tip continues to increase as the fiber recoils back to its original upright shape from the transition point.

Hydrodynamic loads on the core protein fiber: The fluid drag force on the core protein fiber is proportional to the relative velocity between the fluid and the fibers. However, equation **2-6** shows that there is no relative velocity in the *x* direction except in the tip boundary layer, which we neglect. Furthermore, the solutions in Han et al. (2005) and Weinbaum et al. (2003) show that the fluid shear stress at the ESL edge causes a very small deflection of the core protein fibers compared to the large deformation caused by the passage of the WBC in the present analysis. This small deflection describes the final steady state after the fiber recoil is completed. In contrast, there is a substantial relative velocity in the y direction between the fluid and fibers due to the entraining effect of the recoiling fiber layer and the fact that the fiber is moving upward relative to the fluid whose normal velocity vanishes at y = 0. The relative motion of the fluid and the fibers is, therefore, much greater in the y direction as opposed to the x direction and the latter can be neglected. We decompose the drag force due to the relative motion in the y direction into force components normal, n, and tangential, t, to the local fiber direction since the drag coefficients or the Darcy

permeability differ for flow normal and tangential to the fibers. We write the drag force in vector form as

$$\vec{f} = \{f_n, f_t\} = \mu \cdot \frac{\pi}{c} \cdot r^2 \cdot \left(u_y + \frac{\partial v_y}{\partial t} \right) \left\{ \frac{\cos\theta}{K_{Pn}}, \frac{\sin\theta}{K_{Pt}} \right\} \qquad \textbf{[2-8]}$$

Here θ is the local tangential angle of the fiber and K_{Pn}, K_{Pt} are the Darcy permeability for the flow normal and tangential to the fiber, respectively. Substituting Eqs. **2-5** into **2-8**, one obtains

$$\vec{f} = \{f_n, f_t\} = -\mu \cdot \frac{\pi}{c} \cdot r^2 \cdot \left(\frac{y c_o h_o}{h^2} \frac{dh}{dt} - \frac{\partial v_y}{\partial t} \right) \left\{ \frac{\cos\theta}{K_{Pn}}, \frac{\sin\theta}{K_{Pt}} \right\} \qquad \textbf{[2-9]}$$

where *r* is the fiber radius. In Eq. **2-9** we compute the local drag force by modeling the bead-fiber structure of the core proteins in figure 1 as a uniform fiber whose radius is that of the bead to simplify the analysis. As shown earlier, in phase I ($h < h_t$), the ends of the fibers overlap and form a thin layer where a portion of the fiber ends are in contact with one another. The viscous resistance of this overlapping region is balanced by the elastic restoring force at the initial contact points of the fibers with the underside of the layer, as shown in figure **2-5**. Thus, the flat portion of the fibers move upward but remain horizontal and parallel to the capillary wall during phase I. The flat portion of a fiber exerts no restoring force since no bending energy is stored in a region of no curvature.

The instantaneous shape of core protein fibers subject to the distributed load given by Eq. **2-9** satisfies an ‘elastica’ equation for the large deformation of an elastic

strip. The governing equation in θ, s intrinsic coordinates is given by (Frisch-Fay 1962),

$$EI\frac{\partial\theta}{\partial s}=\int_s^{h^o}\left[\begin{array}{l}\left(f_n(\xi,t)\cos(\theta)+f_t(\xi,t)\sin(\theta)\right)\int_s^{\xi}\sin(\theta)d\zeta\\+\left(f_n(\xi,t)\sin(\theta)-f_t(\xi,t)\cos(\theta)\right)\int_s^{\xi}\cos(\theta)d\zeta\end{array}\right]d\xi\,. \qquad \textbf{[2-10]}$$

Here *EI* is the flexural rigidity of core protein fibers, $f_n(\xi,t)$ and $f_t(\xi,t)$ are normal and tangential components of the local instantaneous load and ξ, ζ are dummy variables. The integro-differential equation **2-10** can not be solved in a closed form, except for the special case of a concentrated vertical load applied at the fiber tip (Frisch-Fay 1962). Numerical solutions are also available for a uniform or linearly varying load (Lee, Wilson, & Oh 1993). In the current application, the numerical procedures in ANSYS (v8.0, commercially available from ANSYS, Inc.) are used to solve Eq. **2-10** for an arbitrary $\vec{f}(\xi,t)$.

Nondimensionalization: It is convenient to introduce the following dimensionless variables and parameters,

$$h^*=h/h_o,\quad y^*=y/h_o,\quad v_y^*=v_y/h_o\quad t^*=t/\tau,\quad \vec{f}^*=\vec{f}h_o^3/EI. \qquad \textbf{[2-11]}$$

Here τ is the dimensional reference time, which is defined as

$$\tau=\frac{\pi}{c_o}\cdot\frac{r^2}{K_{pn}}\cdot\frac{\mu h_o^4}{EI}. \qquad \textbf{[2-12]}$$

Equation **2-9** can be rewritten in dimensionless form as

$$\vec{f}^*=-\frac{c_o}{c}\left(\frac{c_o y^*}{h^{*2}}\cdot\frac{dh^*}{dt^*}-\frac{dv_y^*}{dt^*}\right)\{\cos\theta,\,K_r\sin\theta\}. \qquad \textbf{[2-13]}$$

Here $K_r = K_{Pn} / K_{Pt}$. One can obtain the distributed hydrodynamic load along the fiber from [13) if the local small displacements, dh^* and dv_y^*, in the time interval dt^* are known. Equations **2-10** and **2-13** can be solved numerically at each time step by an iteration procedure as described next.

Numerical solution procedure: (I) Starting from a prescribed fiber shape whose tip height is h^* at time t^*, one guesses a new fiber shape whose tip height is $h^* + dh^*$ and as an initial guess assumes other points are displaced by an amount dv_y^* which increases linearly with distance along the fiber subject to $dv_y^* = dh^*$ at $s^* = 1$ at time $t^* + dt^*$. (II) One then computes the hydrodynamic load using Eq. **2-13** for the assumed value of dh^* and the guessed displacement distribution dv_y^*. The assumed time interval dt^* serves as a scaling constant for the loading f^*. (III) Using the loading from step II, one calculates the fiber shape from Eq. **2-10** and the upward displacement of the fiber tip dh^* using the numerical program for the 'elastica' in ANSYS. The value of dt^* is set by requiring that the assumed dh^* and the predicted dh^* from the ANSYS program agree. This completes the first iteration. (IV) One now uses this newly computed shape to provide new values for dv_y^* and dh^* and iterates steps II-IV until the new fiber shape converges. The criterion for convergence is that the integral $\int_{s^*=0}^{s^*=1} \left| v_y^{*n} - v_y^{*n-1} \right| ds^* < 0.001$ where v_y^{*n-1} and v_y^{*n} denote the vertical deflection of the same fiber element at the n-1 and n iteration. Since the shape of the fiber is not very sensitive to the detailed loading, one finds that one can achieve convergence after less than 10 iterations. (V) This new shape at $t^* + dt^*$ is then treated

as a known shape and steps I-VI are repeated until the fiber layer is fully restored. In this manner, one obtains the fiber layer dimensionless height h/h_o, the dimensionless fiber deflection v_x/h_o, v_y/h_o and the dimensionless fiber loading $f_y h_o^3/EI$ as a function of t/τ.

One will observe later in Fig. **2-5(b)** that the hydrodynamic load on the fiber increases monotonically with distance *s* along the fiber length and the tangential load has a complex distribution which changes shape in passing from phase I to phase II. At the transition between phase I and II, the dimensionless transition height of the fiber layer, $h_t^* = h_t/h^o$, would be 0.367 for a linearly varying load. In phase I ($h^* < h_t^*$) the curved portion of the fiber is similar to the fiber shape at $h^* = h_t^*$ except that the fiber behaves as if it has a foreshortened length *l* in this region. Thus, the horizontal portion carrying no net load is $h^o - l$. The initial fiber shape for phase I is assumed to be that of a fiber subject to a linearly varying load on its curved portion plus its horizontal end segment. The initial height of this flat segment is the measured initial thickness of the ESL in the experiment. The initial fiber shape for phase II is the fiber shape at the end of phase I.

2.4. Results

Figure **2-4** shows the comparison of the theoretical prediction of our model with the experimental data in Fig. **2-1(b)** and the predictions reconstructed from the data in Fig. **2(b)** of Damiano and Stace (2002). In the experiment, we measured the gap between the RBC membrane and the EC membrane. This gap includes two layers, the ESL and a lubricating plasma layer between the RBC membrane and the ESL

surface (Secomb et al. 2001; Vink and Duling 1996; Weinbaum et al. 2003). The measured velocity of the WBC and hence the velocity of the trailing RBCs in Fig. **2-1(b)** is approximately 50 μm/s. At this velocity the results in Fig. **3** of Vink and Duling (1996) indicate a plasma layer thickness of approximately 70 nm. If we subtract this estimated plasma layer thickness from the measured gap of 470 nm between the RBC and EC cell membranes before the passage of the WBC one estimates that the undisturbed ESL thickness is 400 nm. In Fig. **2-4**, the measured ESL thickness is normalized by its undisturbed thickness, 400 nm, and the experimental time is normalized by the dimensional reference time τ in [12). An optimum fit between theory and experiment is obtained for τ = 11.5 s. All the parameters in Eq. **2-12** are either measured or can be theoretically approximated except the flexural rigidity EI. K_{Pn} and K_{Pn} are estimated using formula for the flow perpendicular (Sangani & Acrivos, 1982) and parallel (Cowin, Weinbaum & Zeng, 1995) to a periodic array of parallel fibers. If $h_o = 400\,nm,\ c_o = 0.16,\ \mu = 1.2\,cp,\ \ r = 6\,nm$ and $K_P = 3.16\,nm^2$ (Weinbaum et al. 2003), one finds that EI = 600 pN·nm^2. The data taken from Damiano and Stace (2002) are shifted to right by 0.01 since the starting point of their recovery is 0.5 the initial thickness of the ESL. There are no results for the early large deformation portion of the recovery. The data in Damiano and Stace (2002) is scaled by a factor of 4900 since they use a different reference time in their model.

Figures **2-5(a)** and (**b)** show the computed fiber shapes and the hydrodynamic loading, respectively, at different times during restoration. The transition between phase I and II occurs at 0.034 s when h_t^* = 0.361. The fiber shapes are not very

sensitive to the detailed load distribution as long as the fiber tip is displaced to the same height. Thus, the transition height predicted herein $h_t^* = 0.361$ is very close to the value $h_t^* = 0.367$ that would be predicted for a linearly increasing load distribution.

2.5. Discussion

We have used effective medium and 'elastica' theory for the large deformation of elastic fibers to model the core protein fiber recoil after their compression by the passage of a WBC in a tightly fitting capillary. We estimated the flexural rigidity *EI* of the core protein fibers by fitting the predictions of the model to the experimental data for the time dependent restoration of the ESL. The predicted value of *EI* is 600 pN·nm^2, which is about 85 percent of the value 700 pN·nm^2 predicted in Weinbaum et al. (2003) and about 0.042 the measured value for an actin filament (Dupuis et al. 1997; Gittes et al. 1993). This flexural rigidity of the actin filaments is required for the core proteins to be rigidly supported at their base. The present model is a major improvement over our previous model in Weinbaum et al. (2003) since we consider the relative motion of the fluid and fibers, use a realistic family of shapes for the fiber recoil and large deformation theory for 'elastica' to describe the recoil process. In contrast, Weinbaum et al. (2003) assumed a stagnant fluid and used small deformation theory. Considering these truly major improvements in the model it is rather surprising that the predicted value of EI differs by only 15 percent. This is likely due to the fact that the large deformation portion of the recoil in phase I is short lived compared to the total recoil, see Fig. **2-5a**.

It has long been recognized that the microvascular endothelium is covered with an ESL – a matrix layer of proteoglycans and glycoproteins. *In vivo* observations show that the ESL maintains structural integrity with little deformation when subject to the fluid shear stress of flowing blood (Vink and Duling 1996) and is restored to its original thickness after being crushed by the passage of WBCs as observed herein. These observations suggest that the layer has structural stiffness and elastic, oncotic or electrochemical restorative properties (Damiano and Stace 2002; Pries et al. 1997; Secomb et al. 2001; Weinbaum et al. 2003).

Wiederhielm and Black (1976) found that insoluble collagen exhibits a remarkable volume exclusion effect on plasma proteins and the oncotic pressure of a plasma protein solution is increased considerably when it is mixed with collagen and hyaluronate. Thus, Pries et al. (1997) suggest the colloid osmotic pressure in the endothelial glycocalyx layer may exceed that of blood plasma due to loosely absorbed plasma proteins on the glycocalyx component even in the absence of collagen and this increase of osmotic pressure must be balanced by tension along the core protein from a mechanical point of view. In this way, an externally applied force is needed to release the tension and deform the glycocalyx layer. Experiments in Pries et al. (1998) show that reduction of plasma protein levels in microvessels *in vivo* lead to reduced flow resistance and they hypothesize that the glycocalyx layer becomes thinner since less proteins are adsorbed. Secomb et al. (2001a; 2001b) argue that the difference in oncotic pressure required to maintain ESL thickness is extremely small, of the order 20 dyn/cm^2, and use this estimate to theoretically predict the deformation of the glycocalyx layer when RBCs pass through a capillary. This model provides reasonable

predictions of the ‘pop out’ phenomenon, the lift off of the red cell from the capillary wall and its rise through the ESL as its velocity increases starting from rest. However, Hu et al. (2000) calculated the protein concentration distribution across the glycocalyx layer and found that the concentration drops sharply across the ESL and that the layer serves as a molecular sieve. This view is strongly supported by the recent experiments of Adamson et al. (2004) where the oncotic forces across the ESL are measured. Loss of this molecular sieve by hyaluronidase treatment (Van den Berg, Vink and Spaan 2003) results in subendothelial edema formation, consistent with the associated loss of protein concentration drop across the glycocalyx. Thus, the oncotic pressure of the adsorbed proteins of the blood plasma would have to exceed the oncotic pressure induced by the ESL as a molecular sieve for oncotic swelling of the ESL to occur.

Vink, Wieringa and Spaan (1995) showed that repulsion of negative charges on the membrane of red blood cells by anionic glycocalyx sites influences capillary hemodynamics, and Vink and Duling (2000) found that negatively charged molecules diffuse more slowly into the glycocalyx than their neutral counterparts. Stace and Damiano (2001) proposed that this is due to fixed negative charges that are bound to the glycocalyx fibers. They modeled the glycocalyx layer as a diffusely distributed anionic mucopolysascharide matrix without an elastic restoring capability. Based on this picture of the glycocalyx layer, they developed a mechano-eletrochemical model to predict the recovery time of the glycocalyx layer after its compression by the passage of a WBC (Damiano and Stace 2002). The fundamental premise is that mechanical deformations of the layer caused by the passage of the WBC produce a departure from a near electroneutral equilibrium. This creates gradients of

electrochemical potential that result in a redistribution of mobile ions and a rehydration of the layer after its compression. The model can predict recovery times that agree with experiment and restoration profiles that are similar to this study see Fig. **2-4** provided the ratios of glycocalyx fixed charge concentration to mobile ion concentration and the cationic charge density of blood are chosen to provide an optimum fit.

The third hypothesis, proposed by Weinbaum et al. (2003), is that the core proteins in the ESL depicted in Fig. **1-1** have a finite flexural rigidity sufficient to withstand significant deformations of the glycocalyx layer due to blood flow and yet strong enough to restore the layer after a large amplitude compression by passing WBCs. Important experimental evidence in support of this hypothesis is the fact that the quasi-periodic structure for the distribution of the molecular level scattering centers along the axes of the core proteins observed in Squire et al. (2001) would not be possible in the presence of thermal fluctuations due to Brownian motion unless the core proteins had a non-negligible flexural rigidity. To this end the model in Weinbaum et al. (2003) predicts that the value of EI, 700 $pN{\cdot}nm^2$, required to restore the ESL after the passage of a WBC is also sufficient to limit deflections of the core proteins to at most a few percent of their length at physiological flow rates.

The elastic model in Weinbaum et al. (2003) provides only a reasonable characteristic time for the restoration of the compressed glycocalyx layer. It is too simplified to provide realistic predictions for the time dependent changes in shape of the core proteins or detailed predictions of the recovery profiles for ESL thickness that can be compared with the experimentally measured restoration curves in Fig. **2-1b**.

The theory for small deflections in Weinbaum et al. (2003) describes only the final approach to equilibrium, neglects the y component of the velocity and treats the fluid in the matrix layer as a stagnant fluid. The present model for large fiber deformations is superior in that it corrects all of these shortcomings and also considers in an approximate manner the difficulties that arise from an ESL with overlapping fibers at its edge for large compressions. This is clearly illustrated in Fig. **2-4** where the theory provides good agreement with experiment for both phase I and phase II of the restoration process using only a single curve fitting parameter *EI*.

The oncotic (Secomb et al. 2001a; 2001b), the mechano-electrochemical (Damiano & Stace 2002; Stace & Damiano 2001) and the elastic (Weinbaum et al. 2003) theoretical models all agree that the flow within the glycocalyx layer is negligible and that this layer shields the endothelial cell membrane from the direct shearing of the blood flow. Thus, these models also need to address the issue of mechanotransduction across the glycocalyx layer in addition to the mechanical properties that provide its stiffness. Both the "oncotic force" and the "mechano-eletrochemical" models neglect the flexural rigidity of the core proteins and assume that the fluid shear stress is passively transmitted to the membrane of endothelial cells as a surface traction. The basic question is how the fluid shear is transmitted across the endothelial membrane to the actin cortical web. In the oncotic force model tangential component tension develops along the ESL fibers due to fluid shear and is transmitted as a traction force to the intracellular cytoskeleton via the transmembrane proteins that form the attachment points for the ESL fibers. In the elastic model described herein fluid shear induces bending moments on the ESL fibers due to their finite flexural

rigidity. These fibers are assumed to be rigidly linked by transmembrane proteins to the actin cortical cytoskeleton beneath the membrane.

The recent experiments of Thi et al. (2004) show that in the presence of plasma proteins, either 1% bovine serum albumin or fetal bovine serum, there was a reorganization of the actin cytoskeleton and a redistribution of associated linker molecules, such as vinculin, in rat fat pad endothelial cells in response to a fluid shear of 10 dyn/cm^2 for 5h. This response could be completely abolished at the same fluid shear stress applied for the same duration if the plasma proteins were removed or the ESL was enzymatically treated with heparinase. In either case more than half the ESL fibers were still present, but they were unable to transmit the tangential stress across the membrane and there was no cytoskeletetal reorganization. Thi et al. (2004) explain this behavior in terms of the elastic model described herein. In this model the torque on the actin cytoskeleton is transmitted to the dense peripheral actin band associated with the adherens junction at the border of the cell. This model predicts that at a shear stress of 10 dyn/cm^2 the integrated torque on the adherens junction is sufficient to unzipper the VE-cadherin linkage between adjacent cells and initiate a disruption of the dense peripheral actin bands.

2.6 Footnotes

This chapter is reprinted with permission from Han, Y., Weinbaum, S., Spaan, J. A. and Vink, H. (2006) "Large deformation Analysis of the elastic recoil of the core protein in the endothelial glycocalyx." the 50th anniversary issue for *J. Fluid Mechanics*.

Chapter 3 Deformation of the Glycocalyx Due to the Red Cell Motion and Arrest

3.1 Deformation Due to Red Cell Motion

One of the striking observations in Vink and Duling (1996) is that when the red cell motion is arrested, the cell expands to fill nearly the entire capillary lumen. At very low velocities, < 20 μm/s, the red cell membrane slowly lifts off the wall and at velocities > 20 μm/s the cell "pops out" of the layer and glides above the glycocalyx with a fluid gap that increases nearly linearly with increasing speed as observed in Fig. 3 of Vink and Duling (1996), which is adapted and shown here as Fig. **3-1**. The “pop out” behavior while the cell is still in the endothelial surface layer (ESL) has been examined in Feng and Weinbaum (2000) and Secomb (2001). In Feng and Weinbaum (2000) it is shown that the compression of the layer is closely akin to snowboarding on fresh snow powder. The fluid is trapped within the fibers of the compressed matrix and is unable to fully escape on the time scale of the cell passage with the result that lubrication pressures far greater than predicted by classical lubrication theory can be generated. The analysis in Secomb (2001) considers a deformable cell whose membrane is subject to fluid shear and bending deformation. The latter analysis provides intuitive insight into the shape changes that occur for an axisymmetric cell during lift off from the capillary wall. Neither Feng and Weinbaum (2000) nor Secomb (2001) consider the visco-elastic deformation of the ESL.

We first develop a simple model for the deformation of the ESL when the red cell is gliding above its outer edge at velocities > 20 μm/s. The observations in Vink

and Duling (1996) show a nearly uniform fluid gap δ between the outer edge of the ESL and the red cell membrane that increases initially with increasing velocity and then asymptotes to a nearly uniform gap. This suggests a simple two-dimensional model for the fluid motion in the confined region, a parallel channel flow with two layers, a Brinkman layer of thickness L_f on the bottom to describe the ESL and a clear plasma layer of thickness δ on top, as shown in Fig. **3-2**. For the fluid in the Brinkman layer,

$$0 = \mu \frac{d^2 u}{dx^2} - \frac{\mu}{K_P} u \,. \qquad \textbf{[3-1]}$$

For the fluid in the plasma layer,

$$0 = \mu \frac{d^2 u}{dx} \,. \qquad \textbf{[3-2]}$$

Here K_P is the Darcy permeability of the glycocalyx layer and μ is the fluid velocity. At the capillary wall and the moving red cell membrane one applies the non-slip conditions,

$$u(0) = 0 \quad \text{and} \quad u(L_f + \delta) = U_{RBC} \,. \qquad \textbf{[3-3]}$$

At the interface between the regions one requires continuity in the fluid velocity but discontinuity in the average fluid shear stress due to the solid fraction of ESL,

$$u^+ = u^-, \mu \frac{du^-}{dx} = (1 - c) \frac{du^+}{dx} \,. \qquad \textbf{[3-4]}$$

Solving Eqs. **3-1** and **3-2** with boundary conditions **3-3** and **3-4**, one obtains the closed form solutions for the velocity field across the ESL as

$$u = \frac{(x - L_f)\cdot L_f^2/K_P \cdot \cosh(L_f^2/K_P) + (1-c)\sinh(L_f^2/K_P)}{\delta \cdot L_f/K_P \cdot \cosh(L_f^2/K_P) + (1-c)\sinh(L_f^2/K_P)}, \qquad L_f \le x \le L_f + \delta;$$
$$u = \frac{(1-c)\sinh(xL_f/K_P)}{\delta \cdot L_f/K_P \cdot \cosh(L_f^2/K_P) + (1-c)\sinh(L_f^2/K_P)}, \qquad 0 \le x \le L_f. \quad \textbf{[3-5]}$$

Figure **1-1** shows that the root of the core protein fiber is firmly anchored into the cortical cytoskeleton web. Thus, the core protein fiber can be ideally modeled as a cantilever beam, shown in Fig. **3-3**, whose governing equation is

$$EI\frac{d^4y}{dx^4} = \frac{\pi}{c}\frac{\mu a^2}{K_P}u \ . \quad \textbf{[3-6]}$$

with boundary conditions

$$At \quad x = L_f, \ \frac{d^2y}{dx^2} = 0, \frac{d^3y}{dx^3} = \frac{\mu c}{EI \cdot n}\cdot\frac{du^+}{dx};$$

$$At \quad x = 0, \ y = \frac{dy}{dx} = 0. \quad \textbf{[3-7]}$$

Here y is the lateral deflection of the core protein and EI and α are its bending rigidity and radius, respectively. Note that the right side of Eq. **3-6** is the hydrodynamic drag force per unit length on the core protein (Guo et al. 2000) and the fluid velocity is given in Eq. **3-5**. One solves Eq. **3-6** with boundary conditions **3-7** analytically to obtain the deflection of the core protein fiber.

The results of the above model have been plotted in Fig. **3-4** using the parameters $L_f = 400\,nm$, $EI = 700\,pN\cdot nm^2$, $c = 0.16$, $\mu = 1.2\,cp$, $r = 6\,nm$ and $K_P = 3.16\,nm^2$ for the ESL as employed in Weinbaum et al. (2003). Fig. **3-4** also shows the theoretical prediction for deflection of core protein fibers at a plasma fluid shear of 10 dyn/cm^2 on the outer edge of the EG. The novel feature of this solution is that the increase in the fluid gap δ as a function of the red cell velocity U_{RBC} has been

estimated using the measured data in Fig. **3-1** adapted from Vink and Duling (1996). This allows us to circumvent the much more difficult problem of developing a model for finding the change in red cell shape as a function of its velocity and capillary diameter when our primary interest is the forces and bending moments on the vertical fibers and their deformation. Fig. **3-4** shows our predictions for the change in fiber shape as a function of increasing red cell velocity from 20 to 210 μm/sec for red cells traveling in a 5 μm diameter hamster cremaster capillary where L_f is 0.4 μm. One observes that the magnitude of the tip deflection at 210 μm/s is about one half of the prediction for a shear stress of 10 dyn/cm^2 (Weinbaum et al. 2003), but decreases rapidly as the red cell velocity and fluid gap δ decrease.

3.2. Fluid Drainage from ESL Due to Red Cell Arrest

Weinbaum et al. (2003) predict that the maximum pressure that the ESL can withstand without its fibers buckling is 160 dyn/cm^2 when the red cell comes to rest. It will be interesting to compare this elastic restoring force with the excess pore pressure created by the draining of the fluid from the ESL when the motion of a red cell is arrested. The latter is estimated by considering the stationary red cell as a cylindrical pellet of constant radius which uniformly expands under an applied pressure P_C to crush the glycocalyx. To simplify the model we have neglected the deformation of the red cell membrane due to the fluid drainage, membrane elastic properties and the initial stress-free configuration of the cell in its biconvex shape. These membrane related considerations lead to complex shapes for the red cell membrane that are described in (Wu and Weinbaum 1982) for a compressed red cell or (Secomb 2001)

for a moving axisymmetric cell. The motion of the fluid in the glycocalyx satisfies Darcy's law and continuity. The thin fiber interaction layers near the endothelial and red cell membranes are neglected. The flow in the layer is treated as a time dependent flow in a compressible porous medium whose velocity varies as a function of time and distance from the leading or trailing edge of the pellet. We wish to capture the large amplitude deformation of the ESL and the changes in K_P that result from this deformation. The change in K_P as a function of L_f is modeled using the solutions in (Sangani and Acrivos 1982) for the slow flow through a face centered periodic array of spheres whose solid fraction c changes as a function of L_f. For the large deformations considered in this application, where the fibers are crushed, the fluid resistance of the compacted matrix is better represented by the spherical particles on the core proteins as opposed to cylindrical fibers.

3.2.1. Governing Equations

The draining of fluid from the ESL due to red cell arrest is modeled in the Fig. **3-5**. In the figure $v_y(y)$ is the local velocity of fluid in the ESL; W is the width of red cell; P_c is compression pressure of the red cell membrane on the ESL and L_f is the height of the ESL. For a flexible membrane L_f is a function of both y and t, see Wu and Weinbaum (1982). However, for present purposes, where we are primarily interested in the characteristic time for the fluid drainage, we treat L_f as a rigid planar surface. As described in the text, the process is governed by Darcy's law,

$$\frac{\partial p}{\partial y} = -\frac{\mu}{K_p} v_y \ , \qquad \textbf{[3-9]}$$

and continuity ,

$$y\frac{dL_f}{dt} = -v_y L_f \,. \qquad \textbf{[3-10]}$$

Combining the above two equations, one obtains the pressure distribution beneath the red cell membrane,

$$p - p_0 = \frac{\mu}{8K_p}\left(-\frac{dL_f}{dt}\right)\left(\frac{W^2 - 4y^2}{L_f}\right), \qquad \textbf{[3-11]}$$

where p_o is the ambient pressure at the edge of the compression zone. The average compression pressure on the ESL must equal the cell pressure. Thus,

$$P_c = \frac{2\int_0^{\frac{W}{2}}(p - p_0)dy}{W} = \frac{\mu W^2}{12K_p L_f}\left(-\frac{dL_f}{dt}\right) . \qquad \textbf{[3-12]}$$

Assuming P_c and W are constant, one obtains

$$t = \frac{\mu W^2}{12p_c}\int_{L_{f0}}^{L_f}\frac{-dL_f}{K_p L_f} . \qquad \textbf{[3-13]}$$

Where L_{f0} is the initial ESL thickness. If K_p is constant, then

$$L_f / L_{f0} = \exp(-t/\tau) \,, \qquad \textbf{[3-14]}$$

with

$$\tau = \frac{\mu W^2}{12P_c K_P} . \qquad \textbf{[3-15]}$$

However, for the large compressions of the ESL considered herein K_p is a function of the instantaneous solid fraction *c*.

3.2.2. Estimation of *Kp*

In Sangani and Acrivos (1982), the expression for the drag force on a single spherical scattering center along the core protein is

$$F = 6\pi K \mu r v_y , \qquad \textbf{[3-16]}$$

where r is the radius of the scattering center and K is the drag force coefficient. Sangani and Acrivos (1982) showed that for a face-centered cubic array of spheres,

$$K = \sum_{s=0}^{30} q_s \left[(c / c_{\max})^{1/3} \right]^s , \qquad \textbf{[3-17]}$$

where $c_{\max} = 0.74$ is the maximum solid fraction for the face-centered array and the q_s are coefficients given in Sangani and Acrivos (1982). From Darcy's law, one can show that K_p is related to K by

$$K_p = \frac{\varepsilon K^{-1}}{6\pi r}, \qquad \textbf{[3-18]}$$

where $\varepsilon = \frac{4\pi r^3}{3c}$.

3.2.3. Estimation of other parameters

To solve the above equations, we have to estimate two other parameters: the solid fraction c and the width W of the red cell compression along the ESL. Mass conversation within the solid phase requires that

$$c = \frac{L_{f0} c_0}{L_f}, \qquad \textbf{[3-19]}$$

where c_0 = 0.13 for the initial array of spherical scattering centers depicted in Fig.1. For a red cell volume of 90 μm^3, a capillary diameter of 5 μm and L_f = 0.4 μm, W=4.6 μm initially and increases to 6.5 μm after maximum crushing of the ESL if the

assumed shape is that of a circular cylindrical pellet. In our calculation we let W be the mean of these two values.

3.2.4. Calculation

a. Constant K_p

Substituting t = 0.5 s into Eq.**3-14**,

$$\exp(-t/\tau) = \frac{L_{f\,\min}}{L_{f0}} = \frac{c_0}{c_{\max}} = 0.176\,.$$

Therefore,

$$\tau = 0.29 \text{ s}.$$

Substituting τ into Eq. **3-15** and rearranging, one obtains

$P_c = 2421$ dyn/cm^2.

b. Variable K_p

Combining Eqs.**3-16~3-18**, one finds K_p is only a function of L_f. Thus, the integrand of the integral in Eq.**3-13** is only a function of L_f. For $P_c = 2421$ dyn/cm^2 the relationship between t and L_f is given in the following Table **3-I** and plotted in Fig.**3-6**. Note that the time for maximum compaction has been extended by a factor of 50 from 0.5 to 25 s.

3.2.5 Results

The results of the model for the fluid drainage are shown in Fig.**3-6**. The time scale for the drainage is determined by the observation that the gap between the red and EC membranes nearly vanishes in 0.5 s (Hans Vink private communication). We

assume that the expansion pressure P_C exerted by the spectrin cortical cytoskeleton (CC) of the red cell and its internal hydrostatic pressure are constant over the draining process and the elastic restoring force of the glycocalyx is neglected. Two solutions for the time dependent collapse of the glycocalyx are shown, one for a constant Darcy permeability K_P and a second for a time varying decrease in K_P where L_f is a function of c as described above. For constant K_P the characteristic time is given by $\mu W^2/12P_C K_P$ where W is the pellet length. For the initial array c=0.13 whereas for maximum compaction c=0.74. For constant K_P an applied pressure of 2420 dyn/cm^2 is required to fully drain the ESL in 0.5 s. If this same pressure is applied in the variable K_P model the total draining time is extended to 25 s. This applied pressure is 20 times the elastic buckling pressure of the core proteins in Fig.5B. This justifies the neglect of the elastic restoring force in the fluid draining model.

3.3. Discussion

Since red cells are continuously flowing through our capillary beds with an intermittency that causes their velocity to vary widely, one would intuitively expect that their motion does not cause frequent disruptive interactions with the ESL. The predicted structural properties of the core proteins appear to be finely attuned to this motion. Fig. **3-4** shows that the passage of red cells over a wide rage of velocities from 20 to > 200 μm/s causes only minor deformations of the core proteins. At velocities < 20 μm/s the observations in Vink and Duling (1996) and the theoretical models (Feng and Weinbaum 2000; Secomb 2001) predict that the red cell will enter the ESL. This will occur when the flow in a capillary is temporarily arrested by the passage of a red

cell through a tightly fitting arteriolar sphincter at the entrance to a microvessel. Much larger repulsive forces are required here to prevent adhesive interactions between proteins in the red and EC membranes. The stiffness of the core proteins, though adequate to resist the penetration of red cells during their normal motion, is insufficient to prevent their buckling when red cell motion is arrested. Weinbaum et al. (2003) predicts that the buckling pressure for a core protein cluster is ~100 pN/cm^2 when L_f = 400 nm and increases as $1/L_f^2$. The added resistance to the collapse of the glycocalyx arises from the time dependent draining of the fluid in the compressed ESL. Our simplified model for the draining of this layer predicts that the pressure generated by the draining of the fluid trapped in the ESL is at least 20 times greater than the elastic restoring forces exerted by the core proteins (Weinbaum et al. 2003). It is this pressure and not the elastic response of the matrix that prevents the red cell from rapidly entering the matrix when its motion is arrested.

The characteristic fluid draining time for the ESL, $\mu W^2/(12P_cK_P)$, is a sensitive function of K_P. The results in Fig.**3-6** show that the draining time for large compressions is greatly extended by the large decrease in K_P that accompanies matrix compaction. This can be thought of as an additional safety factor preventing the adhesive interaction between proteins in the opposing membranes when motion is arrested. This allows the red cell to slowly enter arteriolar sphincters without the flow coming to a complete cessation. With few exceptions red cells enter capillaries edge on and fold up on themselves much like a crepe. Their bending stiffness in this configuration is much greater than the axisymmetric configuration treated in Secomb (2001). In the latter study the authors showed that an oncotic pressure of only 40

dyn/cm^2 would prevent the ESL from collapsing. This is less than the elastic buckling pressures predicted in Weinbaum et al. (2003). The large increase in pressure that can be generated by the folded cell in tightly fitting capillaries is due to the small radius of curvature of its inner plasmalemma in the folded edge on configuration.

3.4 Footnotes

This chapter is reprinted and partially rewritten with permission from Weinbaum, S., Zhang, X., Han, Y., Vink, H. and Cowin, S. (2003) "Mechanotransduction and flow across the endothelial glycocalyx." *Proc. Natl. Acad. Sci. USA* **100**(13): 7988-7995.

Chapter 4 Transmission of Steady and Oscillatory Fluid Shear Stress across Epithelial and Endothelial Surface Structures

4.1. Introduction

All vascular endothelial cells and many epithelial cells are covered at their apical surface by either a surface matrix of glycoproteins and proteoglycans or an organized array of microvilli or cilia. These structures have been proposed to play an important role in the transmission of fluid shear stresses to the intracellular cytoskeleton of the cell (Florian et al. 2003; Guo, Weinstein and Weinbaum 2000; Liu et al. 2003; Praetorius and Spring 2001; Secomb et al. 2001; Weinbaum et al. 2003). In the case of endothelial cells, Florian et al. (2003) experimentally demonstrated that heparan sulfate proteoglycan, a major component of the endothelial surface layer (ESL), plays an important role in mechanotransduction by mediating NO production in response to fluid shear stress. Recently, Squire et al. (2001) were able to identify a quasiperiodic substructure for the core proteins of the glycocalyx whose anchoring foci appear to emanate from the underlying cortical cytoskeleton. This observed structure was transformed into an idealized mathematical model in Weinbaum et al. (2003) for predicting the forces and torques on the core proteins in the endothelial surface layer (ESL) and the deformation of both these proteins and the underlying cortical cytoskeleton when the ESL was subject to steady fluid shear at its outer edge. In the case of epithelial cells both proximal tubule and intestinal epithelium have an ordered hexagonal array of hair-like projections, or microvilli, of locally uniform length that greatly increase their area for transport (Welling and Welling 1975). In

addition, some epithelial cells have a single central primary cilium, e.g. the principal cells in the cortical collecting duct (CCD) (Latta, Maunsbach and Madden 1961; Pfaller and Klima 1976; Schwartz et al. 1997). Guo et al. (2000) have proposed that the microvilli in the proximal tubule perform a mechanosensory function and serve as the afferent sensor of flow in 'glomerulotubular balance', the observation that reabsorption varies proportionally with the tubule flow rate. Similarly, Praetorius and Spring (2001) and Liu et al. (2003) have proposed that the primary cilia in the CCD also serve a mechanosensory function in intracellular signaling. The cilia in the present analysis are primary cilia with a 9 + 0 microtubule structure and are passive. In contrast, active beating cilia have a 9 + 2 structure with two central microtubule pairs that are capable of self deformation due to the motion of their dynein molecules.

In this chapter we shall develop a generalized theory for examining the fluid-solid interaction in these structures when the apical surface of the cell is subject to either steady or oscillatory shear. The latter is of particular importance in the case of the ESL since numerous studies in fluid flow chambers have shown that there is a different intracellular response to fluid shear in steady laminar flow and sinusoidal flow of the same magnitude (Helmliger, Berk and Nerem 1995; Hillsley and Tarbell 2002). We shall examine the fluid and solid motion within the surface layer and the drag and torque on the core proteins, microvilli or cilia taking into account the hydrodynamic interaction between the structural elements. We shall also predict the deformation of these structural components using existing models for their bending rigidity *EI*. While previous studies (Guo et al. 2000; Liu et al. 2003; Weinbaum et al. 2003) have addressed these applications for particular structural geometries and

specific sets of physical parameters, this is the first study to examine the transient dynamic response of any of the structures to sinusoidal loading and the first to explore the behavior in a more general dimensionless parameter space. The fundamental new insight provided by the present study is that it examines the relative motion of the fluid and solid components and their amplitude and phase. In the steady state analysis the solid structures deform but their velocity is zero by definition. Note that in the case of the ESL, Secomb et al. (2001) have proposed an alternative model for the transmission of fluid shear stress to endothelial cells by assuming that the structural rigidity of the layer arises from oncotic forces due to absorbed proteins. Their model neglects the bend rigidity *EI* of the core proteins and, thus, does not explain how the shear stress is transmitted to the cortical cytoskeleton.

Liu et al. (2003) point out in their recent paper that the flow past microvilli and cilia lie at opposite ends of a dimensionless parameter space. Cilia typically have a separation that is comparable to their length L and, thus, the value of the dimensionless Brinkman parameter $\alpha = L/\sqrt{K_p}$ is ~ 1 since $\sqrt{K_P}$, where K_P is the Darcy permeability, has the dimensions of length and for a fiber medium is characteristic of the spacing between the fibers. The value of α for microvilli is shown in Guo et al. (2000) to be ~ 100 and, thus, from asymptotic analysis one can show there is a thin fiber interaction layer near the tips of the microvilli whose thickness is $\sim \sqrt{K_P}$. Weinbaum et al. (2003) show, quite surprisingly, that the core protein structure for the ESL observed by Squire et al. (2001) has a value of α that is of the same order as that for microvilli, though the dimensions of these structures differ by an order of magnitude. Hence the model for steady flow through a capillary with its

ESL predicts results that are nearly the same as the model first proposed in Guo et al. (2000) for flow through the proximal tubule which is lined with microvilli. In the present analysis we shall also explore the steady state behavior that lies between these limiting solutions.

The formulation of the dimensionless problem for the oscillating shear stress shows that the critical new parameter that enters the analysis is the dimensionless frequency $\omega_r = \omega/\omega_c$, where $\omega_c = \frac{c}{\pi}\frac{EI}{\mu r_f^2 L^2}$ is the natural frequency for the damped vibration of the structural element. There are two questions of special interest. First, will the amplitude of the deformation of the structural element due to the fluid flow follow a quasi-steady behavior or will it deviate significantly due to the viscous dissipation arising from the relative motion of the structural element and the fluid? We shall show that this attenuation is a function of ω_r and α, but in the large α limit the dependence on α is lost and the attenuation becomes independent of the length of the structural element. This type of fluid-solid interaction problem has been looked at in the past primarily for the case where either the fluid or solid or both had inertia. In the present case the Reynolds number is so low that inertia is negligible for all meaningful frequencies. Second, will the fluid motion be in phase with the applied force or will it deviate due to the motion of the structural elements? In effect what are the requirements for the structural elements to be able to follow the motion of the fluid within the Brinkman medium? This behavior we shall find will be strongly dependent on the frequency of the applied shear compared to the natural frequency of the structural element in the viscous medium.

4.2. Structural Background

In this section, we will briefly describe our idealized structural models for the arrangement of the core proteins in endothelial glycocalyx, the microvilli in brush border cells of the proximal tubule and the primary cilia in the principal cells of the CCD.

Figure **4-1(a_1)** is a schematic of a proximal tubule epithelial cell including its basic intracellular structures. This figure shows that the apical border of the cell contains a dense array of uniform microvilli, which vary from 1.5 to 3 μm in height depending on location in the proximal tubule. Typically, there are approximately 4000 microvilli per cell. One hexagonal unit of the *en face* view of the microvilli is shown in Fig. **4-1(a_2)**. Aside from the hexagonal spacing of microvilli themselves, Guo et al. (2000) assumed that the cross-section of each microvillus contained on average seven long axial microfilaments arranged in an hexagonal array with one at the center and six at the half radius of each microvillus. It is also assumed that the seven actin filaments bear the entire bending moment induced by the hydrodynamic drag on each microvillus since the fimbrin and α-actin cross links are highly flexible. Using this basic structure, Guo et al. (2000) estimated the bending rigidity EI of each microvillus utilizing the measured elastic properties of the individual actin filaments (Kishino and Yanagida 1988).

Figure **4-1(b_1)** is a sketch of the endothelial glycocalyx layer and the underlying cortical cytoskeleton based on the quasi-periodic structure observed in Squire et al. (2001) and the simplified mathematical model proposed in Weinbaum et

al. (2003) The bush-like structural elements of the endothelial glycocalyx appear to emanate from cortical cytoskeletal foci in the cell membrane. The cortical shell is tethered by α-actinin-linked transcellular stress fibers to focal adhesion sites of intergrins on the basal aspect of the cell. An *en face* view of the idealized model in Fig. **4-1(b_2)** shows two levels of periodicity, an hexagonal arrangement of the core proteins with 20 nm spacing in each cluster and an hexagonal arrangement of the common intercluster or cytoskeletal foci with 100 nm spacing that is attached to the actin scaffold beneath the cell membrane by short and rigid linker molecules.

Figures **4-1(c_1)** and **4-1(c_2)** show the arrangement of the primary cilia in the CCD. Figure **4-1(c_1)** is an idealized model of the longitudinal and radial cross sections of a CCD taken from Liu et al. (2003). Figure **4-1(c_2)** shows the hexagonal appearance and dimensions of the epithelial cells on the apical surface of a split-open CCD. The dimensions of the cells and cilia are taken from the morphological observations in Evan et al. (Evan et al. 1991) There are two types of epithelial cells in the CCD, principal cells and intercalated cells. However, a central primary cilium is found only in principal cells. Following Liu et al. (2003), we neglect the smaller population of intercalated cells since they are much less numerous than the principal cells. In Fig. **4-1(c_1)**, the solid and dotted lines denote cilia in different planes, which are separated by 5.7 μm. At the center of each hexagonal cell in Fig. **4-1(c_2)** stands a vertical cilium, which is 0.2 μm in diameter and 2.5 ~ 8 μm in length. Mature cilia are typically 2.5 μm long, whereas the 8 μm length is representative of newly formed tubule.

4.3. Mathematical Formulation

In this section, we present a mathematical model to simulate the response of the structural elements and the fluid confined within the border or matrix layer adjacent to a capillary, tubule or collecting duct wall to a steady or oscillatory shear stress applied at its outer edge. The geometry of the model is shown in Fig. **4-2**. If the ratio of the matrix thickness L to the radius of the capillary, tubule or collecting duct is small, its wall can be modeled locally as a planar surface (x=0). In the case of oscillatory flow, a periodic shear stress $\tau_L = -\tau_0 \cos(\omega t)$ is applied at the edge of the surface layer (x=L). If the oscillatory force is applied for a long period of time, the start-up effect can be neglected and the motions of both the fluid and the structural elements are harmonic.

Based on the structural models depicted in Figs. **4-1(a~c)** and the more detailed discussion in Guo et al. (2000), Weinbaum et al. (2003) and Liu et al. (2003), we assume that all structures are firmly anchored to stiffer structural elements in the cortical cytoskeleton of the cell. Thus, the vertical structural elements can be treated as cantilever beams, whose deformation in the limit of small deflection is given by

$$EI \frac{\partial^4 y}{\partial x^4} = f(x,t), \qquad \textbf{[4-1]}$$

where EI is the flexural rigidity of the structural element, y is the deflection of the element along its length x, and $f(x, t)$ is the local drag force per unit length induced by the local relative motion between the fluid and the structural element. In the above equation, we neglect the inertia of the structural element, since the fluid motion is viscous dominated and the mass of the structural elements can be neglected. For an hexagonal fiber array, Guo et al. (2000) derived an expression for the local drag force per unit length,

$$f(x) = \frac{\pi\mu u(x)}{c}\frac{r_f^2}{K_P}, \qquad \textbf{[4-2]}$$

where μ is the viscosity of the fluid trapped, r_f is the radius of the fibers, c is the solid fraction in the surface layer, K_p is the Darcy permeability of the surrounding fiber matrix and $u(x)$ is the local fluid velocity. The Darcy permeability describes the hydrodynamic interaction between the fibers and is obtained from the local Stokes flow solution for the two-dimensional flow past the fiber array.

Weinbaum et al. (2003) examine the viscoelastic recoil of an hexagonal fiber array in a stagnant fluid after the removal of a point force applied at the fiber tips. In their analysis they replace the local fluid velocity, *u*, in Eq. **4-2** by the local recoil velocity of the individual fibers, $\frac{\partial y}{\partial t}$. They neglect the background motion of the fluid since it is initially stagnant. In the present application the local drag force is proportional to the local relative velocity between the fluid and fibers, which can be expressed by

$$f(x,t) = \mu\frac{\pi}{c}\frac{r_f^2}{K_p}\left(u - \frac{\partial y}{\partial t}\right). \qquad \textbf{[4-3]}$$

Following Guo et al.[1] and Weinbaum et al. (2003), one can relate K_P to the solid fraction, *c*, by

$$\frac{K_P}{r_f^2} = \frac{\ln\left(c^{-1/2}\right) - 0.745 + c - c^2/4}{4c}, \qquad \textbf{[4-4]}$$

Equation **4-4** is derived based on the solutions for the local two-dimensional Stokes flow past an hexagonal array of parallel circular cylinders in Sangani and Acrivos

(Sangani and Acrivos 1982) and is valid for $c < 0.4$. Combining Eqs. **4-1** and **4-3**, one obtains the desired beam equation for a single structural element,

$$EI\frac{\partial^4 y}{\partial x^4} = \mu\frac{\pi}{c}\frac{r_f^2}{K_p}\left(u - \frac{\partial y}{\partial t}\right). \qquad \textbf{[4-5]}$$

Equation (4-5) satisfies the usual boundary conditions for a cantilever beam,

$$y(0,t) = \frac{\partial y(0,t)}{\partial x} = \frac{\partial^2 y(L,t)}{\partial x^2} = \frac{\partial^3 y(L,t)}{\partial x^3} = 0. \qquad \textbf{[4-6]}$$

The motion of the fluid surrounding the fibers is modeled using effective medium theory. The Brinkman equation for uni-directional, time-dependent flow in a porous medium whose fibers are moving with local velocity $\frac{\partial y}{\partial t}$ is

$$0 = \mu\frac{\partial^2 u}{\partial x^2} - \frac{\mu}{K_P}\left(u - \frac{\partial y}{\partial t}\right). \qquad \textbf{[4-7]}$$

The corresponding boundary conditions which must be satisfied are

$$u(0,t) = 0 \text{ and } -\mu\frac{\partial u(L,t)}{\partial x} = \tau_L = -\tau_0\cos(\omega t). \qquad \textbf{[4-8]}$$

Note that in Eq. **4-7** we neglect the inertia of the fluid flow, since the Reynolds number is ~ 10^{-3} or smaller and Eq. **4-8** neglects the fluid shear stress acting on the interface area containing the tips of the structural elements.

To simplify the formulation, we introduce the following dimensionless variables,

$$x^* = \frac{x}{L},\ t^* = \omega t,\ u^* = \frac{u}{u_c},\ y^* = \frac{y}{y_c}, \qquad \textbf{[4-9]}$$

where u_c is the characteristic velocity and y_c is the characteristic deflection of the structural element. For large α, Guo et al. (2000) have shown that the fluid velocity

variation is concentrated in a tip interaction layer whose thickness is of order $\sqrt{K_P}$. Therefore, we choose the characteristic velocity u_c as $\frac{\tau_0\sqrt{K_P}}{\mu}$. Substituting this characteristic velocity for $u(x)$ in Eq. **4-2** and multiplying by the characteristic tip layer thickness, $\sqrt{K_P}$, one obtains the characteristic drag force F_c on each structural element,

$$F_c = f_c\sqrt{K_p} = \frac{\pi}{c}r_f^2\tau_0, \qquad \textbf{[4-10]}$$

where the subscript c indicates this is a characteristic value. Equation **4-10** expresses the force balance in the tip layer in the case of large α. If the drag force in Eq. **4-10** is treated as a point force at the tip of the structural element, one finds using elementary cantilever beam theory that the characteristic deflection of the structural element is

$$y_c = \frac{\pi}{3c}\frac{r_f^2L^3\tau_0}{EI} = \frac{\tau_0 L}{3\mu\omega_c}, \qquad \textbf{[4-11]}$$

where $\omega_c = \frac{c}{\pi}\frac{EI}{\mu r_f^2L^2}$ is the characteristic frequency for the damped vibration of the structural element. Note that ω_c is a physical parameter representing the bending rigidity of the structural element and is independent of K_P and hence the permeability parameter α. With these new variables the non-dimensional form of Eq. **4-5** is

$$\frac{\partial^4 y^*}{\partial x^{*4}} = 3\alpha\left(u^* - \frac{\alpha\omega_r}{3}\frac{\partial y^*}{\partial t^*}\right), \qquad \textbf{[4-12]}$$

where $\omega_r = \frac{\omega}{\omega_c}$ is the ratio of the applied frequency to the characteristic frequency and, as defined earlier, $\alpha = \frac{L}{\sqrt{K_P}}$. Note that the combination $\frac{\alpha\omega_r}{3}$ is not used as a dimensionless group. This will enable us later to retain α with same power in the second and third terms of Eq. **4-20** and also boundary condition **4-22**. After non-dimensionalization, equation **4-7** can be written as

$$0 = \frac{\partial^2 u^*}{\partial x^{*2}} - \alpha^2 \left(u^* - \frac{\alpha\omega_r}{3} \frac{\partial y^*}{\partial t^*} \right). \qquad \textbf{[4-13]}$$

When the boundary conditions are also put in dimensionless form, equations **4-6** and **4-8** become

$$y^*(0,t^*) = \frac{\partial y^*(0,t^*)}{\partial x^*} = \frac{\partial^2 y^*(1,t^*)}{\partial x^{*2}} = \frac{\partial^3 y^*(1,t^*)}{\partial x^{*3}} = 0\,, \qquad \textbf{[4-14]}$$

and

$$u^*\left(0,t^*\right) = 0 \text{ and } \frac{\partial u^*\left(1,t^*\right)}{\partial x^*} = \alpha \cos\left(t^*\right). \qquad \textbf{[4-15]}$$

Equations **4-12** and **4-13** with boundary conditions **4-14** and **4-15** may be solved analytically for the fiber deflection $y^*\left(x^*,t^*\right)$ and fluid velocity $u^*\left(x^*,t^*\right)$. From these equations, one concludes that the dimensionless solutions depend on two dimensionless parameters α and ω_r. When one substitutes the dimensional *y(x,t)* and *u(x,t)* into Eq. **4-3**, and integrates *F(x,t)* over the length of the element one obtain the total drag force induced by the relative motion of fluid and the structural element. The integral of $F(x,t)\cdot x$ yields the total torque. Details of the solution procedure follow.

Since the motions of both the structural elements and the fluid are in a periodic steady state, it can be assumed that

$$y^*\left(x^*,t^*\right)=\Re e\left(y^0\left(x^*\right)e^{i\cdot t^*}\right),\quad u^*\left(x^*,t^*\right)=\Re e\left(u^0\left(x^*\right)e^{i\cdot t^*}\right), \qquad \textbf{[4-16a, b]}$$

where $y^0\left(x^*\right)$ and $u^0\left(x^*\right)$ are complex functions and $\Re e$ denotes the real part of a complex function. Substituting Eqs. **4-16a** and **4-16b** into Eqs. **4-12** and **4-13** and removing $\Re e$ and $e^{i\cdot t^*}$ from both sides of the resulting equations, one obtains the coupled ordinary differential equations,

$$\frac{d^4y^0\left(x^*\right)}{dx^{*4}}=3\alpha\left[u^0\left(x^*\right)-i\frac{\alpha\omega_r}{3}y^0\left(x^*\right)\right], \qquad \textbf{[4-17]}$$

$$0=\frac{d^2u^0\left(x^*\right)}{dx^{*2}}-\alpha^2\left[u^0\left(x^*\right)-i\frac{\alpha\omega_r}{3}y^0\left(x^*\right)\right]. \qquad \textbf{[4-18]}$$

From Eq. **4-17**, $u^0\left(x^*\right)$ can be expressed as

$$u^0\left(x^*\right)=\frac{1}{3\alpha}\left(\frac{d^4y^0\left(x^*\right)}{dx^{*4}}+i\alpha^2\omega_r y^0\left(x^*\right)\right). \qquad \textbf{[4-19]}$$

Substituting Eq. **4-19** into **4-18** and rearranging, one can eliminate $u^0\left(x^*\right)$ and obtain a sixth-order differential equation solely for $y^0\left(x^*\right)$,

$$\frac{d^6y^0\left(x^*\right)}{dx^{*6}}-\alpha^2\frac{d^4y^0\left(x^*\right)}{dx^{*4}}+i\,\alpha^2\omega_r\frac{d^2y^0\left(x^*\right)}{dx^{*2}}=0, \qquad \textbf{[4-20]}$$

with boundary conditions,

$$y^0(0)=\frac{\partial y^0(0)}{\partial x^*}=\frac{\partial^2y^0(1)}{\partial x^{*2}}=\frac{\partial^3y^0(1)}{\partial x^{*3}}=0, \qquad \textbf{[4-21]}$$

and

$$\frac{d^4y^0(0)}{dx^{*4}}+i\,\alpha^2\omega_r y^0(0)=0\qquad\frac{d^5y^0(1)}{dx^{*5}}+i\alpha^2\omega_r\frac{dy^0(1)}{dx^*}=3\alpha^2. \qquad \textbf{[4-22]}$$

where Eq. **4-19** has been employed in rewriting boundary condition **4-15**. Note that α appears only as α^2 in Eqs. **4-20** and **4-22**.

The general solution of Eq. **4-20** is,

$$y^0\left(x^*\right) = c_1 + c_2 x^* + c_3 e^{\lambda_1 x^*} + c_4 e^{\lambda_2 x^*} + c_5 e^{\lambda_3 x^*} + c_6 e^{\lambda_4 x^*}, \qquad \textbf{[4-23]}$$

where λ_1, λ_2, λ_3, λ_4 are the characteristic values of Eq. **4-20** given by

$$\lambda_{1,2} = \pm\sqrt{\frac{\alpha^2 + \alpha\sqrt{\alpha^2 - i\,4\omega_r}}{2}} \text{ and } \lambda_{3,4} = \pm\sqrt{\frac{\alpha^2 - \alpha\sqrt{\alpha^2 - i\,4\omega_r}}{2}}, \quad \textbf{[4-24a,b]}$$

and c_1, c_2, c_3, c_4, c_5, c_6 are constant coefficients which can be calculated by satisfying boundary conditions **4-21** and **4-22**,

$$c_1 + c_3 + c_4 + c_5 + c_6 = 0, \qquad \textbf{[4-25a]}$$

$$c_2 + c_3\lambda_1 + c_4\lambda_2 + c_5\lambda_3 + c_6\lambda_4 = 0, \qquad \textbf{[4-25b]}$$

$$c_3\lambda_1^{\,2}e^{\lambda_1} + c_4\lambda_2^{\,2}e^{\lambda_2} + c_5\lambda_3^{\,2}e^{\lambda_3} + c_6\lambda_4^{\,2}e^{\lambda_4} = 0, \qquad \textbf{[4-25c]}$$

$$c_3\lambda_1^{\,3}e^{\lambda_1} + c_4\lambda_2^{\,3}e^{\lambda_2} + c_5\lambda_3^{\,3}e^{\lambda_3} + c_6\lambda_4^{\,3}e^{\lambda_4} = 0, \qquad \textbf{[4-25d]}$$

$$\left(c_3\lambda_1^{\,4} + c_4\lambda_2^{\,4} + c_5\lambda_3^{\,4} + c_6\lambda_4^{\,4}\right) + i\,\alpha^2\omega_r\left(c_1 + c_3 + c_4 + c_5 + c_6\right) = 0, \quad \textbf{[4-25e]}$$

$$\begin{aligned}&\left(c_3\lambda_1^{\,5}e^{\lambda_1} + c_4\lambda_2^{\,5}e^{\lambda_2} + c_5\lambda_3^{\,5}e^{\lambda_3} + c_6\lambda_4^{\,5}e^{\lambda_4}\right)\\ &\quad + i\,\alpha^2\omega_r\left(c_2 + c_3\lambda_1 e^{\lambda_1} + c_4\lambda_2 e^{\lambda_2} + c_5\lambda_3 e^{\lambda_3} + c_6\lambda_4 e^{\lambda_4}\right) = 3\alpha^2\end{aligned}. \quad \textbf{[4-25f]}$$

The system of linear algebraic Eqs. **4-25(a-f)** may be solved analytically or numerically for the six constant coefficients. Substituting Eq. **4-23** into **4-19**, one finds that the solution for $u^0\left(x^*\right)$ is

$$u^0\left(x^*\right) = \frac{1}{3\alpha}\left[\begin{aligned}&\left(c_3\lambda_1^{\,4}e^{\lambda_1 x^*} + c_4\lambda_2^{\,4}e^{\lambda_2 x^*} + c_5\lambda_3^{\,4}e^{\lambda_3 x^*} + c_6\lambda_4^{\,4}e^{\lambda_4 x^*}\right)\\ &\quad + i\alpha^2\omega_r\left(c_1 + c_2 x^* + c_3 e^{\lambda_1 x^*} + c_4 e^{\lambda_2 x^*} + c_5 e^{\lambda_3 x^*} + c_6 e^{\lambda_4 x^*}\right)\end{aligned}\right] \quad \textbf{[4-26]}$$

Finally, the dimensionless time-dependent structural element displacement, $y^*\left(x^*,t^*\right)$, and fluid velocity, $u^*\left(x^*,t^*\right)$, are obtained by substituting Eqs. **4-23** and **4-26** into Eqs. **4-16a** and **4-16b**.

An interesting special case to consider is that of steady shear, wherein $\frac{\partial y^*}{\partial t^*}$ vanishes. Hence, Eqs. **4-12** and **4-13** reduce to

$$\frac{d^4 y^*}{dx^{*4}} = 3\alpha u^*, \qquad \textbf{[4-27]}$$

and

$$0 = \frac{d^2 u^*}{dx^{*2}} - \alpha^2 u^*. \qquad \textbf{[4-28]}$$

The steady state boundary conditions corresponding to Eqs. **4-14** and **4-15** are

$$y^*(0) = \frac{dy^*}{dx^*}(0) = u^*\left(0\right) = 0, \qquad \textbf{[4-29]}$$

$$\frac{d^2 y^*}{dx^{*2}}(1) = \frac{d^3 y^*}{dx^{*3}}(1) = 0 \quad \text{and} \quad \frac{du^*}{dx^*}(1) = \alpha. \qquad \textbf{[4-30]}$$

The coupled ordinary differential Eqs. **4-27** and **4-28** may be solved with boundary conditions **4-29** and **4-30** to yield

$$u^*\left(x\right) = \frac{\sinh\left(\alpha x^*\right)}{\cosh\left(\alpha\right)}, \qquad \textbf{[4-31]}$$

and

$$y^*\left(x^*\right) = \frac{3\sinh\left(\alpha x^*\right)}{\alpha^3\cosh\left(\alpha\right)} - \frac{3x^*}{\alpha^2\cosh\left(\alpha\right)} + \frac{3}{2}\left(1 - \frac{\tanh\left(\alpha\right)}{\alpha}\right)x^{*2} - \frac{x^{*3}}{2}. \qquad \textbf{[4-32]}$$

4.4. Parameter Values

The two key dimensionless parameters that emerge from the analysis are the permeability parameter α that appears in the Brinkman equation and ω_r, the dimensionless frequency that appears in the equation for the vibration of the structural elements. The key parameters that need to be calculated in the estimation of these dimensionless groups for the three applications of interest, core proteins in the endothelial glycocalyx, microvilli in brush border epithelium and cilia in the cortical collecting duct, are K_P, the Darcy permeability and ω_c, the fundamental frequency for the oscillation of the structural element in a viscous fluid. In Table **4-I** we have summarized the physiological values of the parameters or the range of values that enter into this calculation. In general, K_P, and hence α, can be determined from Eq. **4-4** once the dimensions of the structural elements and their spacing are specified. In all three cases we assume that the structural elements form an hexagonal array in cross-section. To determine ω_c one requires estimates of the bending rigidity EI in addition to these ultrastructural parameters. The latter is calculated for core proteins in Weinbaum et al.[2], for proximal tubule microvilli in Guo et al. (2000) and measured values for primary cilia in the CCD are given in (Welling and Welling 1975). The calculated values for EI for core proteins are derived from a model for the time dependent restoration of the glycocalyx after the passage of a white cell using time dependent measurements of its thickness in Vink and Duling (1996). The calculated values for EI for brush border microvilli are determined from a basic model for the actin filament structure described in Guo et al. (2000) and measured values for EI for individual actin filaments.

Results will be presented for a shear stress of 1 dyn/cm^2 since all velocities and deformations can be easily scaled to this value. This scaling is linear since for small deflections of the structural elements the governing equations are linear. One observes in Table I that the physiological shear stresses are roughly of this magnitude in the kidney tubule and are approximately one order of magnitude larger for vascular endothelium. One observes at the bottom of Table I that α for cilia are typically of ~1, whereas for core proteins and microvilli it is typically ~10^2. The characteristic frequency for the natural vibration of primary cilia is of ~10 rad/s, whereas the natural frequency for the vibration of either a core protein or microvillus is somewhere between 10^4 and 10^5 rad/s. A typical forcing frequency for vascular flow is 1 Hz and many experiments in flow chambers, where the response of cells to cyclic loading are conducted, are at this frequency. Results for the fluid velocity and the time dependent deformation of the structural elements will be presented for this frequency. However, the more general results for the torque and the phase of the fluid and structural response to the applied fluid shear will be presented as a function of the dimensionless frequency ω_r.

4.5. Results

We first consider the velocity distribution and fiber deflection when the apical surface layers (brush border, endothelial glycocalyx or cilia layer) experience steady shear. For steady flow both the velocity field, Eq. **4-31**, and the deformation of the structural elements, Eq. **4-32**, depends only on the Brinkman parameter α. The key velocity in analyzing the response of the fluid to the applied shear is the slip velocity

at the edge of the surface layer. In particular, one wishes to see how the presence of the structural elements causes this velocity to decrease as the Brinkman parameter α increases. This is best illustrated by introducing a new velocity scale, namely the velocity $U = \tau_0 L/\mu$ that would be achieved at the edge of the layers in the limit where α approached zero, or a simple Couette flow in which no structural elements were present, since this is the maximum velocity that could be achieved by the steady applied shear. This decrease in slip velocity with α is shown in Fig. **4-3(a)**. Also shown in this figure is the variation of the dimensionless characteristic velocity $u_c/U = \tau_0\sqrt{K_P}/(\mu U) = 1/\alpha$ that was introduced in the formulation. One observes that for $\alpha > 2$, the two curves are nearly indistinguishable. Thus, for $\alpha > 1$, which covers the entire range of physiological application for the structural element of interest in the present study, the edge velocity is well represented by u_c.

To examine the velocity profiles we return to the velocity scale u_c. The dimensionless velocity profiles u/u_c are shown in Fig. **4-3(b)** for three representative values of α. One observes that the fluid motion induced by the applied shear penetrates all the way to the apical membrane for $\alpha = 1$, and that for $\alpha > 10$ a tip interaction or boundary layer develops at the edge of the surface layer.

The results for the fiber deflections for steady shear are shown in Fig. **4-4** for α=1, 10 and 100. We can see from these figures that y_c in Eq. **4-11** provides a good scale for the tip deflection for $\alpha = 10$ and 100, since $y/y_c \approx 1$ at *x/L*=1, while for $\alpha = 1$, the scale for the tip deflection in Eq. **4-11** is about five times too large since $y/y_c \approx 0.2$ at *x/L*=1. This occurs because the fluid drag is no longer concentrated at

the tips of the structural elements. However, y_c is also a function of solid fraction *c*, as shown in Eq. **4-11**. To isolate the effect of α, a new scale for the tip deflection, $Y = \frac{\tau_0 \cdot \pi r_f^2 \cdot L^3}{3EI}$, is used in Fig. **4-4(b)**. The difference between *Y* and y_c is that *Y* is the deflection induced by the shear stress τ_0 acting on the tip end, whose surface is πr_f^2 while y_c is the deflection induced by the shear stress τ_0 acting on the effective unit area $\pi r_f^2 / c$, which includes the surrounding fluid. To relate α and *c*, a representative value of L/r_f must be selected. Table **4-I** indicates $L/r_f = 30$ is suitable for all three cases. Fig. **4-4(b)** shows that with this new scale *Y* the tip deflection monotonically decreases as α increases. Rearranging Eq. **4-11**, one has $y_c / L = \tau_0 / (3\mu\omega_c)$. Therefore, the scale of fiber deflection is proportional to the applied surface stress, τ_0, and is inversely proportional to the natural beam frequency, ω_c. However, Eq. **4-1** limits us to the region of linear deflection, where at most $y(L)/L \le 1/3$. Hence, to make sure the analysis based on Eq. **4-1** is valid, the fibers should be sufficiently rigid. This requires that there be a minimum value of ω_c corresponding to each τ_0. For instance, for $\tau_0 = 1\ \text{dyn/cm}^2$ ω_c should not be smaller than *100* rad/s for $\mu = 10^{-3}\ P_a \cdot s = 1\ \text{cp}$. Note that for $\alpha = 1$ the minimum value of ω_c is about 20 rad/s since the scale of the deflection, see Fig. **4-4**, is about 1/5 the characteristic deflection y_c. From Table **4-I** one observes that the results for core proteins and brush border microvilli easily satisfy this constraint, but the results for the deflection of primary cilia lie at the margin of validity of small deflection theory.

One important physiological frequency is the contraction and relaxation of the heart, which operates at around 1 Hz or 2π rad/s for humans. Hence, we choose 1 Hz as the dynamic frequency for the results in Figs. **4-5**, **4-6** and **4-7**. Since $\omega_r = \omega/\omega_c$ there is a maximum ω_r for each ω to satisfy the constraint of small deflection theory. Thus, if $\omega = 1\,\text{Hz}$, $\tau_0 = 1\,\text{dyn/cm}^2$ and the deformation of the structural elements are to satisfy the constraint that $y(L)/L \le 1/3$, then the maximum ω_r at 1 Hz is $2\pi/20$ for $\alpha = 1$ and $2\pi/100$ for $\alpha = 10$ and 100. It will be shown later that both the fluid and the surface structures exhibit a quasi-steady behavior unless ω_r exceeds a critical value. Therefore, we will want to compare this critical value with the maximum ω_r for different α.

The results in Figs. **4-5**~**4-7** show our theoretical predictions for (a) the fluid velocity distribution u/u_c along the length of fibers, (b) the local deflection velocity of the structural elements, (c) the local relative velocity between fluid and these elements and (d) their resultant deflection for $\alpha = 1$, 10 and 100 when $\omega = 1\,\text{Hz}$. In Fig. **5**, $\alpha = 1$ and $\omega_c = 10$, values of characteristic of cilia, we observe in Fig. **4-5(a)** that the fluid velocity distribution is in phase with the applied shear stress and the amplitude of this motion is the same as for the steady flow in Fig. **4-3(a)** for $\alpha = 1$. The relative velocity between the fluid and the structural elements in Fig. **4-5(c)** is nearly the same as the fluid velocity profile since the vibration velocity of the structural elements in Fig. **4-5(b)** is small compared to the fluid velocity. The deflection of the structural elements in Fig. **4-5(d)** exhibits a quasi-steady behavior since the relative velocity between the fluid and the structural elements is in phase with the applied shear. For larger values of

ω_c, or stiffer elements, the deflection of the elements, and hence their velocity would be still smaller and they would have an even less significant influence on the velocity profile of the fluid. In effect, for $\alpha = 1$ the structural elements are too far apart for their deflection to have a significant influence on one another. To demonstrate the effect of increasing the concentration of the structural elements, we consider in Fig. **4-6** the fluid motion and deformation for $\alpha = 10$ and $\omega_c = 100$. In this case we observe an important transition in behavior. The velocity of the structural elements in Fig. **4-6(b)** is no longer vanishingly small and this produces a significant perturbation on the velocity field in Fig. **4-6(a)**. The motion of the structural elements is $\pi/2$ out of phase with the fluid velocity field and is of sufficient magnitude to induce fluid motions that are non-vanishingly small at $\pi/2$ and $3\pi/2$. The motion of the structural elements is due to their elastic restoring force from their position of maximum displacement and this is the origin of the $\pi/2$ difference in phase between the profiles in Figs. **4-6(b)** and **4-6(d)**. The structural elements have their smallest velocity at their position of maximum displacement. However, the motion of the structural elements drags the fluid with them and there is only a small relative motion of the fluid and the structural elements within the surface layer, except as one approaches the tip region where the applied shear overwhelms any motion due to the fibers. Since it is the relative velocity that drives the deformation of the structural elements, the deformation profiles in Fig. **4-6(d)** qualitatively resemble those in Fig. **4-5(d)**.

The tendencies just described for $\alpha = 10$ are accentuated when $\alpha = 100$ and $\omega_c = 100$ in Fig. **4-7**. The structural elements in the surface layer are sufficiently closely spaced for the applied shear to generate only negligible fluid velocities (0 and π

profiles in Fig. **4-7(a)**) except in a thin tip interaction layer where the slip velocity u_c is quite small. The elastic recoil of the structural elements, depending on their bending rigidity, can produce a velocity which can even exceed the small slip velocity produced by the applied shear as shown by the $\pi/2$ and $3\pi/2$ curves in Fig. **4-7(b)**. The recoiling structural elements carry the fluid with them, as shown by the $\pi/2$ and $3\pi/2$ curves in Figs. **4-7(a)** and (**b)**, and there is no relative motion of the fluid and solid phases except for the small slip velocity at the layer edge, Fig. **4-7(c)**. Since it is only this relative velocity that produces the deformation of the structural elements, their deformation in Fig. **4-7(d)** is in phase with the applied shear. The drag due to this shear acts as a point force applied at the end of a cantilever beam and produces the torque required for its deflection.

The foregoing behavior is possible when the structural elements are quite flexible. For more rigid structural elements we have plotted the equivalent results for $\alpha = 100$ and $\omega_c = 10^4$ in Fig. **4-8**. In this case the structural elements are too stiff to significantly deform and the fiber velocities generated are small compared to the fluid slip velocity produced by the applied shear. The structural elements are essentially rigid structures and their small deformation is again in phase with the applied shear force. This behavior is characteristic of the core proteins in the glycocalyx and brush border microvilli.

The resultant torque on the structural elements normalized by its corresponding value in steady flow is examined for α=1, 10 and 100 in Fig. **4-9**. Note that it is the relative velocity that determines the resultant drag force and torque on the structural elements, as shown in Eq. **4-2**. One observes that all curves collapse into a single

curve for $\omega_r < 1$. This is not unexpected since the results in Figs. **4-5(c)** through **4-8(c)** for the relative velocity profiles show little deviation from the quasi-steady profiles for all α and ω_c in the physiological range for $\omega = 1$ Hz. The maximum value of ω_r shown in Figs. **4-5** to **4-8** is $2\pi/10$ or 0.628. For higher values of ω_r, the critical value of ω_r at which the normalized torque deviates from unity, increases with decreasing α. For $\alpha \geq 10$, the curve for the normalized torque becomes independent of α. This behavior can be explained by examining Eq. **4-20**. One finds that the sixth derivative term is negligibly small for $\alpha \geq 10$ and the parameter α cancels out of the equation making the solution for y_c independent of α. For $\alpha \geq 10$ the normalized torque decreases rapidly as ω_r increases for $\omega_r \geq 1$.

In Figs. **4-10** and **4-11** we examine how the phase and magnitude of the fluid velocity, the structural element velocity, and the relative velocity between the two at the tip of the element ($x = L$) vary as a function of ω_r for α=1, 10 and 100, respectively. After the start-up transients decay, there exists a phase angle, δ, associated with each kinematic variable whose time-dependence is of the form $\cos(\omega t - \delta)$ when the oscillating applied shear force is $\cos(\omega t)$. In these figures, one observes that when $\omega_r << 1$ the fluid velocity and the relative velocity are in phase with the applied shear force while the tip velocity of the structural element lags the applied shear force by $\pi/2$ since the elements move with maximum velocity at their equilibrium position. However, when ω_r increases, the motion of both the fluid and the structural elements deviate from quasi-steady state behavior. The phase angle of the tip velocity of the elements increases and this contributes to the fluid motion. This

interaction causes the relative velocity to move out of phase with the applied shear force, and consequently, also the torque. Large deviations between the phases of the relative velocity and the applied shear stress occur for $\omega_r > 1$. The principal difference between Figs. **4-10(a-c)** is that the phase angle for fluid motion, the solid curves, indicates that the local minimum in the phase curves moves up the frequency spectrum and become progressively more attenuated as α decreases. The results for the magnitudes of the kinematical variables in Figs. **4-11(a-c)** change in parallel with the results for the phases in Figs. **4-10(a-c)**. For $\omega_r << 1$, the structural element velocity is negligible compared to the fluid velocity. Hence, the relative velocity are same as the fluid velocity. For $\omega_r > 1$, the relative velocity begins to diminish since the fluid velocity and the structural element begin to move closely in both phase and magnitude. So does the torque transmitted, as shown in Fig. **4-9**.

4.6. Discussion

The structural elements in the apical surface layers, such as the ore proteins in the glycocalyx on vascular endothelial cells, microvilli in the proximal tubule and cilia in the cortical collecting duct, have been proposed to serve as mechanotransducers that sense fluid shear (Florian et al. 2003; Guo, Weinstein and Weinbaum 2000; Liu et al. 2003; Praetorius and Spring 2001; Secomb et al 2001; Weinbaum et al. 2003). In this study we examine the response of these structures to both steady and pulsatile fluid shear using two key structural parameters: a dimensionless Brinkman parameter, $\alpha = L/\sqrt{K_P}$, and a dimensionless frequency parameter, ω_r, which is scaled by the natural frequency of the damped vibration of the structural element, ω_c, in a viscous

fluid. Furthermore, for the pulsatile case we focus on the transient hydrodynamic interaction between the fluid and the structural elements and the resultant torque on the structural elements when the surface layers experience sinusoidal shear.

We will first discuss the case of steady shear. As shown in Table **4-I**, the core proteins of the endothelial glycocalyx, the microvilli in the brush border and the cilia in the CCD differ greatly from each other in dimensions and spacing. However, using effective medium theory to model the fluid confined in the surface layer, one can combine these structural factors into a single parameter, the dimensionless Brinkman parameter α. Our results, see Eqs. **4-31** and Figs. **4-3(a)** and **4-3(b)**, show that the scaled fluid velocity depends only on α. For cilia, the dimensionless Brinkman parameter is ~ 1. The fluid velocity scale and velocity profile, see Figs. **4-3(a)** and **4-3(b)**, are close to the results for a simple Couette flow, since the structural elements are loosely spaced and have a relatively small effect on the fluid flow. For the endothelial glycocalyx and the brush border microvilli, the dimensionless Brinkman parameters are ~ 100. For these structural elements, the scale of the slip velocity at the edge of the layers is two orders of magnitude smaller than that for cilia due to the hydrodynamic interaction of the structural elements in the densely spaced matrix layer. A tip interaction or boundary layer appears at the outer edge and the fluid velocity vanishes rapidly in this tip layer. Consequently, the endothelial or epithelial cell membrane feels almost vanishing fluid shear stress. The results for the brush border, endothelial glycocalyx and cilia correspond to the results previously reported (Damiano 1998; Guo et al. 2000; Liu et al. 2003; Secomb, Hsu and Pries 2001; Weinbaum et al. 2003) However, there is no slow bulk flow in the deep region of the

matrix layers in the current case, since the motion here is driven only by surface shear stress and there is no an axial pressure gradient.

Despite the above differences, these surface layers were proposed to perform a similar role as a mechanotransducer. The common mechanism is that the structural elements are sufficiently rigid in their respective fluid environments to deform only modestly to fluid shear stress in the physiological range. This limited deformation enables them to transfer the drag force or torque to the intracellular cortical cytoskeleton with little attenuation. This rigidity is characterized by the natural frequency for the damped vibration of the structural element, ω_c. For small deflection theory to be valid for shear stresses typical of these surface layers, see Table I, the minimum values of ω_c are 1000 rad/s for the core proteins in the endothelial glycocalyx and the microvilli in the brush border and 10 rad/s for cilia the CCD. The values of ω_c in Table I show that the deflections of the core proteins and microvilli fall within the limits of small deflection theory while the deflections of cilia longer than 4 μm could well lie outside this range and should be examined using "elastica" theory as Schwartz et al.(1997). Liu et al. (2003) use small deflection theory for cilia up to 8 μm in length since the tip shear force in their experiments is only of the order of 0.1 dyn/cm^2. Despite their difference in size we note in Table I that α and ω_c are of the same order for core proteins and microvilli. In the case of the ESL, Secomb et al. (2001) proposed an alternative mechanism of fluid shear stress transmission. They assumed the stiffness of the ESL is due to the oncotic force induced by proteins trapped in the matrix. Thus the fluid shear stress is transmitted to the endothelial cell membrane as a surface traction via the ESL when they are tilted relative to the normal

by the shear force acting at the edge of the ESL. In the model proposed by Weinbaum et al. (2003) and used herein, the fibers have a bending rigidity *EI* and the fluid shear stress is transmitted, not to the cell membrane, but directly to the underlying actin cortical cytoskeleton via short linker molecules, such as talin and vinculin. The contrast and feasibility of the two mechanisms is discussed in Weinbaum et al. (2003) The main argument against the oncotic model is that transport experiments examining the role of the ESL as a molecular sieve in establishing the starling force balance indicate that there is a sharp drop in protein concentration across the ESL which would cause a dehydration rather than a swelling of the ESL (Hu et al. 2000).

Pulsatile flow does not normally occur in capillaries or post capillary venules and is mostly damped by viscosity in arteries where the pressure pulse is typically about one mm Hg. While the endothelial glycocalyx has been observed *in vivo* only in microvessels, there is strong evidence that it is present throughout the vasculature, and was first observed *in vitro* in large arteries (Luft 1966) where the pressure pulse is very substantial. The present results in Fig. **4-8** for one Hz are, thus, representative of the behavior that would be anticipated in these large blood vessels where the pressure pulse is only slightly damped. Moreover, some sites in arteries, such as the inner walls of arterial curvature and outer walls of arterial bifurcation (side opposite the flow divider), experience significant oscillations in shear stress and are most likely to develop atherosclerotic plaques (Ku et al. 1985; Qiu and Tarbell 2000) These areas have been shown to be associated with low shear, flow separation and flow reversal. In kidney tubules pulsatile flow does occur but only at very low flow rates. Schmidt-Nielsen and Graves (1982) first demonstrated more than 20 years ago that pelvic

contractions associated with peristalysis in the ureter fed upstream into the papilla where the CCDs emptied and that these peristaltic motions caused a rhythmic pulsation of flow in the tubules. These flow oscillations had a frequency of ten/min or 0.17 Hz. The value of ω_r in the last row of Table 1 is, thus, six times that describing these slow flow oscillations in the kidney tubule. In addition to these physiologically meaningful flow oscillations, one is also interested in *in vitro* experiments on cultured cells in shear chambers in which these apical surfaces experience oscillating shear in order to explore the frequency response of the cell to changes in flow rate or the start-up effect of flow in experiments.

Since the structural elements in these surface layers are also present in other cells where they might perform a mechanosensory function, it is of general interest to ask how the torque amplitude changes with the applied frequency. At 1 Hz, cilia, core proteins and microvilli and their surrounding fluid move in a quasi-steady motion, see Figs. **4-5** and **4-8**. Consequently, our model predicts no attenuation or phase shift in torque at 1 Hz. Figure **4-9** shows that for cilia ($\alpha = 1$) the critical dimensionless frequency $\omega_r = \omega/\omega_c$ at which attenuation in torque begins to occur is 10. For small deflection theory to be valid, the minimum ω_c for cilia is 10 rad/s at physiological shear rates, see previous discussion and Table **4-I**. Hence, the minimum critical applied frequency ω at which the torque is attenuated is 100 rad/s or 16 Hz, a frequency much greater than the rhythmic contractions described in the last paragraph. Figure **4-9** also shows that the critical dimensionless frequency becomes independent of α for $\alpha > 10$ and that for $\alpha > 10$, ω_r has to be >1 for this attenuation to occur. For core proteins and microvilli $\omega_r = 1$ when ω is of the order of 10^4 to 10^5 rad/s or 10^3 to

10^4 Hz, see Table **4-I**. Clearly, frequencies in this range are not of practical importance. Note that in the case of the ESL a similar attenuation of dynamic fluid shear stress stimuli was previously reported by Secomb et al. (2001) using different assumptions for the origin of ESL rigidity.

Finally, we are concerned with the phase relation between the fluid and fiber motion and torque with the frequency of the applied shear and, similarly, their magnitude. For cilia with a natural frequency, $\omega_c = 10$ rad/s, the fluid velocity at the cilia tips is in phase with the applied shear force up to frequencies of 10 rad/s, while the cilia tip velocity is out of phase with the applied shear by $\pi/2$ in this range, see Fig. **4-10(a)**. Since the structural element velocity is small compared to the fluid velocity, the relative velocity has nearly the same magnitude as the fluid velocity. Thus, the relative velocity is also in phase with the applied shear force up to 10 rad/s, and hence, so is the torque. However, for cilia with a natural frequency, $\omega_c = 10$ rad/s, the relative velocity is out of phase with the applied shear when $\omega > 100$ rad/s and its magnitude diminishes since the structural elements partially follow the fluid motion in this frequency range. If the highest practical applied frequency ω is 100 Hz or 628 rad/s, the maximum dimensionless frequency ω_r is about 0.1 for core proteins and microvilli. In this frequency range, the relative velocity at the tips of the elements and the torque are in phase with the applied shear force and their magnitude does not change, see Figs. **4-10(c)** and **4-11(c)**. However, for $\omega > 100$ rad/s the fluid velocity at the tips of the elements is markedly out of phase with the applied shear and increases in magnitude because the densely packed core proteins or microvilli transport substantial fluid with them. Note that for cilia the loosely spaced matrix can not

transport a significant amount of fluid over the entire frequency range. This is shown in Figs. **4-10(a)** and **4-11(a)** where one observes that the phase of the fluid velocity at the tips is close to the phase of the applied shear and its magnitude does not change over the entire frequency range.

In concluding this paper we closed with a cautionary statement. While Fig. **4-1(b)** provides a reasonable morphological structure for the ESL, there is no consensus as to the organization of the gluco and glycosaminoglycans (GAG) that are attached to the core proteins that comprise the ESL or even the thickness of the ESL. The latter has been estimated to vary from 100-200 nm in frog microvessels (Squire et al. 2001) to 400 nm in mammalian capillaries (Vink and Duling 1996). Squire et al. (2001) are careful to point out that in chemical fixation there is significant shrinkage due to dehydration and that the thickness observed in frog, typically 50-100 nm, is only about half the 100-200 nm thickness observed in rapid free etching. Heparan sulfate (HS), a glucosaminoglycan, is the most abundant GAG associated with endothelial proteoglycans. There are four forms of HS proteoglycans, syndecans 1-4, with sydecan-1 being associated with the apical surface and leukocyte adhesion (Ihrcke, et al. 1993) and syndecan-4 playing an important role in focal adhesion formation on the basal aspects of the endothelial cell (Bass and Humphries 2002). All syndecans have an extracellular proteolytic cleavage site in close proximity to their transmembrane domains and this may account for the different appearance of the ESL when viewed in electron micrographs with different fixation methods. The extracellular domains of the syndecans are of variable length and this length depends on the number of GAGs attached to the core proteins. Thus, it is likely that ESL thickness is tissue and species

dependent. It is also possible that the core proteins are cross-linked by the GAG. However, if the quantitative predication for the bending rigidity *EI* of the core in Weinbaum et al. (2003) are of the right order then it unlikely that such cross-linking will occur since this would provide an added stiffness to the ESL which would prevent its observed collapse during red cell arrest (Vink and Duling 1996).

4.7 Footnotes

This chapter is reprinted with permission from Han, Y., Ganatos, P. and Weinbaum, S. (2005) "Transmission of steady and oscillatory fluid shear stress across epithelial and endothelial surface layers." *Phys. of Fluids* **17**: 031508(1-13).

Chapter 5 Mechanotransduction and Strain Amplification in Osteocyte Cell Processes

5.1. Introduction

A fundamental paradox in bone tissue is that tissue level strains in whole bone due to animal and human locomotion are typically < 0.2 percent (Fritton, McLeod and Rubin 2000; Rubin and Lanyon 1984), yet an extensive range of *in vitro* experiments in bone (Burger and Veldhuijzen 1993; Smalt et al. 1997; You et al. 2000) and other tissue cultures (Almekinders, Banes and Ballenger 1993; Guilak, Ratcliffe and Mow 1995) show that dynamic substrate strains must be at least an order of magnitude larger for intracellular biochemical responses to occur. Such large whole tissue strains *in vivo* would cause bone fracture. You et al. (2001) have recently proposed a new hypothesis and exploratory quantitative cellular level model which predicts that the fluid flow through the pericellular matrix in the lacunar-canalicular porosity due to small whole tissue deformations can induce cellular level strains in the actin filament bundles of the cell processes which are one to two orders of magnitude larger than whole tissue strains and sufficient to initiate intracellular signaling. This model was intended to demonstrate the quantitative feasibility of the basic hypothesis and not realistically simulate the strain amplification mechanism, since there was only fragmentary and sometimes contradictory evidence with regard to the key structural components of osteocytes that would be necessary for the model to work *in vivo*. In addition, there was no information on the most important mechanical properties in the system, i.e., the flexural rigidity EI of the transverse filaments in the pericellular space

and the sieving characteristics of the pericellular matrix. You et al. (2001) treat these filaments as inextensible strings with no flexural rigidity.

The four basic structural components in the model are (i) transverse filaments in the pericellular matrix that anchor and center the osteocyte process within its canaliculus; (ii) an organic matrix attached to the transverse filaments that fills the entire pericellular space surrounding the osteocyte and its cell processes, and which would exert a flow-induced drag force on the transverse filaments; (iii) a cytoskeletal structure within the cell processes to resist hoop tensions and bending deformation and (iv) transmembrane proteins and other linker molecules which transmit the flow induced tension in the transverse filaments to the actin cytoskeleton in the cell process.

The recent ultrastructural study by You et al. (2004) has provided the first detailed information on these structural components in and around osteocytes in adult bone. In particular, the study unequivocally demonstrated the existence of the transverse tethering filaments in the pericellular space and the first measurements of their spacing and distribution. The study also elucidated for the first time in bone tissue the spacing and arrangement of the actin filaments in the cross-section of the cell process. Morphologically, this central actin filament bundle is very similar in appearance to the bundle that has been extensively studied in the brush border microvilli of the small intestine (Matsudaira and Burgess 1982; Mooseker and Tilney 1975). The cell process consists of 15-20 central axial actin filaments, surrounded by a 25 nm annulus in which there is presumably a filament-membrane complex via which the central filament bundle is attached to membrane proteins that link the cytoskeleton to the extracellular matrix. The immunocytochemical studies of Tanaka-Kamioka et al.

(1998) on isolated embryonic chick calvarias, show a nearly uniform labeling of the cell process by fimbrin, a cross-linking molecule which is known to cross-link actin filaments with parallel polarity (Volkmann et al. 2001). There was also localized labeling of α-actinin, but the latter was primarily associated with stress fibers in the cell body which have an antiparallel polarity.

The close similarity between the three-dimensional cytoskeletal organization of the osteocyte cell process and intestinal microvilli was not realized when the model in You et al. (2001) was published. The slender cell processes are an order of magnitude longer in osteocytes than intestinal microvilli, and the studies of Tanaka-Kamioka et al. (1998) considered only planar arrangements of cells where the osteocyte processes were observed primarily *en face* in field emission scanning electron microscopy rather than in cross-section. Subsequently, Weinbaum et al. (2001) presented a comparative study of possible mechanotransduction mechanisms in renal and intestinal microvilli, stereocilia in the ear and bone cell processes. The fundamental difference is that in the first three cell types with actin rich projections, hydrodynamic loading causes a bending along the long axis of the cellular projections, whereas in bone cells the strain amplification hypothesis in You et al. (2001) assumes it occurs through a hoop tension that is generated in the cross-section of the process since the processes are encased in nearly rigid tubes with minimal bending deformation.

Important new information has also been obtained recently concerning the sieving properties of the pericellular matrix and hence the spacing of the glycosaminoglycan (GAG) side chains of the proteoglycans in the pericellular space.

Both Wang et al. (2004) and Knothe-Tate (2001) have found that the sieve lies somewhere between HRP, 6 nm diameter, and ferritin, 10 nm diameter. The cutoff in size appears to lie very close to 7 nm, the molecular sieve size for albumin in the endothelial glycocalyx of capillaries (Hu et al. 1994; Michel 1997; Weinbaum 1998). This spacing is a key input in determining the hydrodynamic drag on the tethering filaments. Finally, model calculations for the flexural rigidity of the core proteins of proteoglycans, the structural component believed to represent the transverse filaments, predict a value for *EI* of 700 pN•nm^2 (Weinbaum, et al. 2003).

The foregoing advances have set the stage for a much more realistic, ultrastructurally-based model for strain amplification in bone. In this study we shall first develop a three-dimensional model for the osteocyte process with a 19 element actin filament bundle whose organization is modeled after the fimbrin cross-linked hexagonal structure observed in stereocilia (DeRosier, Tilney and Egelman 1980) and microvilli (Volkmann et al. 2001). To our knowledge this is the first attempt to analyze the force distribution in hexagonally packed actin filament bundles with helically arranged fimbrin crossbridges. We then apply large amplitude deformation theory for 'elastica' to predict how the hoop strains in the osteocyte process vary as a function of the transverse element flexural rigidity, *EI*, and the tissue loading and frequency. We find that the value of *EI* has a subtle influence on the hoop tension that is transmitted to the core bundle of the cell process. We also propose that the present theory for cellular level strain amplification provides a more likely hypothesis for the excitation of osteocytes than the fluid shear hypothesis previously proposed in Weinbaum, Cowin and Zeng (1994).

5.2. Methods

Structural Model: Figs. **5-1(a~d)** are sketches of our idealized model for the internal structure of the osteocyte process and its attachment to the canalicular wall by the transverse elements as seen in both radial, Fig. **5-1(a)**, and longitudinal cross section, Fig. **5-1(b)**, respectively. The central filament bundle inside the cell process is an hexagonal array of 19 actin filaments (You, et al. 2004), which are attached to unknown integral membrane proteins (You et al. 2001; You et al. 2004) in the cell process membrane by cross-filaments equivalent to brush border myosin I in intestinal microvilli (Matsudaira and Burgess 1982). Adjacent actin filaments with 12 nm spacing are periodically crosslinked by fimbrin in an hexagonal pattern. Along each actin filament, the fimbrin crosslinks rotate 60 degrees counter-clockwise and advance 12.5 nm axially in successive crosslinking positions as proposed in DeRosier et al. (1980) and Volkmann et al. (2001), see Fig **5-1(c)**. The cross-filaments surrounding the core bundle spiral in a double helical coil around the core bundle with a 37.5 nm spacing between each coil, see Fig. **5-1(d)**, which is similar to the spacing observed for brush border myosin I in intestinal microvilli (Matsudaira and Burgess 1982). Since there are 12 actin filaments in the outermost ring, each coil advances 6.25 nm between successive outer actin filaments (75 nm in a single rotation). The transverse elements attach the osteocyte process to the canalicular wall and center it in the canaliculus. The integral membrane proteins are the sites where individual cross-filaments are connected with each transverse element (You et al. 2004). This implies that the transverse elements are also arranged in a double helix with a 37.5 nm spacing

along the axial direction of the canaliculus. Note that this spacing is consistent with the measured value of 38 nm in You et al. (2004). The transverse elements with their GAG side chains fill the annular space between the cell membrane and the canalicular wall. These side chains are assumed to have a 7 nm spacing (Knothe Tate 2001; Wang et al. 2004; You et al. 2001), and thus form a molecular sieve which prevents the loss of albumin (7 nm diameter) to the bone tissue space. The radii of the osteocyte process and canaliculus are 52 nm and 130 nm, respectively (You et al. 2004).

Mathematical Model for the Deformed Transverse Elements: In You et al. (2001) a simplified model is developed for the deformation of the transverse filaments that tether the cell process to the canalicular wall. The hydrodynamic loading on these tethering elements is produced by the fluid flow through the GAG filled annular space surrounding the cell process, as shown in Fig. **5-2**. The GAG side chains are attached to the tethering filaments and the drag on these side chains is transmitted to the filament much like the wind blowing through the needles on a pine tree. In You et al. (2001) the deformed shape of the tethering filaments is easy to determine since the loading per unit length of tethering filament, w, is uniform and they are treated as inextensible strings with $EI = 0$. For these assumptions the deformed shape is a simple catenary, the same as a hanging chain with uniform loading in a gravitational field.

In the present model a more elaborate theory is required to determine the deformed shape of the tethering filament since its finite flexural rigidity is considered. Furthermore, large deformation theory is required since relatively small displacements of the ends of tethering filaments at the cell process membrane can lead to large lateral

deflections of the filaments. We, therefore, use large amplitude deformation theory for 'elastica' (Frisch-Fay 1962) to determine the deformed shape of the tethering filaments due to the hydrodynamic loading. The one simplification that can still be retained is that the hydrodynamic loading w is still uniform. The hydrodynamic theory (Weinbaum et al. 1994) shows that the velocity profile in the pericellular matrix is nearly uniform except for very thin side wall fiber interaction layers at the canalicular wall and process membrane whose thickness is less than the GAG spacing (7 nm). These thin layers can be neglected. The governing equation from 'elastica' theory for the shape of the tethering element in Fig. **5-2** is given by

$$EI\frac{d^2\phi}{ds^2} = w(L_c - s)cos(\phi) + T_n\, sin(\phi). \qquad \textbf{[5-1]}$$

Here L_c is the length of an individual transverse element; T_n is the normal component of the tensile force at the canalicular wall, T, and $w \cdot L_c$ is its horizontal component; EI is the flexural rigidity of the core proteins. Note that the deflection of the transverse elements will cause the spacing, d, between the cell membrane and the canaliculus wall to decrease. d is given by

$$d = \int_0^{L_c} cos(\phi)ds\,, \qquad \textbf{[5-2]}$$

where we assume, as in You et al. (2001), that the tethering filaments are inextensible.

The key unknown in Eq. **5-1** is the hydrodynamic loading w on the transverse filament. This loading is determined from the hydrodynamic model presented in Weinbaum et al. (1994) for the fluid flow in the fiber filled fluid annulus surrounding

the cell process and the theoretical model in Zeng, Cowin and Weinbaum (1994) for the interstitial pressure distribution in the lacunar-canalicular porosity of an osteon. Using this combined theoretical model, You et al. (2001) were able to able to determine the drag force F_D on the transverse elements per unit length of the cell process. This model for calculating F_D is provided in *Appendix A*. The expression for F_D is a function of the lacunar-canalicular geometry and its Darcy permeability, K_P, the osteonal geometry, and the amplitude and frequency of the mechanical loading. The final expression for w is given by,

$$w = \frac{F_D \cdot L_f}{12 L_c}. \qquad \textbf{[5-3]}$$

Note that there are 12 individual transverse elements in a periodic unit of length L_f =37.5 nm along the axis of an individual cell process.

Mathematical Model for the Strain on the Osteocyte Process: To our knowledge no one has ever attempted to analyze the loading distribution within an hexagonally packed actin filament bundle with fimbrin crossbridges, although its geometrical organization has been studied extensively. In You et al. (2001) a much simpler radially symmetric actin filament arrangement is assumed with alternating crossbridges between adjacent actin filaments which lie in planes that pass through the axis of the central filament and there is no hexagonal organization of either the actin filaments or the fimbrin crossbridges. In the present model illustrated in Fig. **5-3** the fimbrin cross-links inside the bundle are subject to five different tensile forces, F_a, F_b, F_c, F_d and F_q, due to structural symmetry. The principle difficulty is that these forces do not act in the same cross-sectional plane due to the 60 degree, 12.5 nm axially

advancing rotation of the fimbrin crosslinks. This difference in plane of actin is distinguished by the dotted, dash-dot and solid lines in Fig.**5-3**.

A force balance on the actin filament shown as an open circle in Fig. **5-3**, and shown enlarged in the right hand force diagram, in direction *x* requires that

$$F_c - F_d = 2F_b \cdot sin(\pi/3) - 2F_a \cdot sin(\pi/3) = F_b - F_a \qquad \textbf{[5-4]}$$

However, $F_c = F_d$ if we assume that the fimbrin crossbridges are inextensible and these two forces are both opposite and act in the same cross-sectional plane. Therefore, from Eq. **5-4** $F_a = F_b$. Hence, the actin filaments in the interior of the bundle are not deflected since three pairs of equal but opposite forces act on them. This conclusion is true even if new layers of actin filaments are added to the bundle. In contrast, the actin filaments in the outer ring in Fig. **5-3** are asymmetrically loaded and have different loading depending on whether they are in a corner or central position in the outer ring. Figs. **5-4(a,b)** show the static force analysis on the outermost actin filaments at both corner and central positions, see also Fig. **5-3**. In Figs. **5-4(a**,**b)** T_n is the tensile force exerted by the cross filaments on the actin filament bundle; and F_a, F_c and F_q are tensile forces exerted by the fimbrin cross-links. The force balances in Figs. **5-4(a**,**b)** are used to obtain the maximum deflection of actin filaments in the *x* direction using classic small deflection theory for uniform beams (Gere and Timoshenko 1990). The actin filament in Fig. **5-4(a)** is treated as a beam with fixed ends due to its symmetric periodic loading, whereas the actin filament in Fig. **5-4(b)** is treated as a simply-supported continuous beam which is asymmetrically loaded. The details of these models can be found in *Appendix B*. For the actin filament at the outer corner in Fig. **5-4(a)**, the maximum deflection in the *x* direction δ_{m1} is given by

$$\delta_{m1} = \left(\frac{1}{192} - \frac{5q_r}{1296} \right) \frac{T_n L_f^{\,3}}{EI_a}, \qquad \textbf{[5-5]}$$

where $q_r = F_q/T_n$ and EI_a is the flexural rigidity of the actin filament. For the actin filament at the central position of the outer ring in Fig. **5-4(b)**, one finds that the maximum deflection in the *x* direction is

$$\delta_{m2} = \frac{T_n L_f^{\,3}}{324 EI_a}. \qquad \textbf{[5-6]}$$

In Eq. **5-5**, one has to also consider the lateral deflections of the actin filaments based on the force balance in the *y* direction shown in Fig. **5-4(a)** in order to obtain a relation between q_r and T_n. The details of this more elaborate analysis are provided in *Appendix B*. The force balance in the *y* direction in Fig. **5-4(b)** is not required since the sum of forces in this direction are equal and opposite and thus, cancel. Comparing Eqs. **5-5** and **5-6**, one observes that the overall maximum deflection of the outer actin filaments is given by Eq. **5-6** since q_r is > 0.6 in the relevant range, see Fig. **B-2** in *Appendix B*, and $\delta_{m2} > \delta_{m1}$. If the cross-filaments are inextensible, the maximum hoop strain is given by

$$\varepsilon_c = \frac{\delta_{m2}}{R_0} = \frac{d_0 - d}{R_0}, \qquad \textbf{[5-7]}$$

where R_0 is the original radius of the cell process and d_0 is the undeformed spacing between the cell process and the canalicular wall. Combining Eqs. **5-1**, **5-2**, **5-6** and **5-7**, we obtain the expression for the hoop strain in the cell process, ε_c, as a function of the hydrodynamic loading, *w*. From this expression, ε_c is also a

function of tissue loading since the hydrodynamic loading, *w*, is related to tissue loading, see Eq. **5-2** and *Appendix A*.

5.3. Parameter Values

The values of the parameters used in the model are shown in Table **5-I**, which were grouped as parameters for the hydrodynamic model, parameters for the canaliculus and cell process, and parameters for the central actin filament bundle.

5.4. Results

In Fig. **5-5** we plot the hoop strain of the osteocyte process as a function of loading frequency for a tissue loading σ of 1 MPa. First, one observes that our new model for the actin bundle is more rigid than the model in You et al. (2001). The hoop strains are roughly a factor of 3 smaller for the same loading. Second, one notes that there is no observable difference between the predictions of the string model, EI=0, of the transverse element as in You et al. (2001) and the predictions of the 'elastica' model for EI=700 pN·nm^2, for a tissue loading σ of 1 MPa. However, there is a substantial effect when EI is one order of magnitude larger.

Figure **5-6** shows the hoop strains of the osteocyte process as a function of loading frequency with tissue loading as a parameter. In this figure, we also model the transverse element as an inextensible string, as in You et al. (2001), since the flexural rigidity EI has a negligible effect on the hoop strains for loadings > 1 MPa (50 μ strain), as shown in Fig. **5-5**. One observes that a tissue loading > 20 MPa (a tissue strain of 1000 μ strain) will stimulate a hoop strain of more than 0.5% for all loading

frequencies > 1 Hz. Experiments show this is the minimum dynamic substrate strain required to stimulate a cellular response in cultured bone cells (Burger and Veldhuijzen 1993; Smalt et al. 1997; You et al. 2000). One of the most interesting predictions of this new theory is shown in Fig. **5-7**. One observes that tissue strains can be amplified by 10 to 100 fold or more in the physiological loading range (1 to 20 H*z*) and that, in contrast to the earlier theory in You et al. (2001), there is a maximum in this amplification curve at very low loading when the finite flexural rigidity of the tethering elements is considered. As noted in You et al. (2001) the amplification ratio $\varepsilon_t/\varepsilon_c$ increases as the both loading frequency increases and as the whole tissue strain decreases for tissue strains > 5 μ strains (loads > 0.1 MPa).

5.5 Discussion

We have constructed a model for the central filament bundle based on the hexagonal organization of actin filaments crosslinked by fimbrin (Volkmann, et al. 2001). The model is consistent with the central filament bundle organization observed for stereocilia in the ear (DeRosier, et al. 1980) and microvilli in the intestine (Matsudaira and Burgess 1982; Weinbaum, et al. 2001). You et al. (2004) found that there is a 25 nm annular space between the central filament bundle and the osteocyte process membrane. The structural similarity between the different cell protuberances suggests that brush border myosin I or cross-filaments of equivalent function attach the core actin bundle to the osteocyte process membrane in this annular space. Furthermore, the structural periodicity in hexagonally packed microvilli and stereocilia suggests that the cross-filaments are spirally arranged with a *37.5 nm*

spacing and the transverse elements, which attach the osteocyte process membrane to the canalicular wall, are arranged in a similar manner. Three features of this model make the osteocyte process more rigid than the model proposed by You et al. (2001). First, the inner actin filaments of the central bundle experience no deflection due to the hexagonal symmetry of the spiraling fimbrin crosslinks, which was not realized in earlier studies. Hence, there is no cumulative displacement of radially symmetric alternately loaded actin filaments. Second, the periodic spacing between the fimbrin crosslinks was smaller, 37.5 nm in Fig. **5-1(b)** instead of 50 nm as assumed by You et al. (2001). Third, actin filaments in the outer ring in You et al. (2001) had a uniformly distributed load other than a point load T_n as in the present model. The probable existence of the double helical spiral of cross-filaments shown in Fig. **5-1(d)** was not realized previously (You et al. 2001). Combining these three effects, one finds that the hoop strains in the osteocyte process would be a factor of 3 smaller than those predicted by You and co-workers (2001). However, the hoop strain is still quite large and is sufficient to stimulate cellular responses, as shown in Fig. **5-6**, for loads > 20 MPa at 1 Hz (tissue strain > 1000 μ strain) and for loads as small as 5 MPa at 20 Hz (tissue strains 250 μ strain). The latter load corresponds to a cellular level strain of 0.5 percent, see Fig. **5-6**.

Fig. **5-2** shows that the hydrodynamic loading produces a deflection of the transverse element while the tensile force and the flexural rigidity inhibit the deflection. Hence, the finite bending rigidity EI should play a role in the strain amplification model, at least for whole tissue strains < 50 μ strain (tissue loadings < 0.1 MPa), see Fig. **5-7**. Fig. **5-5** shows that the hoop strain decreases as EI increases.

However, the transverse element behaves like a string for tissue loading > 1 MPa for EI = 700 pN. Nm^2. Thus, finite flexural rigidity only inhibits the strain amplification at very small tissue loading. This result has important implications since it might explain why cellular level signaling mechanisms are not constantly excited by the numerous low amplitude loads observed in bone (Fritton et al. 2000).

Although the actual mechanism by which bone cells sense mechanical loading is not known for sure, a growing body of theoretical and experimental studies (Knothe Tate 2001; Reich and Frangos 1991; Weinbaum et al. 1994; You et al. 2000; You et al. 2001) suggest that it is related to the fluid flow in the lacunar-canalicular porosity. Reich and Frangos (Reich and Frangos 1991) first demonstrated in culture that osteoblasts can sense fluid shear stress and elicit biochemical responses at shear levels comparable to endothelial cells. Subsequently, Weinbaum et al. (1994) developed a theoretical model to predict the fluid shear stress levels that the cell process membrane would experience due to physiological loading and showed quite surprisingly that this was essentially the same as endothelial cells in human capillaries. Thereafter, numerous cell culture studies with osteoblasts and osteocytes demonstrated intracellular fluid shear responses to steady, pulsatile and oscillatory shear (Klein-Nulend et al. 1997; You et al. 2000). However, the fluid shear hypothesis was then questioned in Weinbaum et al. (2001) on several grounds. First, the theoretical model by You et al. (2001) predicted that the fluid drag on the tethering fibers per unit process length was approximately 20 times > than the fluid shear stress per unit cell process length suggesting that fluid drag induced by mechanical loading was the dominant mechanism. Second, the theoretically predicted effective Young's modulus

E_{eff} of the actin filament bundle in the cell process using earlier assumed model parameters (You, et al. 2001) was roughly 200 times > than that measured in the cell body (Shin and Athanasiou 1999). The present analysis predicts that E_{eff} of this central bundle is roughly three times that in You's work (2001). This suggests that the fluid shear responses that were being measured experimentally in cell cultures in fluid flow chambers (Reich and Frangos 1991; You et al. 2000) were being elicited from the cell body rather than from the much more rigid, tightly organized cell processes, which are widely viewed as the sensing elements of the osteocyte.

The experiments of You et al. (2000) are particularly revealing since they established a threshold response to elicit the release of Ca^{2+} when bone cells were grown on stretchable substrates and also examined the fluid shear response using several different cell lines including ostoblastic and osteocytic (MLO-Y4) cells. Previously, other investigators had examined very small cellular level deformations by bending rigid glass substrates but were unable to separate out the effects due fluid shear and substrate deformation. Owan et al. (1997) tried to overcome this difficulty by using slides of different thickness and concluded that fluid shear was the dominant mechanism since osteopontin expression was enhanced by fluid shear, whereas there was no response for strain levels as high as 8 percent. Osteopontin is an important noncollagenous protein in bone matrix that is associated with bone remolding. In contrast, Ca^{2+} is an early response second messenger associated with numerous signaling pathways, and , thus, a better indicator of the immediate mechanical response of the cells. The experiments on the MLO-Y4 cells in, cells which have extended cell processes, showed significant increase in cytosolic Ca^{2+} when substrate

strains were increased from 0.1 to 1.0 percent (You et al. 2000). This observation was similar to the observation of Smalt et al. (1997), who found no increase in NO or PGE_2 production for cellular strains up to 0.5 percent. The model herein predicts that a threshold cellular level strain of 0.5 percent can be achieved by a tissue loading of 20 MPa (tissue level strain of 1000 μ strain) at ≥ 1 Hz or a tissue loading of 5 MPa at ≥ 10 Hz, see Fig. **5-6**. It is of great interest that this prediction is consistent with the observation in Rubin and Lanyon (1985) that dynamic strains ≥ 1000 μ strain at 1 Hz induced substantial periosteal and endosteal bone formation while strains < 1000 μ strain at this same frequency led to bone loss. This suggests that bone tissue is not constantly excited by the plethora of small strains to which it is subject on a daily basis (Fritton et al. 2000), and that bone cells respond to only larger strains that were shown in Fritton et al. (2000) to occur only few times a day. This is supported by the observation in Rubin and Lanyon (1985) who reported that substantial bone formation would occur in the ulnas of turkeys in which only 100 load cycles 1 Hz daily for 8 weeks was required to maintain bone mass provided the peak strains were > 1000 μ strain. A second related behavior for very small strains is observed in Fig. **5-7**. The finite flexural rigidity of the tethering element leads to a strong attenuation of the amplification mechanism described herein for tissue level strains < 5 μ strain.

The important role that the pericellular matrix plays in the transmission of fluid shear stress to the actin cytoskeleton, and the dichotomy in response of the cell body and cell processes, is suggested by the recent experiments of Reilly et al. (2003). These investigators exposed MLO-Y4 cells to oscillating fluid shear in which this extracellular matrix was either intact or degraded by hyaluronidase treatment. There

was no effect of the glycocalyx degradation on the 2-5 fold increase in the intracellular calcium response, but the 4-fold increase in the PGE_2 response was eliminated. This loss of PGE_2 response was not observed for osteoblastic cells, which do not have cell processes, suggesting that cell processes are associated with the PGE_2 response. In contrast, calcium signaling is associated with hydrodynamic shear forces acting on the much more compliant cell body, and this effect should be independent of the presence or absence of a thin pericellular matrix layer. Jiang and Cherian (2003) have recently shown that hemichannels formed by connexin 43 in the cell processes are upregulated by mechanical strain. These hemichannels allow for the release of PGE_2 into the external environment where it functions in an autocrine manner to regulate gap junction communication.

We emphasize that the present model provides a lower bound on the maximum strain that the central actin filament bundle will experience. First, the fimbrin cross-links are treated as inextensible because it was assumed that the axial strains on the fimbrin crossbridges were small compared to the bending strain on the actin filaments. Second, the positioning of the cross-filament attachments in Fig. **5-1b** has been chosen to minimize the maximum deflection of the filaments in the outer ring of the actin filament bundle. One can only speculate about the mechanism via which hoop strains on the central actin filament bundle cause cytosolic Ca^{2+} to increase. This could be through stretch activated channels in the membrane of the cell process or an axial tension that is transmitted to the cell body due to an axial shortening of the actin filaments in the outer ring of the bundle that arise from their undulating periodic deformation.

Whereas the release of Ca^{2+} and a variety of second messengers observed *in vitro* can very likely be attributed to a shear response acting on the cell body, rather than the much stiffer cell processes (Reich and Frangos 1991; You et al. 2000), these experiments provide little information about the fluid shear stress response *in vivo,* where the shear stress on the cell body and the cell processes can differ greatly due to lacunar-canalicular geometry. Cell processes are exposed to a level of fluid shear stress *in vivo* that is comparable to endothelial shear stresses in capillaries (Weinbaum et al. 1994) because the fluid annulus surrounding the process is so narrow, 78 nm on average for adult mice (You et al. 2004). A pericellular matrix is also observed surrounding the cell body in lacunae, but the thickness of this layer is typically one μm and highly variable. Such distances argue against a tethering of the cell body to the lacunar wall as occurs in the canaliculi. From flow continuity arguments the fluid velocity in the pericellular space of the lacunae will be at least one order of magnitude smaller than in the canaliculi and, thus, the shear stress on the cell body will be at least an order of magnitude smaller than those predicted for the cell processes. These qualitative estimates suggest that the cell body *in vivo* is not involved in mechanosensation, even though its effective Young's modulus is much smaller than the cell process. The more likely hypothesis is that the excitation mechanism is not fluid shear stress acting on the cell process membrane, but rather, the unique strain amplification hypothesis that results from the interaction of the pericellular matrix and the cell process cytoskeleton.

5.6 Footnotes

This chapter is reprinted with permission from Han, Y., Cowin, S. C., Schaffler, M. B. and Weinbaum, S. (2004) "Mechanotransduction and strain amplification in osteocyte cell processes." *Proc. Natl. Acad. Sci. USA* **101**(47): 16689-16694.

Chapter 6 Chemical Regulation of Hemichannels and Purinergic $P2X_7$ Receptors

6.1 Introduction

A fundamental mechanism in the transduction process in bone is the opening of a channel whose identification and localization is not known, but has the unusual property of being permeable to molecules as large as ATP and PGE_2 (Cheng et al. 2001; Cherian et al. 2003; Genetos, 2005). There are several candidates for such a channel, including nonjunctional gap junction channels or "hemichannels" and purinergic P2X receptors, but their involvement in this process is not rigorously demonstrated.

Prostaglandin (PG) is an anabolic agent that has been shown to increase bone mass in animals (Jee et al., 1985; Keller et al., 1993; Baylink et al., 1995; Harada et al., 1995). Forwood (1996) has shown that its presence is required in new bone formation in vivo under mechanical loading. One puzzling finding is that mice lacking genes for COX-2, an enzyme required for PG synthesis, do not have bone developmental defects (Dinchuk et al. 1995). This could be due to the absence of mechanical loading during early bone formation. In culture studies Flanagan and Chambers (1992) and Nagata et al. (1994) have demonstrated that PGE_2 is required for bone nodule formation. These results are especially significant in view of the fact that many investigators have shown that osteoblast and osteocytes release PGE_2 in response to fluid shear stress (FSS) (Reich and Frangos 1991; Klein-Nulend et al. 1995; Cheng et al. 2001; Reilly et al. 2003). The paper by Reilly et al. provides an additional important insight since it

provides a clue as to how the FSS might be communicated to the cytoskeleton and the role that polarization in the elastic properties between the cell body and cell processes might play. These authors showed that hyaluronidase treatment to remove the pericellular matrix on MLO-Y4 cells could entirely abolish a four fold increase in PGE_2 release in response to FSS. In marked contrast, hyaluronidase treatment had no effect on the increase in intracellular Ca^{2+} in response to FSS. This divergent behavior could be explained if the Ca^{2+} response was due to the release of intracellular Ca^{2+} from the endoplasmic reticulum in the cell body whereas the PGE_2 release was originating in the cell processes. In terms of the model in Han et al. (2004) the drag on the pericellular matrix surrounding the thin cell processes is communicated as a strain on the central actin filament bundle in the processes, whereas the deformation of the cell body is independent of the presence of this matrix since it is due to pressure forces arising from the flow over the much larger and softer cell body.

Jiang and coworkers have performed a series of studies (Cheng et al. 2001; Cherian et al. 2003; Jiang and Cherian 2003; Cherian et al. 2005) to try and establish the signaling pathway through which PGE_2 performs its autocrine regulation. These researchers first showed that conditioned medium obtained from fluid flow-treated MLO-Y4 cells increased the abundance of Cx43 and produced a response that was identical to MLO-Y4 cells directly exposed to FSS where there was PGE_2 release and increased COX-2 expression. The response could be substantially abrogated by removing PGE_2 from the external medium. In Cherian et al. (2003) this group showed that the regulation of gap junctions occurred through an EP2 receptor that activated cAMP-dependent protein kinase A (PKA). Application of PGE_2 directly or from the

conditioned medium of FSS treated cells also led to the increased expression of the EP2 receptor. Jiang and Cherian (2003) proposed that the pathway for PGE_2 release is Cx43 hemichannels but the blockers used, antisense Cx43 and 18-βGA, were not specific for this gap junction protein. In Cherian et al. (2005) they attempted to strengthen the case for Cx43 using the blocker carbenoxolone and inhibitors for other channels, the purinergic receptor $P2X_7$ and the PG transporter PGT. Since FSS appears to direct Cx43 hemichannels to both the membranes of the cell processes and the cell body one is unable to establish the localization of the PGE_2 release or its relationship to the polarization of the cell. The other issue that needs to be explained is how Cx43 is opened under physiological conditions.

The foregoing difficulties have led the Donahue group to explore an alternative hypothesis for the activation of gap junction hemichannels which was just reported in The 7th Bone Fluid Flow Workshop and the PhD dissertation of D. Genetos (2005). This group observed significant PGE_2 release in Cx43 deficient MLO-Y4 cells treated with exogenous ATP, suggesting that PGE_2 release does not occur directly through open hemichannels. Instead they proposed that the activation of the hemichannels occurs through a mechanism involving protein kinase C, which then promoted ATP release. Removal of Cx43 using siRNA strategies greatly reduced ATP release, which was interpreted as due to hemichannel activation (although the caveat stands that $P2X_7$ expression was not evaluated following Cx43 siRNA application). In this scenario FSS on MLO-Y4 cells first produces ATP release, which then functions in an autocrine fashion to promote PGE_2 release downstream of P2 receptor activation by the ATP.

In this chapter I aim to characterize experimentally the activities of the P2X receptor on the cellular membrane.

6.2. Materials and Methods

6.2.1. Cell Cultures

Osteocyte-like MLO-Y4 cells (obtained from Dr. Lynda F. Bonewald, Univ. TX Health Science Center) were cultured in α-MEM that contained 1% penicillin-streptomycin, 2.5% FBS, and 2.5% calf serum (GIBCO-BRL) at 37°C with 95% O_2-5% CO_2. The cells were plated at low density around 1000 cells/cm^2, and the experiments were performed after two days' culture to allow enough time for the growth of cell processes.

6.2.2. Dye Uptake Assay

YoPro was used as a tracer to detect the activities of hemichannels and P2X receptors on the membrane of MLO-Y4 cells. This dye shows fluorescence only after permeating into cells and interacting with nucleic acids. MLO-Y4 cells in low densities were first treated with agonists/antagonists to P2X receptors in serum free media for 20 minutes. Then, the cells were bathed with Ca^{2+} and Mg^{2+} free PBS with the presence of the same agonist or antagonist and YoPro (5 μM) for another 10 minutes. The cells were washed with regular PBS and observed with a fluorescence microscope. Dye uptake was shown as a percentage of YoPro positive cells after counting the fluorescent images and the corresponding phase images.

6.3. Results and Discussions

Figures 6-1(a-d) show YoPro uptakes by MLO-Y4 cells after being bathed for 10 minutes in regular PBS (rPBS), No Ca/Mg PBS (Ca^{2+} and Mg^{2+} free PBS), no Ca/Mg PBS with 1 mM ATP, and no Ca/Mg PBS with 1 mM ATP and 10 μM KN-62 (1-[N,O-Bis(5-isoquinolinesulfonyl)-N-methyl-L-tyrosyl]-4-phenylpiperazine, an antagonist to $P2X_7$ receptors), respectively. The cells bathed in rPBS are not fluorescence positive in Fig. **6-1(a)**. This indicates that both hemichannels and $P2X_7$ receptors putatively present on the cellular membrane are not open in static media with physiological ion concentrations. This is consistent with the observations in Cherian and Jiang (2003) and Genetos (2005). However, fluorescence was observed in some experiments with rPBS since dead cells have leaky membranes. It is well accepted that divalent cation Ca^{2+} and Mg^{2+} deficient media activates hemichannels and enhances dye uptake by cells. However, figure **6-1(b)** shows that only a small percentage of cells are positive with fluorescence when incubated with Ca^{2+} and Mg^{2+} deficient PBS, even though this incubation enhances dye uptake compared to regular PBS in Fig. **6-1(a)**. In contrast, most of cells observed Fig. **6-1(c)** take up fluorescence when 1 mM ATP, an agonist to $P2X_7$ receptors, is added to the incubating divalent free PBS. More interestingly, the enhancement of dye uptake in Fig. **6-1(c)** can be negated by the addition of KN-62, one of widely-used antagonists to $P2X_7$ receptors. This suggests the involvement of $P2X_7$ receptors in the dye uptake of the cells treated with ATP. Note that Genetos (2005) proposed that PGE_2 release in response to fluid shear stress is through $P2X_7$ receptors subsequent to ATP activation while Cherian and Jiang (2003) proposed it is through hemichannels.

To further characterize the involvement of hemichannels and $P2X_7$ receptors in the dye uptake by MLO-Y4 cells we quantified the dye uptake of the cells incubated with different media. These results are shown in Fig. **6-2**. Note that control with Dimethyl Sulfoxide (DMSO) was also performed since KN-62 and Brilliant Blue G (BBG) were dissolved in it. In regular PBS (rPBS) the cells positive for YoPro are about 2%, while in divalent cation free PBS (No Ca/Mg PBS) about 15% of the cells exhibit dye uptake. When exposed to DMSO in divalent ion free PBS, dye influx is slightly reduced compared to the situation with No Ca/Mg PBS. Addition of 1 mM ATP increases dye uptake so enormously that about 60% of the cells are positive with fluorescence. Note, however, that the concentration of ATP is much higher than the physiological concentration to compensate for its degradation and amplify its effect on cells. The cells incubated with KN-62 and Brilliant Blue G (BBG), both moderately specific blockers of P2X7 receptors with no effect on gap junctions, show dose-dependent inhibition of dye influx induced by 1 mM ATP. Both BBG and KN-62 at 10 μM reduce the dye uptake induced by 1 mM ATP to less than 3% of the cells, which is comparable to the dye uptake with rPBS. These observations indicate that $P2X_7$ receptors are widely present on MLO-Y4 cells and contribute significantly to the cellular dye uptake at least in static shear-free conditions. The agonists and antagonists used in Fig. **6-2** will be used to examine the effect of fluid shear in future experiments.

6.4 Acknowledgements

All the experiments in this chapter were performed jointly with Dr. Mia M. Thi in Dr. David C. Spray's laboratory in the Department of Neuroscience at Albert Einstein College of Medicine.

Chapter 7 Conclusion

Both endothelial cells and bone cells are at least partly coated with extracellular matrices, which interact with the fluid around the cells and transmit hydrodynamic forces to the intracellular cytoskeleton to initiate cellular signaling cascades, although the mechanisms involved are different. The core proteins in the endothelial glycocalyx are relatively rigid and do not deform significantly at physiological shearing stresses and, thus, convert fluid drag at their tips into bending moments at their roots much like the bending moment reaction at the fixed end of a cantilever beam due to loading at its free end. In contrast, the transverse elements in the pericellular matrix surrounding osteocytic processes are highly flexible when exposed to a physiological flow that produces a uniform fluid drag and, then, convert this fluid drag into axial tension along the transverse elements. This produces an amplified hoop tension on the osteocytic processes much like the horizontal tension reaction along a hanging chain which takes the shape of a catenary due to its uniformly distributed weight.

In chapters 2 and 3 I used large deformation theory to estimate the flexural rigidity of the core proteins in the endothelial glycocalyx and modeled the deformation of the core proteins due to red blood cell motion and arrest. Squire et al. (2001) observed the 3D quasi periodic structure of the endothelial glycocalyx for the first time. Based on this structure Weinbaum et al. (2003) proposed that the core proteins of the endothelial glycocalyx must be relatively rigid to maintain the periodic structure and further proposed that they function as a mechanotransducer. In chapter 2 I estimated that the flexural rigidity of a single core protein fiber is 490 $pN \cdot nm^2$. This

value is 70% the prediction in Weinbaum et al. (2003) and 3% the measured flexural rigidity of an F-actin filament. Thus, the core proteins are sufficiently rigid to serve as a molecular filter for plasma proteins and can function as an exquisitely designed transducer of fluid shear stresses. However, this flexural rigidity is inadequate to prevent the buckling of these protein structures during the intermittent motion of RBCs, as shown in chapter 3. In this chapter I predicted that the deflection of the core proteins increases from 1 to 8 nm as the red blood cell velocity increases from 20 to 210 μm/s. The magnitude of the tip deflection at 210 μm/s is about three quarters of the prediction in Weinbaum (2003) for a shear stress of 10 dyn/cm^2. If *Kp* is constant the intracellular pressure of the arrested RBCs required to complete the compression of the endothelial glycocalyx in 0.5 s is 2,420 dyn/cm^2. However, this compaction time is extended 50 fold if *Kp* varies with the compression of the endothelial glycocalyx.

In chapter 4 I developed a generalized mathematical model for the dynamic response of the endothelial glycocalyx in blood vessels, the microvilli in proximal tubules, and the cilia in the cortical collecting duct when oscillatory shear is applied at the edge of these surface structures. When the apical surface layers (brush border, endothelial glycocalyx or cilia layer) experience steady shear, the velocity field depends only on the Brinkman parameter α. Fluid motion induced by the applied shear penetrates all the way to the apical membrane for $\alpha=1$, and for $\alpha>10$ a tip interaction or boundary layer develops at the edge of the surface layers. When the apical surface experiences oscillatory shear, the fluid motion and the dynamic deflection depend on two key parameters, the Brinkman parameter α and the dimensionless frequency parameter ω_r. For $\alpha\leq1$, $\omega_c=10$ rad/s at 1 Hz (cilia), the fluid velocity and the deflection

of the structural elements are in phase with the applied shear stress, their amplitudes are the same as for steady flow, and the relative velocity between fluid and structural element is close to the fluid velocity. However, for α=100, $\omega_c \geq 100$ rad/s at 1 Hz (glycocalyx and microvilli), the fluid velocity is out of phase with the shear, and the relative velocity between fluid and structural elements vanishes except for the tip interaction layer at $x=L$. Since all of these surface structures are proposed to function as mechanotransducers, the resultant bending moment at their roots is of extreme significance. For $\omega_r<1$, the amplitude of the resultant bending moment is not attenuated compared to the corresponding bending moment in steady shear. For $\alpha \geq 10$, the normalized bending moment becomes independent of α and is attenuated rapidly as ω_r increases for $\omega_r \geq 1$.

In chapter 5 I improved and refined the strain amplification model proposed by You et al. (2001) to resolve a long unresolved mystery in bone mechanotransduction, namely that physiological whole tissue strains are not sufficient to excite osteocytes in bone. I first developed a three-dimensional model for the osteocyte process with a 19 element actin filament bundle whose organization was modeled after the fimbrin cross-linked hexagonal structure observed in stereocilia (DeRosier, Tilney and Egelman 1980) and microvilli (Volkmann et al. 2001). To our knowledge this is the first attempt to analyze the force distribution in hexagonally packed actin filament bundles with helically arranged fimbrin crossbridges. The new model predicts a cell process that is 3 times stiffer than You et al. (2001), but hoop strains > 0.5 percent for tissue level strains > 1000 μ strain at 1 Hz and > 250 μ strain at frequencies > 10 Hz. These results can be used to relate the threshold strain (0.5 percent) for osteocytic

excitation experimentally observed in You et al (2000) *in vitro* to the whole tissue threshold strain (1000 μ strain at 1 Hz) for bone remolding observed in Rubin and Lanyon (1985) *in vivo*. In contrast to the earlier theory in You et al. (2001), there is a maximum in the amplification ratio between the cellular strain and the whole tissue strain at very low loading when the finite flexural rigidity of the tethering elements is considered. I also proposed that the present theory for cellular level strain amplification provides a more likely hypothesis for the excitation of osteocytes than the fluid shear hypothesis previously proposed in Weinbaum et al. (1994).

In chapter 7 preliminary studies were performed to determine the extent to which specific $P2X_7$ receptor antagonists inhibit dye uptake by MLO-Y4 cells under static no-flow conditions. The results show that KN-62 and BBG, antagonists to $P2X_7$ receptors, dose-dependently inhibit MLO-Y4 cells' dye uptake due to the activation of $P2X_7$ receptors by ATP. Both KN-62 and BBG at 10 μM negate the dye uptake enhancement by 1 mM ATP. These studies strongly indicate that a pathway other than via hemichannels, likely via the $P2X_7$ receptors, participates in dye uptake under stationary, no-flow conditions.

The theoretical models in Chapters 2-4 predict the flexural rigidity of the core proteins in the EG and the deformation of the core proteins when interacting with RBCs or undergoing steady or oscillatory fluid shear. These models assume that the endothelial glycocalyx has a quasi periodic 3D structure observed in Squire et al. (2001) for frog microvessels. Furthermore, it is not clear what the bead-like spherical scattering centers depicted in Fig. **1-1** correspond to, aggregated GAGs on adhered proteins. The estimation that the core proteins have flexural rigidity of 490 $pN{\cdot}nm^2$

supports the hypothesis in Weinbaum (2003) that the EG functions as a mechanotransducer. Also it was experimentally shown that the release of NO by ECs (Florian et al. 2003) and the reorganization of the actin cytoskeleton and associated molecules (Thi et al. 2004) depend on the presence of the EG. However, it was not experimentally shown how the deformation of the EG is used to trigger subsequent cellular signaling response. Thus, it is of interest to (1) characterize the 3D structure of the EG in mammals and identify its structural components, (2) measure the mechanical properties of the endothelial glycocalyx, and (3) determine the signaling pathways that relate the deformation of the EG to the release of NO and the reorganization of the dense peripheral actin bands.

The theoretical modeling of bone mechanotransduction in Chapter 5 raises two fundamental paradoxes: 1) How can the cell processes function as the sensor organelle if the actin filament bundle in the cell processes is so much stiffer than the actin cytoskeleton in the cell body; and 2) how can intracellular biochemical signaling, e.g. mobilization of intracellular Ca^{2+} and release of ATP and PGE_2, be initiated in the cell process when most of the cell's biochemical machinery is located in the cell body. A fundamental mechanism in the transduction process is the opening of a channel whose identification and localization is not known, but has the unusual property of being permeable to molecules as large as ATP and PGE_2. Previous studies (Thi et al. 2003; Cherian et al., 2003) have indicated that fluid shear stress acting on osteocyte-like MLO-Y4 cells results in the disruption of gap junctions, a redistribution of membrane proteins, including Cx43, and the release of PGE_2, thereby establishing an autocrine response mediated by a PGE_2 receptor. Thus, it is of significance to (1) characterize

the 3D structure of the cytoskeleton inside the osteocytic processes, (2) measure and compare the mechanical properties of osteocytic processes and bodies, and (3) identify pathways for PGE_2 and ATP release.

In summary, I have studied the roles of extracellular matrices in mechanosensing in endothelial cells and osteocytes. These studies show that cytoskeleton-associated extracellular matrices on these cells have suitable structures and properties to amplify the physiological loading and induce strains on the intracellular actin cytoskeleton. In turn, these strains are hypothesized to trigger subsequent cellular signaling responses.

TABLES

Table 3-I Compression of the ESL due to RBC arrest.

t (s)	L_f/L_{f0}	t (s)	L_f/L_{f0}
0	1	0.28	0.55
0.015	0.95	0.36	0.50
0.033	0.90	0.47	0.45
0.053	0.85	0.62	0.40
0.076	0.80	0.86	0.35
0.10	0.75	1.29	0.30
0.14	0.70	2.29	0.25
0.17	0.65	7.03	0.20
0.22	0.60	25.5	0.176

Table 4-I Parameter values for surface structural elements.

	Core Protein	Cilia	Microvilli
Fiber Diameter *d* (nm)	4-12[a]	200[b]	90[c]
Fiber Length *l* (μm)	0.15-0.4[a, d]	2.5-8[b]	1.5-3[c]
Open Gap (nm)	8-16	1.1×10^{4}	62-90
Solid Fraction *c*	0.04-0.33	0.0003	0.23-0.32
Bending Rigidity *EI* (PN·nm^2)	700[e]	1.4×10^{7} [f]	8.4×10^{6} [g]
Fluid Viscosity μ (10^{-3}Pa·s)	1.2	1.0	1.0
Typical Shear Force at Tips (dyn/cm^2)	10-20 (Arterial Side) 2-10 (Venous Side)	0.45	1-5
The Darcy Permeability Kp (nm^2)	3.2-26	3.0×10^{7}	190-480
The Dimensionless Darcy's Parameter α	29-223	0.46-1.46	137-215
Beam Characteristic Frequency ω_c (rad/s)	1.1×10^{4}-8.3×10^{4}	2.0-21	3.4×10^{4}-1.9×10^{5}
ω_r at 1 Hz	7.6×10^{-5}-5.7×10^{-4}	0.30-3.1	3.3×10^{-6}-1.8×10^{-4}

[a] Squire et al. (2001); [b]Evan et al. (1991); [c]Maunsbach et al. (1987); [d]Vink and Duling (1996); [e]Weinbaum et al. (2003); [f]Liu et al. (2003); [g]Guo et al. (2000).

Table 5-I Values of the parameters used in the model.

Parameters for the osteonal hydrodynamic model
B, dimensionless relative compressibility of bone matrix to water, *0.53;*
c, the pore fluid pressure diffusion constant of the Biot theory, *0.13 mm^2/s;*
r_o, radius of the osteon, *100 μm;* r_i, radius of the osteonal lumen, *27 μm;*
Parameters for the canaliculus and cell process
R_1, radius of the canaliculus, *130 nm;*
R_0, radius of the osteocyte process, 52 nm;
K_P, the Darcy's permeability of the matrix between the cell process and the canalicular wall, *10.3 nm^2;*
μ, fluid viscosity, *1cp;*
L_c, length of an individual transverse element, *88 nm;*
EI, bending rigidity of the transverse element, *700 $pN \cdot nm^2$;*
Parameters for the central actin bundle
L_f, length of the periodic fimbrin crossover along actin filament, *37.5 nm;*
EI_a, bending rigidity of actin filaments, *1.5x10^4 $pN \cdot nm^2$*.

FIGURES

(a)

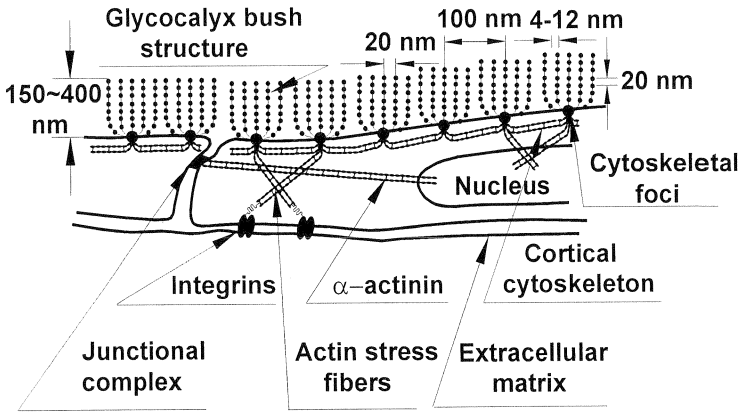

(b)

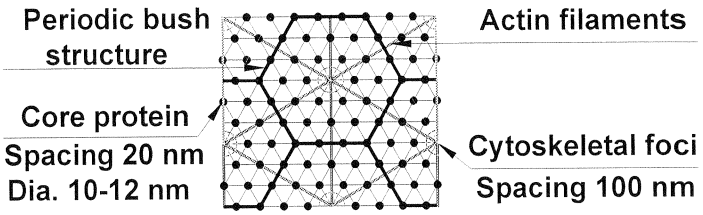

Figure 1-1. Structural model for the endothelial surface layer (ESL) from Squire et al. (2001) and Weinbaum et al. (2003). (a) Sketch of the arrangement of core proteins in the ESL and its anchorage to the underlying cortical cytoskeleton. (b) *En face* view of the structural model showing the hexagonal arrangement of core proteins and cluster foci. (Adapted from Weinbaum et al. (2003))

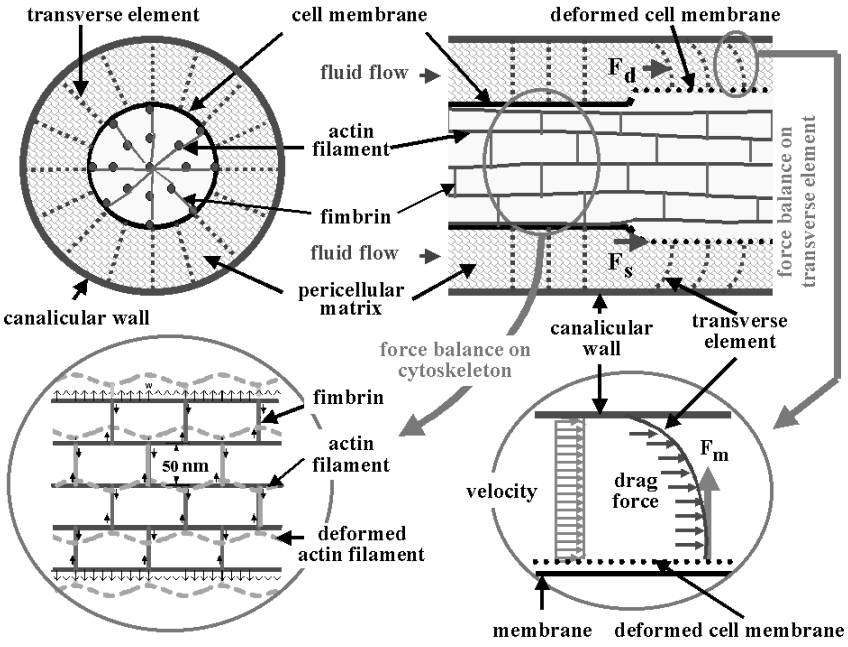

Figure 1-2. Schematic model showing the structure of the pericellular matrix (PM), the internal actin cytoskeleton (IAC) inside the process and the connection between the PM and the IAC. (a) Transverse cross-section of canaliculus showing the fluid annular shape of the region and transverse (radial) pericellular fibers. (b) Longitudinal cross-section before and after the transverse elements are deformed by the flow. (c) The deformation of the actin bundle inside the cell process. The links (fimbrin) between actin filaments are considered to be inextensible. (d) Force balance on a transverse element. (Adapted from You et al. 2001)

(a)

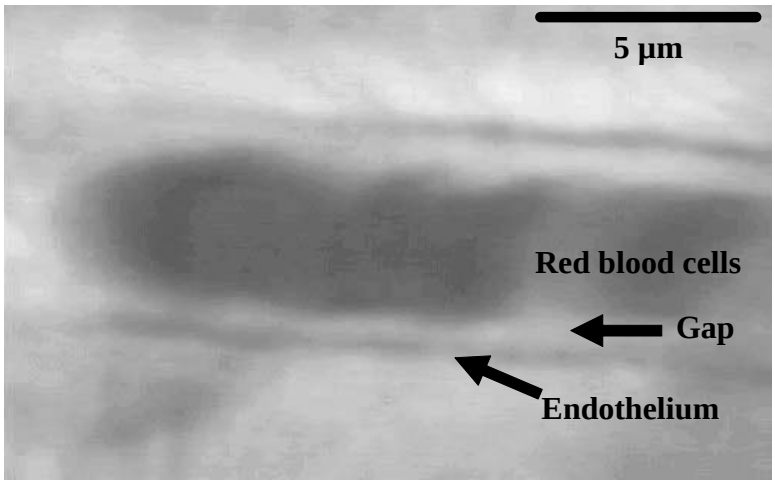

(b)

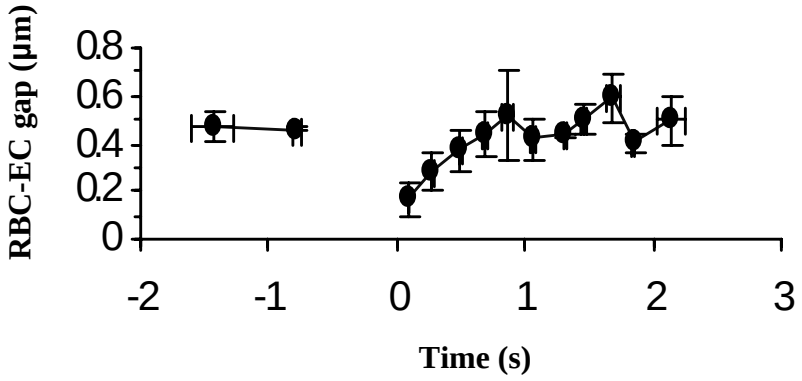

Figure 2-1. Microscopic image of a transilluminated hamster muscle capillary showing the measurement of RBC-EC gaps (a), and RBC-EC gap recovery as a function of time after the passage of a WBC through a capillary with a diameter of 4.4 µm (b).

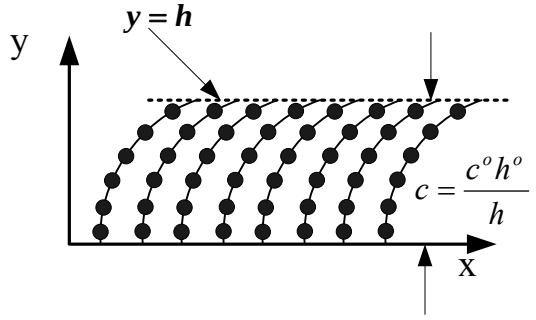

Figure 2-2. Simplified model for the structure of the ESL. The ESL is modeled as a porous medium with an average solid fraction c dependent on the ESL thickness, with scattering centers (black dots) 12 nm diameter located at 20 nm intervals along axes of the core proteins.

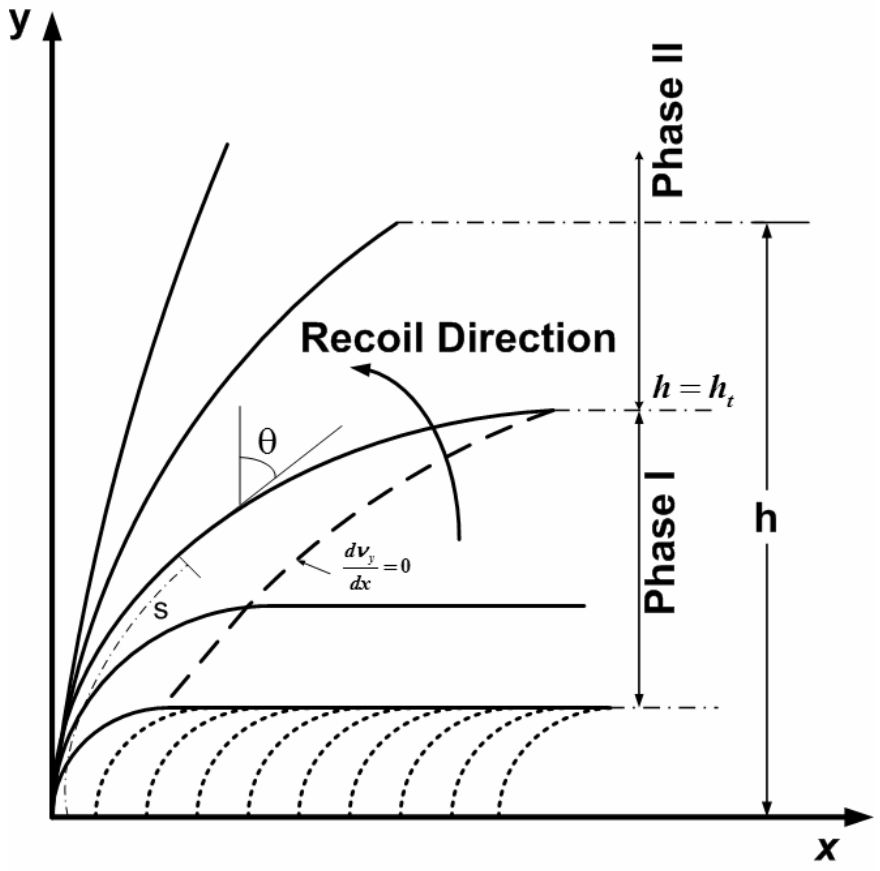

Figure 2-3. Parametric family of shapes for core protein fibers during the ESL recovery. In phase I the tip ends of core protein fibers are matted and in phase II the core protein fibers are no longer matted and have a slope >0 at their ends.

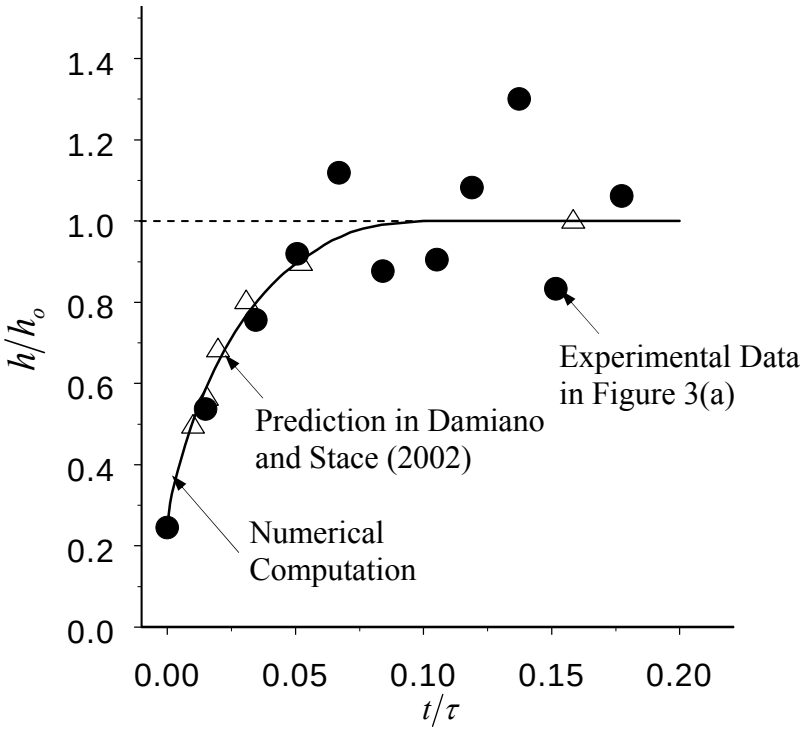

Figure 2-4. Comparison of our model predictions (solid line) and the predictions (open triangle) of figure 2(b) in Damiano and Stace (2002) with the experiment results shown in figure 3(a) (black dots). The ESL thickness is normalized by 400 nm, the undisturbed ESL thickness, and the recovery time is normalized by the dimensional reference time defined by Eq. **2-12** with a value of 11.5 s. The data taken from Damiano and Stace are rescaled by a factor of 46900 and shifted to right by 0.01 since the starting point of their recovery of the ESL is 0.5 its initial thickness.

Figure 2-5

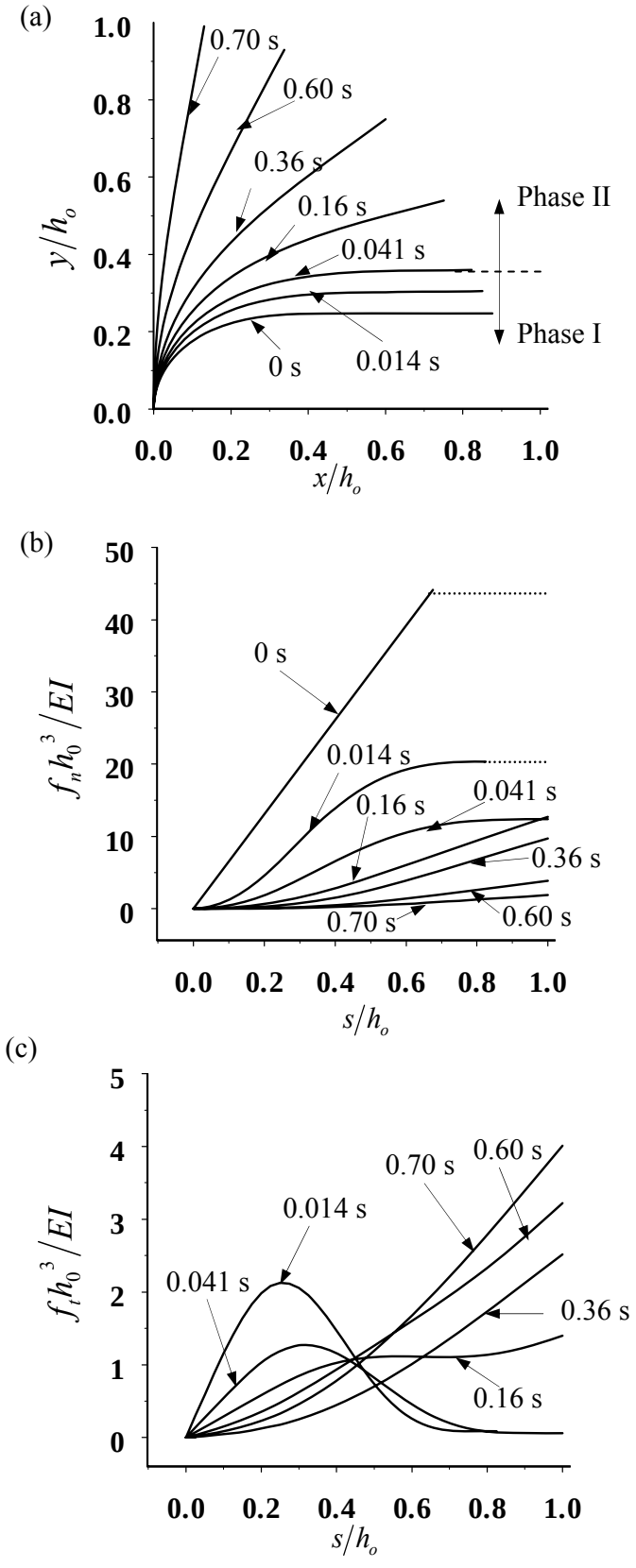
(a)
1.0
0.8
0.6
0.4
0.2
0.0
y/h_o
0.70 s
0.60 s
0.36 s
0.16 s
0.041 s
0 s
0.014 s
Phase II
Phase I
0.0 0.2 0.4 0.6 0.8 1.0
x/h_o
(b)
50
40
30
20
10
0
$f_n h_0^3/EI$
0 s
0.014 s
0.16 s
0.041 s
0.36 s
0.70 s
0.60 s
0.0 0.2 0.4 0.6 0.8 1.0
s/h_o
(c)
5
4
3
2
1
0
$f_t h_0^3/EI$
0.70 s
0.60 s
0.014 s
0.041 s
0.36 s
0.16 s
0.0 0.2 0.4 0.6 0.8 1.0
s/h_o

Figure 2-5. The time dependent change in shape of the core protein fiber (a) and their hydrodynamic loading (b) during ESL restoration after the passage of a WBC. The dotted lines in (b) show the hydrodynamic loading on the flat portion of the core protein fiber, which is balanced by the restoring force of the fibers in the matted layer beneath it.

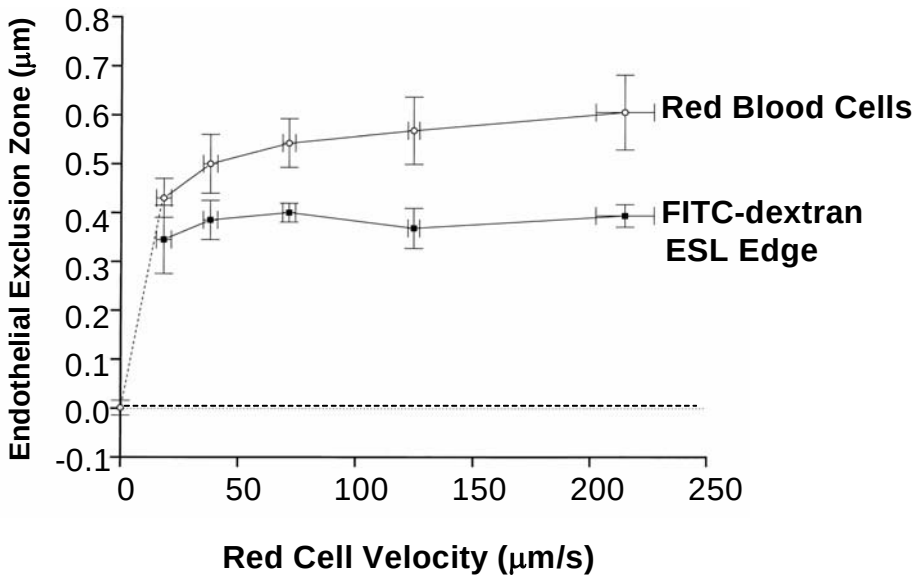

Figure 3-1. The thickness of apparent endothelial exclusion zones for FITC-dextran and RBCs as a function of RBC velocity. (Adapted from Vink and Duling (1996))

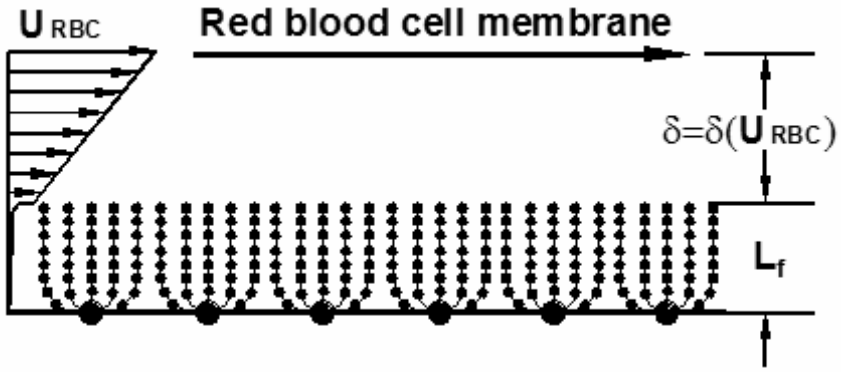

Figure 3-2. Sketch of our model for RBC gliding above ESL. U_{RBC} is the velocity of red blood cells; L_f is the thickness of ESL; δ is the thickness of plasma between RBC and ESL. This thickness is a function of the velocity of RBC, see Fig. **3-1**.

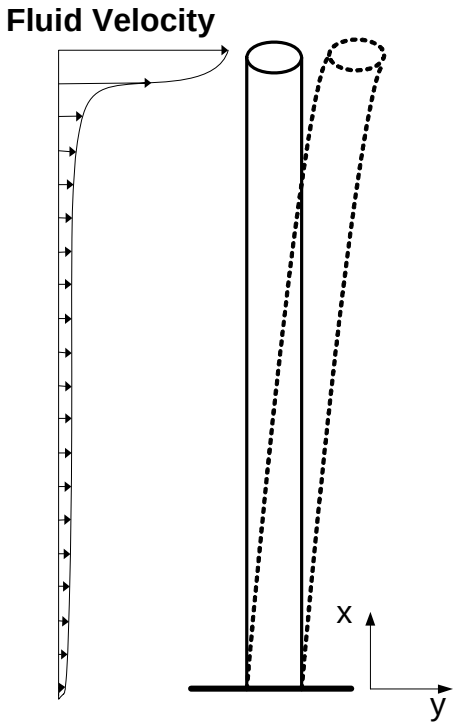

Figure 3-3. Sketch of our model for the core protein fiber as a cantilever beam.

.

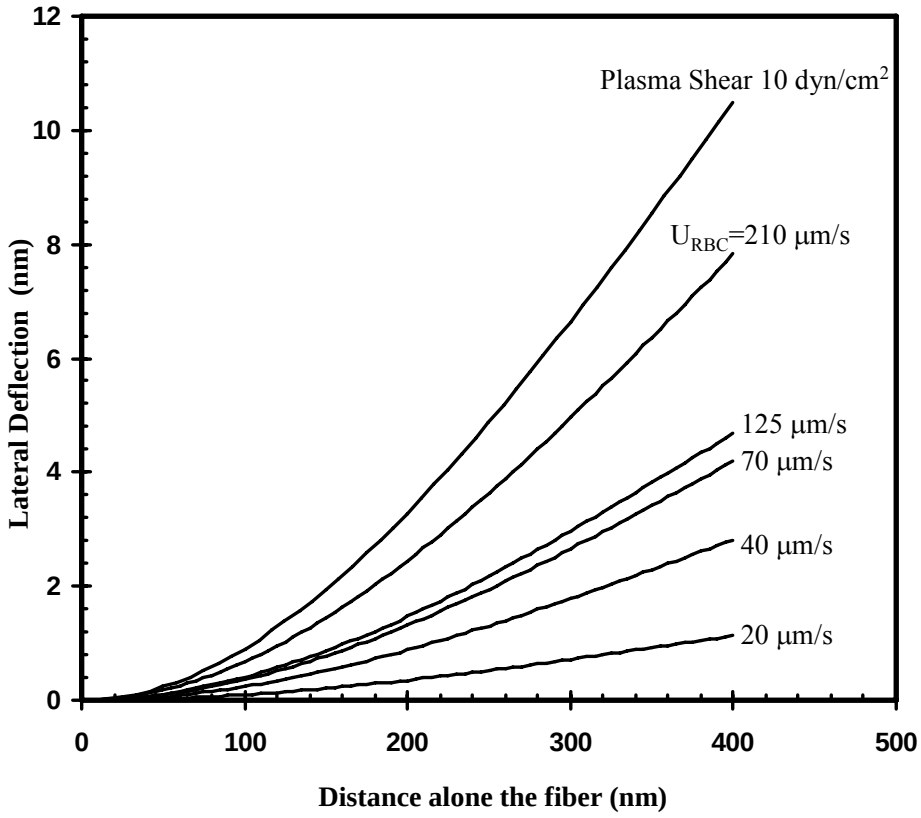

Figure 3-4. Model predictions for lateral deflection of core proteins beneath red cells moving at different velocities, U_{RBC}.

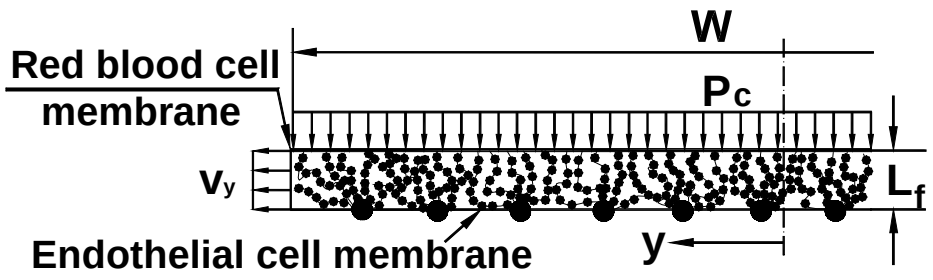

Figure 3-5. Sketch of our model for ESL for RBC arrest. $V_y(y)$ is the local velocity of fluid in the ESL; *W* is the width of red cell; Pc is compression pressure of the red cell membrane on the ESL and L_f is the height of the ESL.

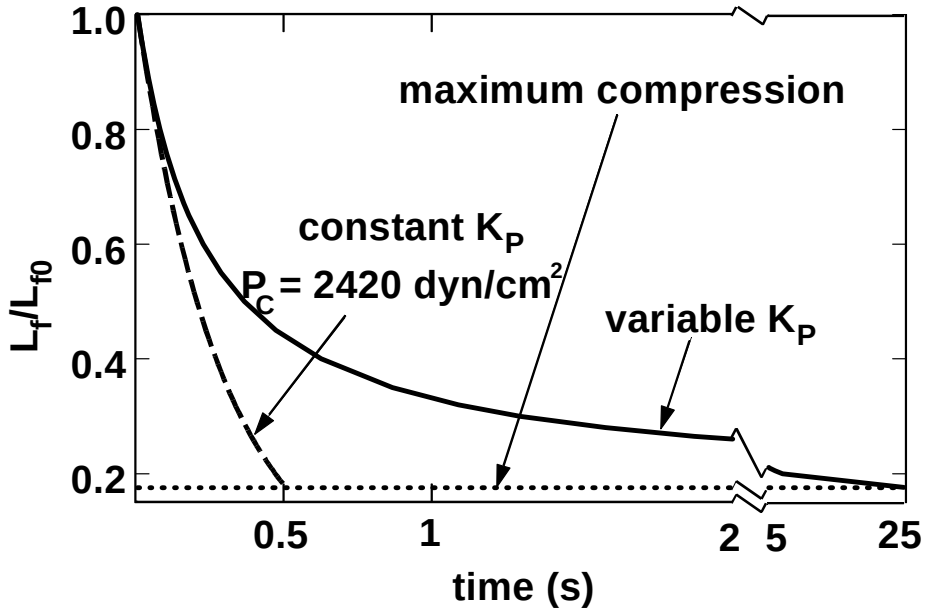

Figure 3-6. Model prediction for time-dependent drainage of fluid from ESL after red cell arrest in a 5-μm-diameter capillary. A cell pressure of 2,420 dyn/cm^2 is required to fully collapse the layer within 0.5 s (H. Vink, private communication) at constant K_P. This time is extended to 25 s if the variation of K_P with compression is considered.

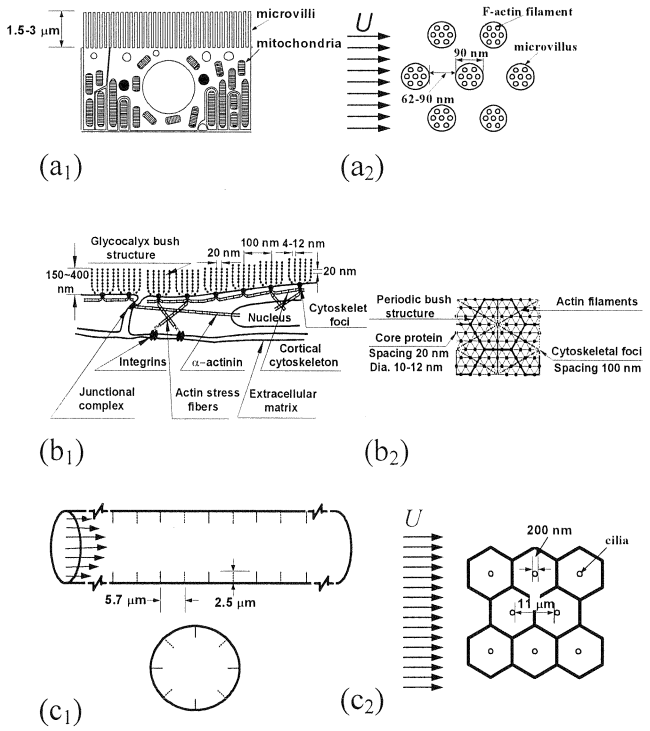

Figure 4-1. Structural diagram for the surface layers. (a_1) Schematic diagram of a proximal tubule epithelial cell with its basic intracellular structures. (a_2) Idealized model for the arrangement of the microvilli and their actin filament organization in kidney proximal tubule cells. (b_1) Sketch of the arrangement of core proteins in the endothelial glycocalyx and its relation to the underlying cortical cytoskeleton based on Squire et al. (2001). (b_2) *En face* view of the idealized mathematical model in Weinbaum et al. (2003) showing the hexagonal arrangement of core proteins and cluster foci and their relationship to cortical cytoskeleton. (c_1) Longitudinal and radial cross sections of kidney CCD showing the arrangement of cilia. The Solid lines and dotted lines denote cilia in different planes. (c_2) *En face* view of idealized model of principal cells with cilia located at the center of each hexagonal cell.

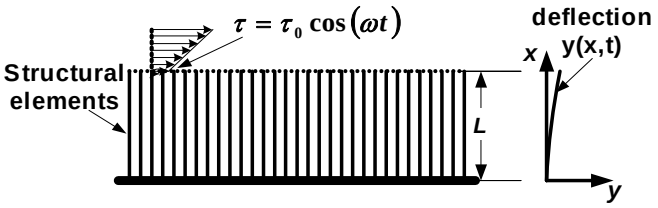

Figure 4-2. Sketch of basic model for shear flow past structural elements at apical surface. The surface layer is modeled as planar geometry of thickness *L*.

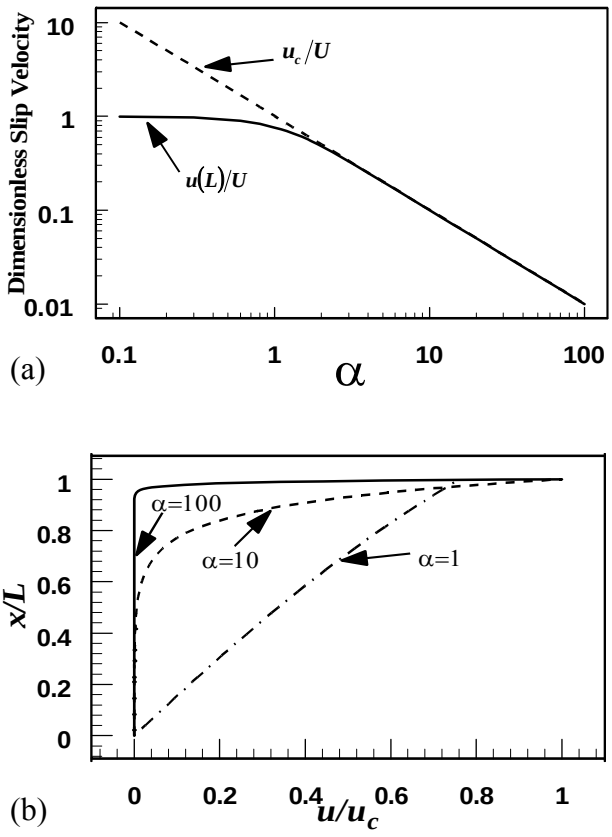

Figure 4-3. Dimensionless fluid velocity and its scale. (a) Dimensionless slip velocity $u(L)/U$ and dimensionless characteristic velocity u_c/U ($U = \tau_0 L/\mu$) as a function of α for steady shear. (b) Dimensionless velocity profile u/u_c along the length of the structural element at different α for steady shear.

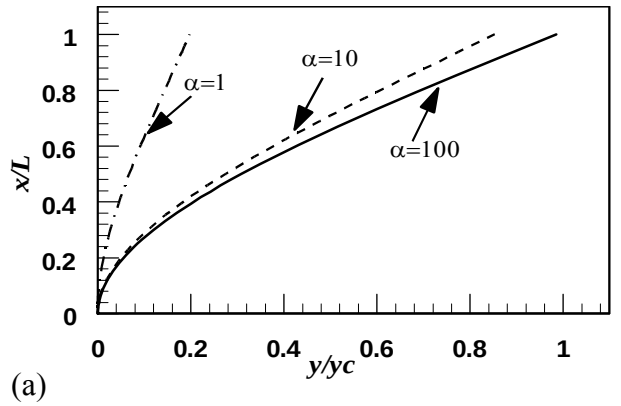

(a)

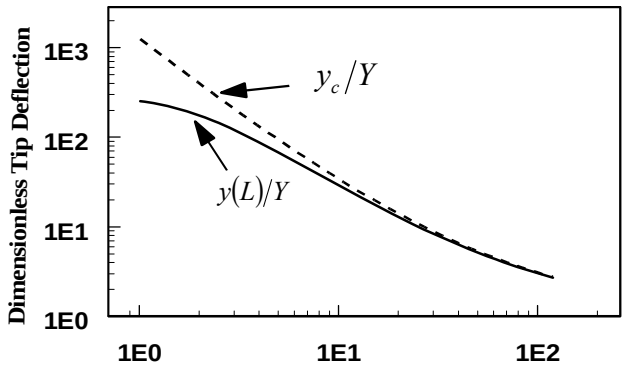

(b)

Figure 4-4. Dimensionless lateral deflection of structural elements and its scale. (a) Dimensionless lateral deflections y/y_c of the structural element along its length for various values of α for steady shear. (b) Dimensionless lateral tip deflection $y(L)/Y$ and dimensionless characteristic deflection y_c/Y as a function of α for steady shear, when $L/r_f = 30$.

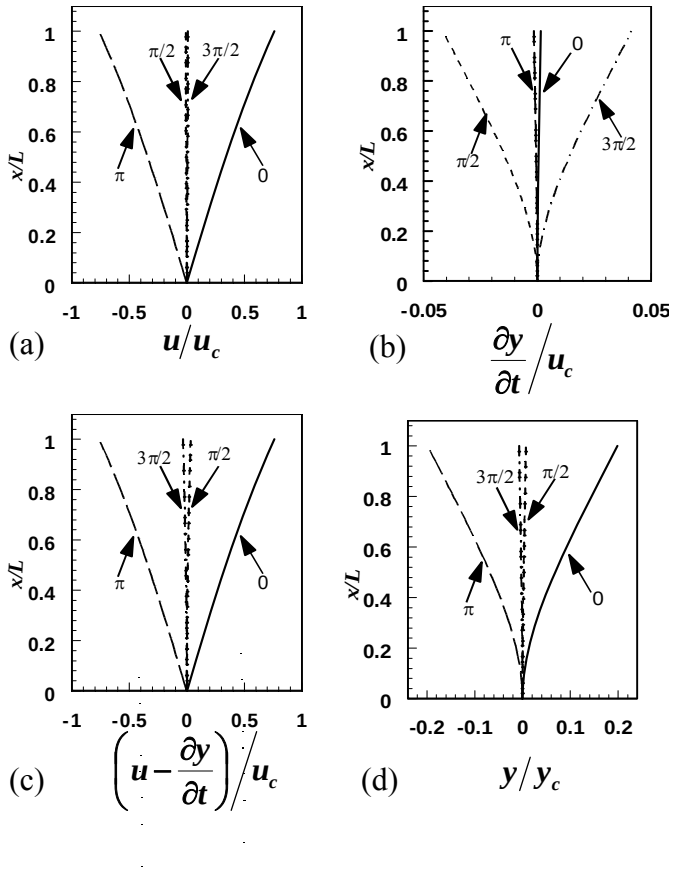

Figure 4-5. Theoretical predictions for (a) the dimensionless fluid velocity profile u/u_c, (b) the dimensionless local velocity of the structural elements $(\partial y/\partial t)/u_c$, (c) the dimensionless local relative velocity between the fluid and the elements $(u-\partial y/\partial t)/u_c$, and (d) the resultant dimensionless deflection of the elements y/y_c at different phase positions for $\alpha = 1$, $\omega_c = 10$ rad/s and $\omega = 2\pi$ rad/s.

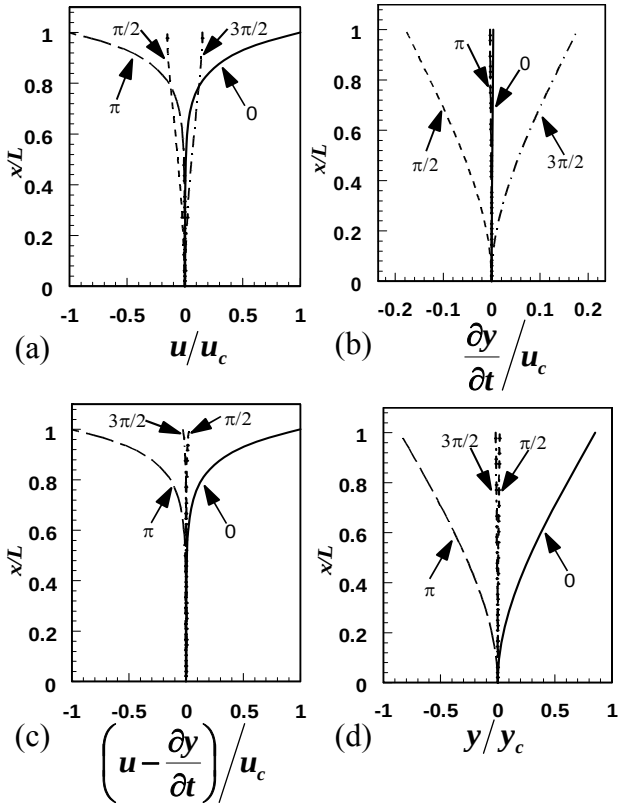

Figure 4-6. Theoretical predictions for (a) the dimensionless fluid velocity profile u/u_c, (b) the dimensionless local velocity of the structural elements $(\partial y/\partial t)/u_c$, (c) the dimensionless local relative velocity between the fluid and the elements $(u-\partial y/\partial t)/u_c$, and (d) the resultant dimensionless deflection of the elements y/y_c at different phase positions for $\alpha = 10$, $\omega_c = 100$ rad/s and $\omega = 2\pi$ rad/s.

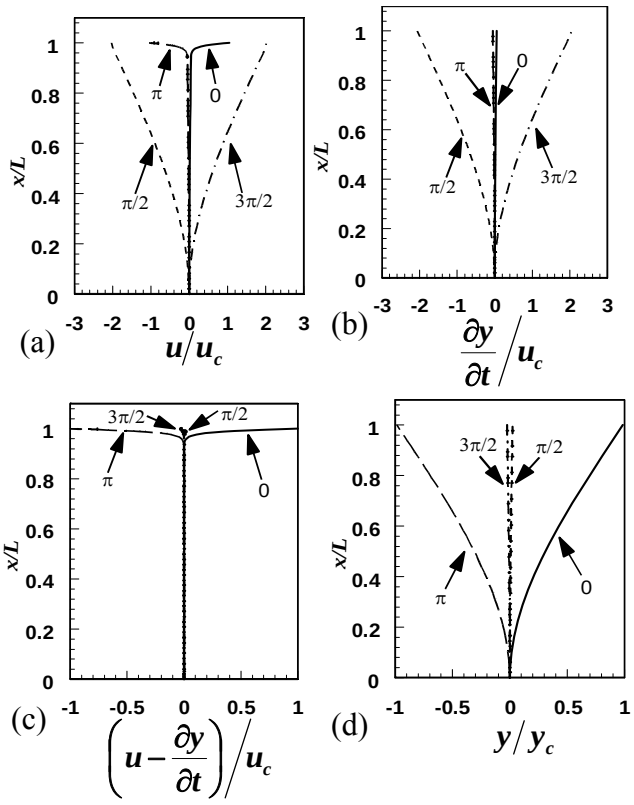

Figure 4-7. Theoretical predictions for (a) the dimensionless fluid velocity profile u/u_c, (b) the dimensionless local velocity of the structural elements $(\partial y/\partial t)/u_c$, (c) the dimensionless local relative velocity between the fluid and the elements $(u-\partial y/\partial t)/u_c$, and (d) the resultant dimensionless deflection of the elements y/y_c at different phase positions for $\alpha = 100$, $\omega_c = 100$ rad/s and $\omega = 2\pi$ rad/s.

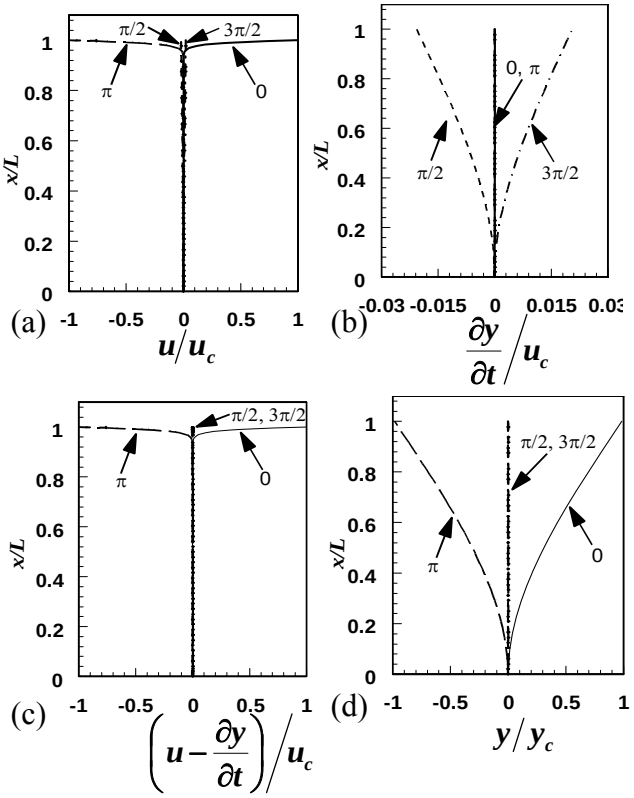

Figure 4-8. Theoretical predictions for (a) the dimensionless fluid velocity profile u/u_c, (b) the dimensionless local velocity of the structural elements $(\partial y/\partial t)/u_c$, (c) the dimensionless local relative velocity between the fluid and the elements $(u-\partial y/\partial t)/u_c$, and (d) the resultant dimensionless deflection of the elements y/y_c at different phase positions for $\alpha = 100$, $\omega_c = 10^4$ rad/s and $\omega = 2\pi$ rad/s.

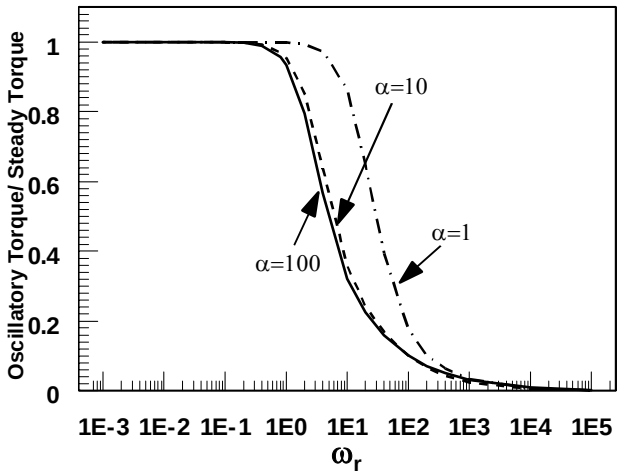

Figure 4-9. The oscillatory torque amplitude normalized by its corresponding value in steady shear as a function of the dimensionless frequency ω_r for various values of α.

Figure 4-10

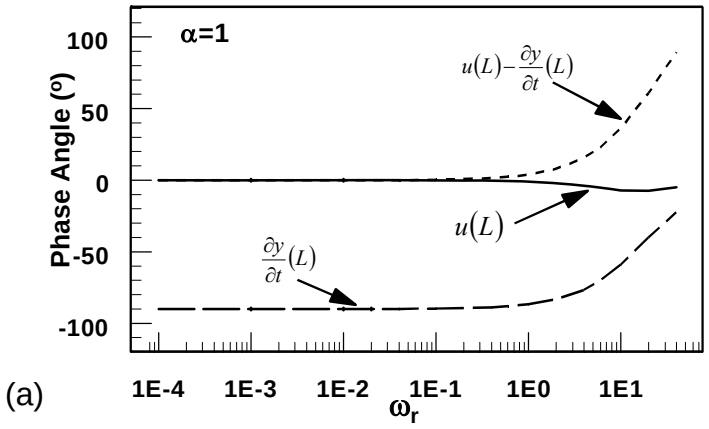

(a)

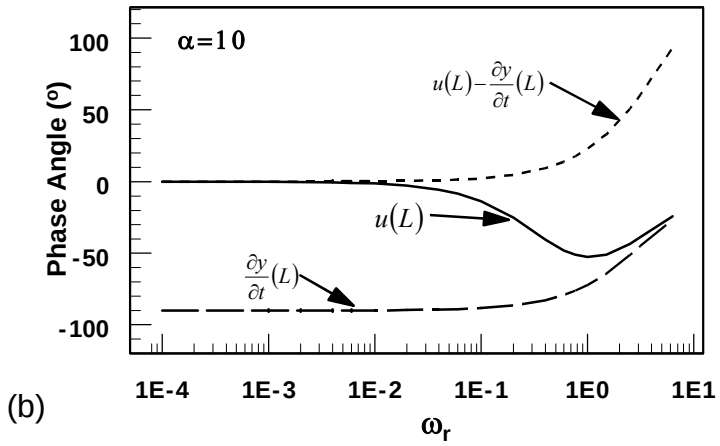

(b)

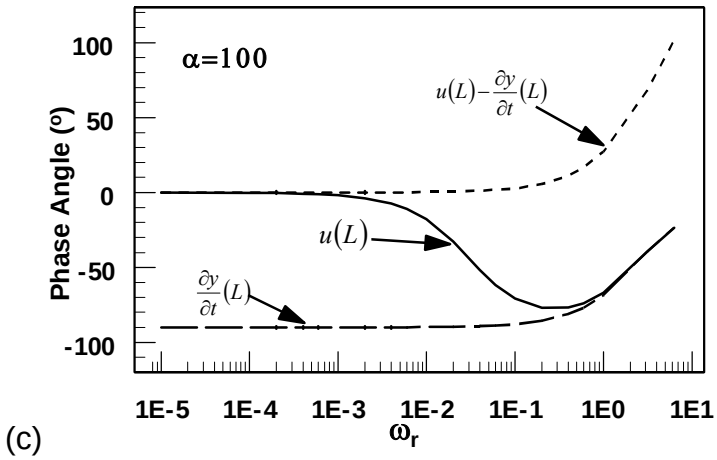

(c)

Figure 4-10. Variation of the phase angle for the fluid velocity, the structural element velocity and the relative velocity between the fluid and structural element at $x = L$ as a function of the dimensionless frequency ω_r for (a) $\alpha = 1$, (b) $\alpha = 10$ and (c) $\alpha = 100$.

Figure 4-11

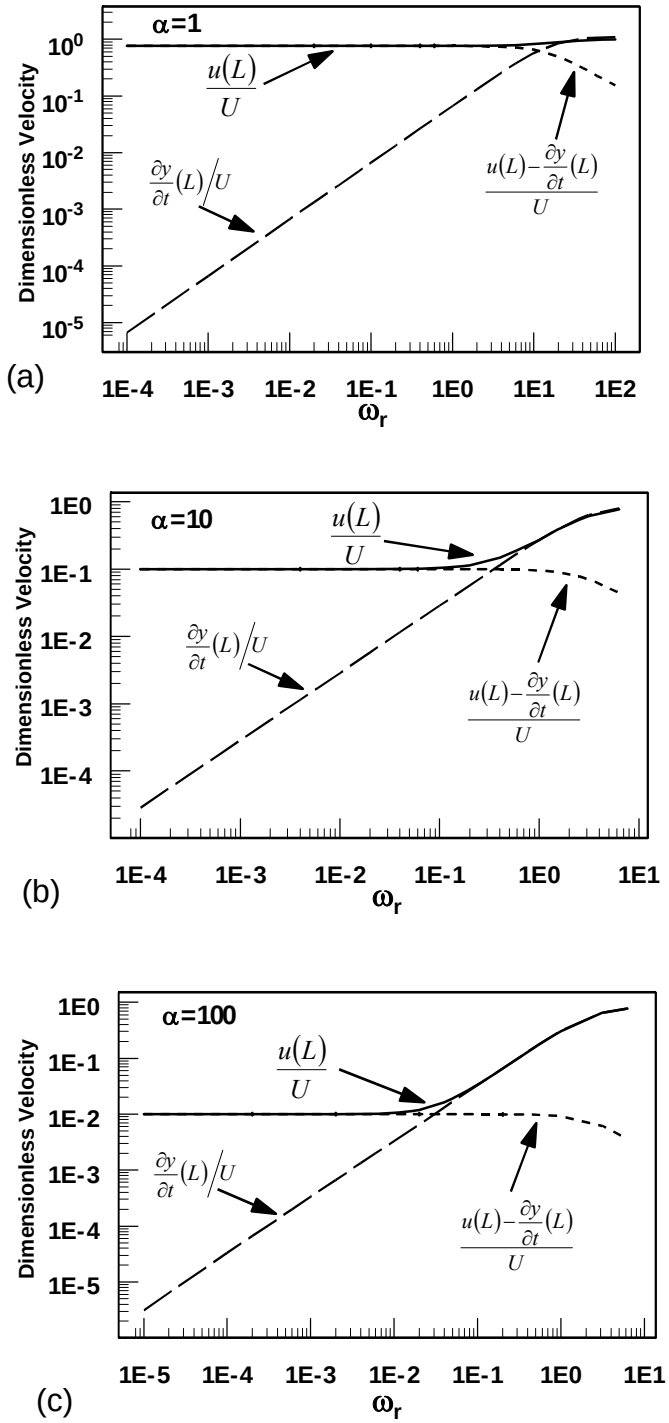
α=1
Dimensionless Velocity
10^0
10^-1
10^-2
10^-3
10^-4
10^-5
u(L)/U
∂y/∂t (L)/U
u(L)−∂y/∂t (L) / U
1E-4 1E-3 1E-2 1E-1 1E0 1E1 1E2
ω_r
(a)
α=10
1E0
1E-1
1E-2
1E-3
1E-4
1E-4 1E-3 1E-2 1E-1 1E0 1E1
(b)
α=100
1E-5
1E-5 1E-4 1E-3 1E-2 1E-1 1E0 1E1
(c)

Figure 4-11. Variation of the magnitude for the fluid velocity, the structural element velocity and the relative velocity between the fluid and structural element at $x = L$ as a function of the dimensionless frequency ω_r for (a) $\alpha = 1$, (b) $\alpha = 10$ and (c) $\alpha = 100$. Note that the velocities are scaled by $U = \tau_0 L/\mu$.

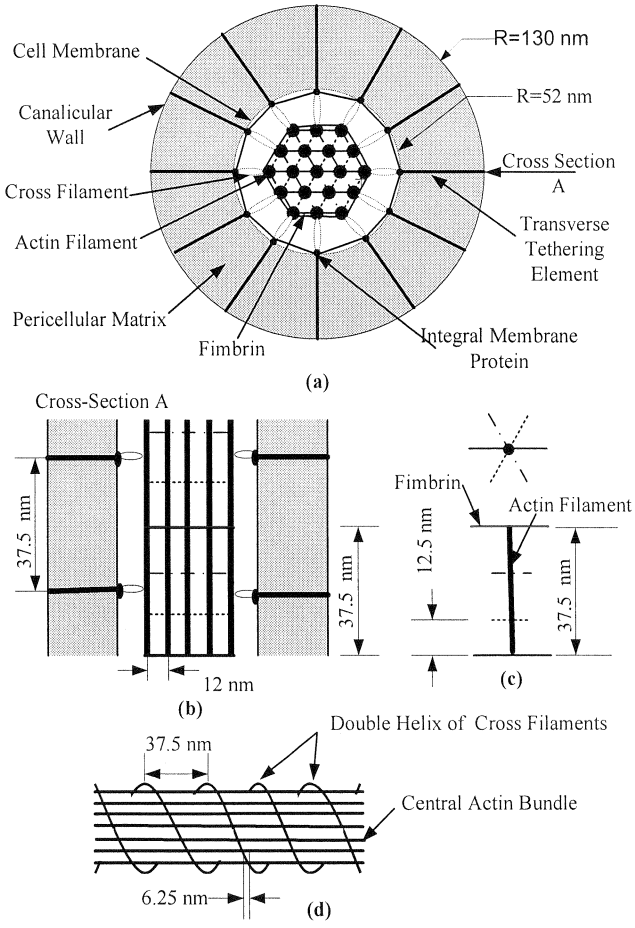

Figure 5-1. Sketches (not to scale) of the osteocyte process and its attachment to the canalicular wall which show the structure of the central hexagonally packed actin filament bundle and the arrangement of the fimbrin crossbridges, the cross-filaments, and the transverse elements. (a) Radial cross section; (b) Longitudinal cross section (cross-section A); (c) Organization of fimbrin cross linkages along an interior actin filament; and (d) Spiraling double helical coil of cross-filaments around the central actin bundle.

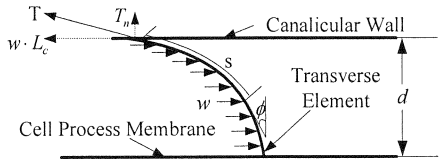

Figure 5-2. Model of the deflection of each transverse element due to the hydrodynamic loading w.

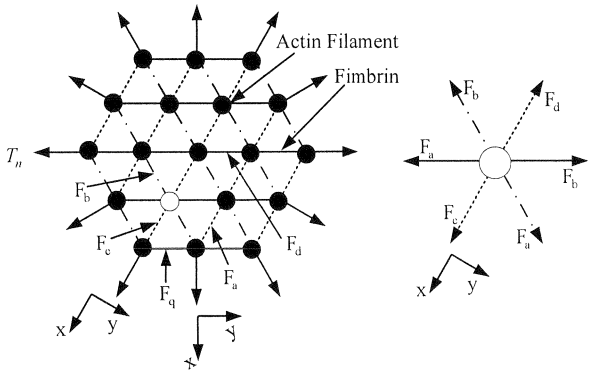

Figure 5-3. Static force analysis on the central actin filament bundle of the cell process. (a) Axial cross section of the entire bundle; (b) Enlarged view of the loading on a single interior filament, open circle in (a).

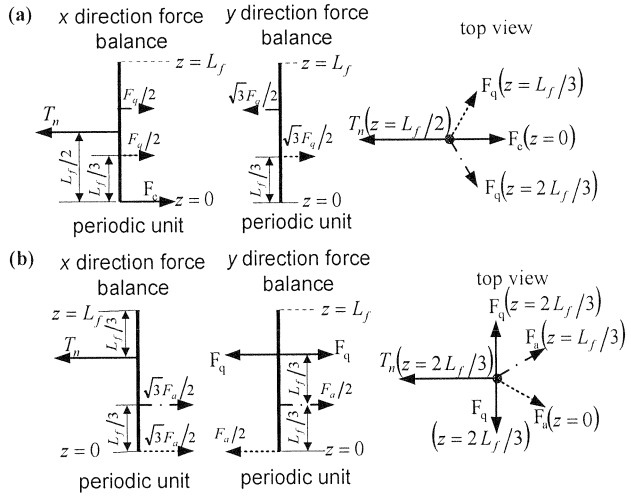

Figure 5-4. Loading of outer filaments ring. (a) Force balance on the actin filament at the corner of outer filament ring (see Fig. 5-3) of the bundle. (b) Force analysis on the actin filament at the middle of outer filament ring (see Fig. 5-3) of the bundle.

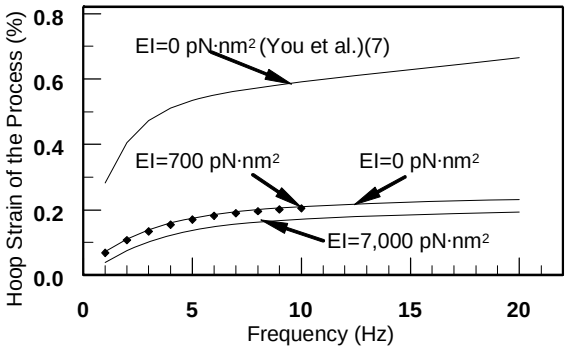

Figure 5-5. The hoop strain of the osteocyte process as a function of loading frequency for tissue loading σ of 1 MPa.

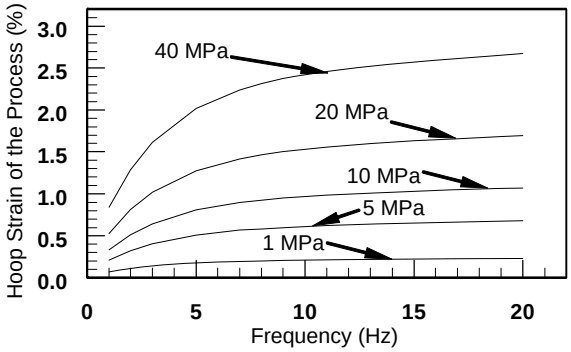

Figure 5-6. Hoop strain of the osteocyte process is plotted as a function of loading frequency with tissue loading amplitude as a parameter. Note EI can approximately treated as zero for loads > 1 MPa.

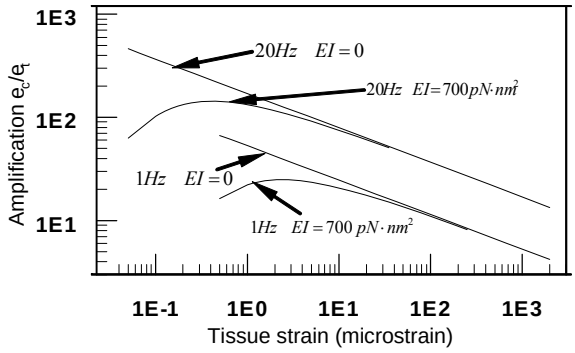

Figure 5-7**.** Strain amplification ratio, the ratio of cellular level cytoskeletal hoop strain ε_c to whole tissue strain ε_t as a function of whole tissue strain at two frequencies, 1 and 20 Hz, for *EI = 0* and *EI = 700 pN·nm²* (Weinbaum et al. 2003)

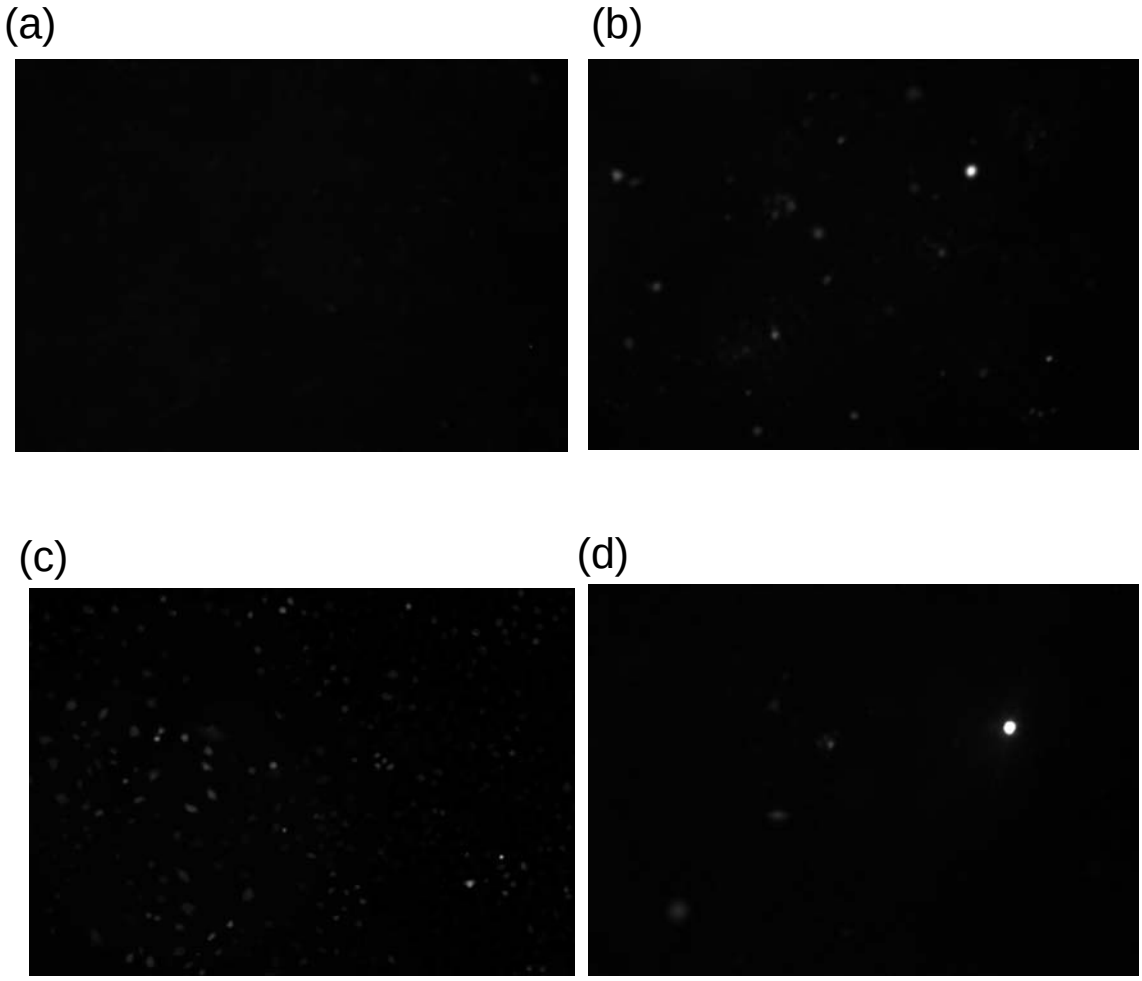

Figure 6-1. Fluorescent Images of YoPro taken up by MLO-Y4 cells. (a) The cells were incubated with regular PBS for 10 minutes; (b) The cells were incubated with Ca^{2+} and Mg^{2+} free PBS for 10 minutes; (c) The cells are incubated with Ca^{2+} and Mg^{2+} free PBS with 1 mM ATP for 10 minutes; (d) The cells were incubated with Ca^{2+} and Mg^{2+} free PBS with 1 mM ATP and 10 μM KN-62 (1-[N,O-Bis(5-isoquinolinesulfonyl)-N-methyl-L-tyrosyl]-4-phenylpipera zine) for 10 minutes after being treated with 10 μM KN-62 for 20 minutes.

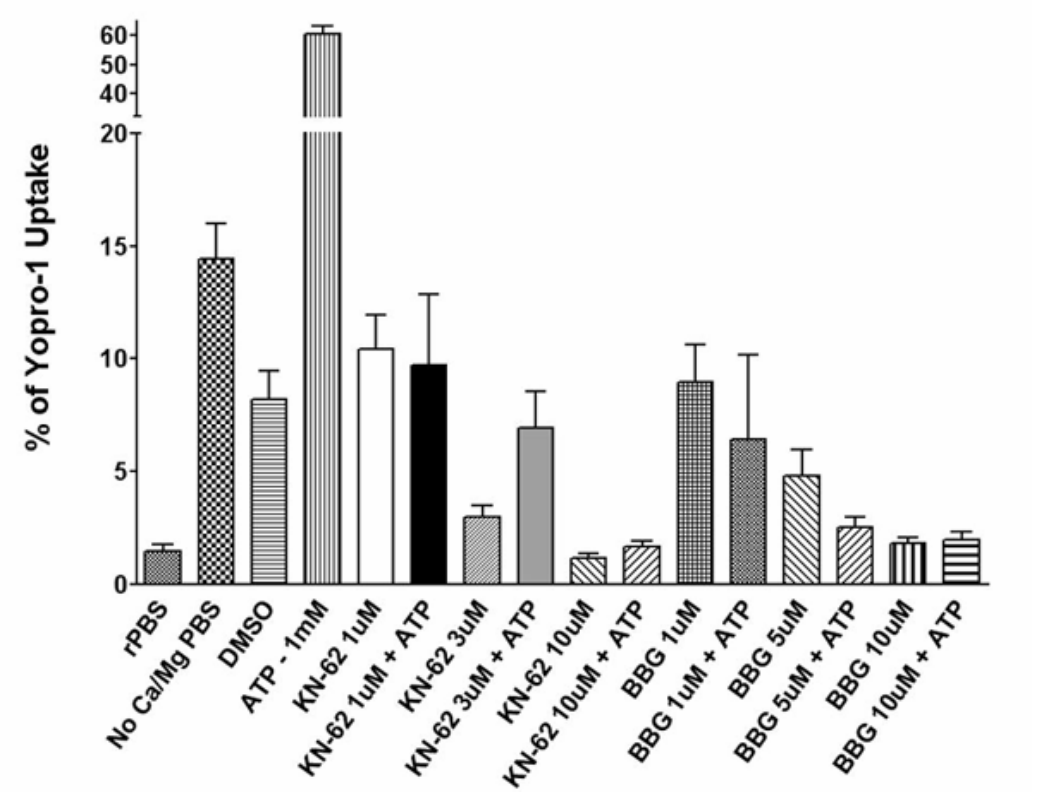

Figure 6-2. Percentages of fluorescence-positive MLO-Y4 cells treated with various agonists and antagonists with varying concentrations. rPBS denotes regular PBS; No Ca/Mg denotes Ca^{2+} and Mg^{2+} free PBS; DMSO denotes Dimethyl Sulfoxide; KN-62 denotes 1-[N,O-Bis(5-isoquinolinesulfonyl)-N-methyl-L-tyrosyl]-4-phenylpiperazine; and BBG denotes Brilliant Blue G.

Appendix A Derivation of the drag force F_D

Weinbaum et al. (1994) predicted the fluid flow in the fiber-filled annular space between the cell process membrane and the canalicular wall when bones experience mechanical loading using a mathematical model. Using this method, You et al. (2001) calculated the drag force F_D on the transverse elements per unit length of the cell process and showed that

$$F_D = 2\pi\int_{R_0}^{R_1}\rho\left(\frac{\mu}{K_P}u\right)d\rho$$
$$= 2\pi\frac{\partial P}{\partial z}\left\{\frac{R_1^{\,2}}{\gamma}\left[A_1 I_1(\gamma) - B_1 K_1(\gamma)\right] - \frac{R_1^{\,2}}{\gamma q}\left[A_1 I_1\left(\frac{\gamma}{q}\right) - B_1 K_1\left(\frac{\gamma}{q}\right)\right] - \frac{R_1^{\,2} - R_0^{\,2}}{2}\right\}. \quad \textbf{[A-1]}$$

Here R_0 is the radius of the cell process; R_1 is the radius of the canaliculi; ρ is the radial coordinate of the canaliculi; μ is the fluid viscosity and u is fluid velocity; K_P is the Darcy permeability of the matrix in the annular space; P is the local fluid pressure; z is the axial coordinate along the cell process; $I_1(x)$ and $K_1(x)$ are modified Bessel functions of the first and seconded kind, respectively; $\gamma = R_1/\sqrt{K_P}$; $q = R_1/R_0$; and A_1 and B_1 are given by

$$A_1 = \frac{K_0(\gamma) - K_0(\gamma/q)}{I_0(\gamma/q)K_0(\gamma) - I_0(\gamma)K_0(\gamma/q)} \text{ and } B_1 = \frac{I_0(\gamma/q) - I_0(\gamma)}{I_0(\gamma/q)K_0(\gamma) - I_0(\gamma)K_0(\gamma/q)}. \quad \textbf{[A-2a,b]}$$

In this model the drag on the GAG sidechains of the transverse tethering filament is described by the model for K_P in You et al. (2001). $\partial P/\partial z$ is the only quantity in Eq. **A-1** that is related to tissue loading. Using Biot theory, Zeng et al. (1994) show that

the pressure field in an osteon under sinusoidal loading perpendicular to its axis is given by

$$P = \frac{B\sigma}{3}\Re e\left\{e^{i\cdot\omega t}\cdot\left[A_0 I_0\left(z\cdot\sqrt{i\cdot\frac{\omega}{c}}\right)+B_0 K_0\left(z\cdot\sqrt{i\cdot\frac{\omega}{c}}\right)\right]\right\}+\frac{B\sigma\sin(\omega t)}{3} \qquad \textbf{[A-3]}$$

Here B (=0.53) is a factor relating the compressibility of the bone matrix to the bone fluid; c is the pore fluid diffusion coefficient; σ and ω are the amplitude and the angular frequency of the applied sinusoidal stress; t is the time variable; $I_0(x)$ and $K_0(x)$ are modified Bessel functions of the first and second kind of zero order; and A_0 and B_0 are given by

$$A_0 = \frac{i\cdot K_1\left(r_o\sqrt{i\cdot\frac{\omega}{c}}\right)}{I_0\left(r_i\sqrt{i\cdot\frac{\omega}{c}}\right)\cdot K_1\left(r_o\sqrt{i\cdot\frac{\omega}{c}}\right)+I_1\left(r_o\sqrt{i\cdot\frac{\omega}{c}}\right)\cdot K_0\left(r_i\sqrt{i\cdot\frac{\omega}{c}}\right)}, \qquad \textbf{[A-4a]}$$

$$B_0 = \frac{i\cdot I_1\left(r_o\sqrt{i\cdot\frac{\omega}{c}}\right)}{I_0\left(r_i\sqrt{i\cdot\frac{\omega}{c}}\right)\cdot K_1\left(r_o\sqrt{i\cdot\frac{\omega}{c}}\right)+I_1\left(r_o\sqrt{i\cdot\frac{\omega}{c}}\right)\cdot K_0\left(r_i\sqrt{i\cdot\frac{\omega}{c}}\right)}, \qquad \textbf{[A-4b]}$$

where r_i is the radius of the osteonal lumen; r_o is its outer radius of the osteon at the cement line and $I_1(x)$ and $K_1(x)$ are modified Bessel functions of the first and second kind of first order.

Appendix B Deflection of the outermost actin filaments of the central actin filament bundle

B1. Deflection of the outermost actin filaments at corner positions

Due to the symmetric loading in Fig. **5-4(a)**, we require that the radial deflection, υ_x, and its gradient, $\partial\upsilon_x/\partial z$, be zero where the force F_c is applied. These are the boundary conditions for a uniform beam with fixed ends shown in Fig. **B-1**. For such a beam, the deflection v due to the action of a concentrated loading, F, is (Gere and Timoshenko 1990)

$$v=\frac{Fx^2(3a-x)}{6EI}+\frac{Fba^2x^2}{2EI\cdot L^2}-\frac{Fa^2(a+3b)x^2(3L-x)}{6EI\cdot L^3}\quad 0\le x\le a\,. \qquad \textbf{[B-1]}$$

Applying Eq. **B-1** for the force $F_q/2$ at $z=\frac{L_f}{3}$ in Fig. **5-4a**, one obtains

$$\upsilon_{x,1}=\begin{cases}\dfrac{\left(\frac{F_q}{2}\right)z^2(L_f-z)}{6EI_a}+\dfrac{\left(\frac{F_q}{2}\right)\left(\frac{2L_f}{3}\right)\left(\frac{L_f}{3}\right)^2z^2}{2EI_a\cdot L_f{}^2}-\dfrac{\left(\frac{F_q}{2}\right)\left(\frac{L_f}{3}\right)^2\left(\frac{L_f}{3}+2L_f\right)z^2(3L_f-z)}{6EI_a\cdot L_f{}^3}, & 0\le z\le\frac{L_f}{3};\\ \dfrac{\left(\frac{F_q}{2}\right)(L_f-z)^2(L_f+z)}{6EI_a}+\dfrac{\left(\frac{F_q}{2}\right)\left(\frac{L_f}{3}\right)\left(\frac{2L_f}{3}\right)^2(L_f-z)^2}{2EI_a\cdot L_f{}^2}-\dfrac{\left(\frac{F_q}{2}\right)\left(\frac{2L_f}{3}\right)^2\left(\frac{2L_f}{3}+L_f\right)(L_f-z)^2(2L_f+z)}{6EI_a\cdot L_f{}^3}. & \frac{L_f}{3}\le z\le L_f.\end{cases} \qquad \textbf{[B-2]}$$

Similarly, for the force T_n at $z=\frac{L_f}{2}$, one finds

$$\upsilon_{x,2}=\begin{cases}\dfrac{T_n z^2\left(\dfrac{3L_f}{2}-z\right)}{6EI_a}+\dfrac{T_n\left(\dfrac{L_f}{2}\right)^3 z^2}{2EI_a\cdot L_f{}^2}-\dfrac{T_n\left(\dfrac{L_f}{2}\right)^2\left(\dfrac{L_f}{2}+\dfrac{3L_f}{2}\right)z^2\left(3L_f-z\right)}{6EI_a\cdot L_f{}^3}, & 0\le z\le\dfrac{L_f}{2};\\ \dfrac{T_n\left(L_f-z\right)^2\left(\dfrac{L_f}{2}+z\right)}{6EI_a}+\dfrac{T_n\left(\dfrac{L_f}{2}\right)^3\left(L_f-z\right)^2}{2EI_a\cdot L_f{}^2}-\dfrac{T_n\left(\dfrac{L_f}{2}\right)^2\left(\dfrac{L_f}{2}+\dfrac{3L_f}{2}\right)\left(L_f-z\right)^2\left(2L_f+z\right)}{6EI_a\cdot L_f{}^3}, & \dfrac{L_f}{2}\le z\le L_f.\end{cases}$$

[B-3]

For the force $F_q/2$ at $z=\dfrac{2L_f}{3}$,

$$\upsilon_{x,3}=\begin{cases}\dfrac{\left(\dfrac{F_q}{2}\right)z^2\left(2L_f-z\right)}{6EI_a}+\dfrac{\left(\dfrac{F_q}{2}\right)\left(\dfrac{L_f}{3}\right)\left(\dfrac{2L_f}{3}\right)^2 z^2}{2EI_a\cdot L_f{}^2}-\dfrac{\left(\dfrac{F_q}{2}\right)\left(\dfrac{2L_f}{3}\right)^2\left(\dfrac{2L_f}{3}+L_f\right)z^2\left(3L_f-z\right)}{6EI_a\cdot L_f{}^3}, & 0\le z\le\dfrac{2L_f}{3};\\ \dfrac{\left(\dfrac{F_q}{2}\right)\left(L_f-z\right)^2 z}{6EI_a}+\dfrac{\left(\dfrac{F_q}{2}\right)\left(\dfrac{2L_f}{3}\right)\left(\dfrac{L_f}{3}\right)^2\left(L_f-z\right)^2}{2EI_a\cdot L_f{}^2}-\dfrac{\left(\dfrac{F_q}{2}\right)\left(\dfrac{L_f}{3}\right)^2\left(\dfrac{L_f}{3}+2L_f\right)\left(L_f-z\right)^2\left(2L_f+z\right)}{6EI_a\cdot L_f{}^3}, & \dfrac{2L_f}{3}\le z\le L_f.\end{cases}$$

[B-4]

The total deflection in the *x* direction in Fig. **5-4(a)** is

$$\upsilon_x=-\upsilon_{x,1}+\upsilon_{x,2}-\upsilon_{x,3}. \qquad \textbf{[B-5]}$$

The maximum defection in the *x* direction in Fig. **5-4(a)** occurs at $z=\dfrac{L_f}{2}$ due to symmetry. Substituting $z=\dfrac{L_f}{2}$ into Eq. **B-5** and simplifying, one obtains Eq. **5-5** in the text.

The deflection in the *y* direction, υ_y, in Fig. **5-4(a)** is zero at $z=0$ and L_f due to the periodic loading and its gradient, $\partial\upsilon_y/\partial z$, is automatically continuous when one models the actin filament as a simply-supported beam shown in Fig. **B-2**. The

deflection v of a simply-supported beam due to the action of a concentrated loading, F, is (Gere and Timoshenko 1990)

$$v = \frac{Fbx}{6L \cdot EI}\left(L^2 - b^2 - x^2\right) \quad 0 \le x \le a\,. \qquad \textbf{[B-6]}$$

Hence, for the force $\sqrt{3}F_q/2$ at $z = \frac{L_f}{2}$, Eq. **B-6** gives

$$\upsilon_{y,1} = \begin{cases} \dfrac{\left(\frac{\sqrt{3}F_q}{2}\right)\left(\frac{2L_f}{3}\right)z}{6EI_a \cdot L_f}\left[{L_f}^2 - \left(\frac{2L_f}{3}\right)^2 - z^2\right], & 0 \le z \le \frac{L_f}{3}; \\ \dfrac{\left(\frac{\sqrt{3}F_q}{2}\right)\left(\frac{L_f}{3}\right)\left(L_f - z\right)}{6EI_a \cdot L_f}\left[{L_f}^2 - \left(\frac{L_f}{3}\right)^2 - \left(L_f - z\right)^2\right], & \frac{L_f}{3} \le z \le L_f, \end{cases}$$

[B-7]

whereas for the force $\sqrt{3}F_q/2$ at $z = \frac{2L_f}{3}$

$$\upsilon_{y,2} = \begin{cases} \dfrac{\left(\frac{\sqrt{3}F_q}{2}\right)\left(\frac{L_f}{3}\right)z}{6EI_a \cdot L_f}\left[{L_f}^2 - \left(\frac{L_f}{3}\right)^2 - z^2\right], & 0 \le z \le \frac{2L_f}{3}; \\ \dfrac{\left(\frac{\sqrt{3}F_q}{2}\right)\left(\frac{2L_f}{3}\right)\left(L_f - z\right)}{6EI_a \cdot L_f}\left[{L_f}^2 - \left(\frac{2L_f}{3}\right)^2 - \left(L_f - z\right)^2\right], & \frac{2L_f}{3} \le z \le L_f. \end{cases} \qquad \textbf{[B-8]}$$

The total lateral defection in Fig.**5-4(a)** is given by

$$\upsilon_y = -\upsilon_{y,1} + \upsilon_{y,2}\,. \qquad \textbf{[B-9]}$$

B2. The deflection of the outermost actin filaments in central positions

Fig. **B-3** shows force balance in the *x* direction in Fig. **5-4(b)** as the combined loading two isolated spans. In this figure, we replace forces $\sqrt{3}F_q/2$ at $z=0, \frac{L_f}{3}$ and L_f as three joint supports. M_A, M_B and M_C denote the redundant bending moments on the actin filament. We assume they are positive (causing compression on the top of the beam) for convenience. The three-moment equation is given by (Gere and Timoshenko 1990)

$$M_A L_{AB} + 2M_B\left(L_{AB}+L_{BC}\right)+M_C L_{BC} = -\frac{6A_{AB}\overline{Z}_{AB}}{L_{AB}} - \frac{6A_{BC}\overline{Z}_{BC}}{L_{BC}} \qquad \textbf{[B-10]}$$

Here $L_{AB}=\frac{L_f}{3}$ and $L_{BC}=\frac{2L_f}{3}$; A is the area of the bending moment diagram for a single span ($A_{AB}=0$ and $A_{BC}=\frac{T_n L_{BC}^2}{8}$); $\overline{Z}$ is the centroid of the area along the span ($\overline{Z}_{BC}=\frac{L_{BC}}{2}$). Due to periodicity, one obtains,

$$M_A = M_B = M_c = M_0 \qquad \textbf{[B-11]}$$

One solves Eqs. **B-10** and **B-11** and obtains

$$M_0 = \frac{T_n L_f}{18} \qquad \textbf{[B-12]}$$

For the span *AB* in Fig. **B-3**, the deflection due to the two equal and positive bending moments at the two ends is (Gere and Timoshenko 1990)

$$v_{x,AB} = \frac{M_0 z}{2EI}\left(\frac{L_f}{3}-z\right) = \frac{T_n L_f z}{36EI}\left(\frac{L_f}{3}-z\right) \qquad 0 \le z \le \frac{L_f}{3} \qquad \textbf{[B-13]}$$

Similarly, one obtains the deflection of the span *BC* due to the bending moments

$$v_{x,BC,1} = \frac{M_0\left(z-\frac{L_f}{3}\right)}{2EI}\left(L_f - z\right) = \frac{T_n L_f}{36EI}\left(z-\frac{L_f}{3}\right)\left(L_f - z\right) \qquad \frac{L_f}{3} \le z \le L_f \quad \textbf{[B-14]}$$

One applies Eq. B6 to obtain the deflection of span *BC* in Fig. **B-3** due to force T_n at $z = \frac{2L_f}{3}$

$$v_{x,BC,2} = \begin{cases} \frac{T_n\left(z-\frac{L_f}{3}\right)}{48EI}\left(2L_f - 4\left(z-\frac{L_f}{3}\right)^2\right); & \frac{L_f}{3} \le z \le \frac{2L_f}{3} \\ \frac{T_n\left(L_f - z\right)}{48EI}\left[2L_f - 4\left(L_f - z\right)^2\right] & \frac{2L_f}{3} \le z \le L_f \end{cases} \quad \textbf{[B-15]}$$

The total deflection in the *x* direction of Fig. **5-4(b)** is

$$v_x = -v_{x,AB} - v_{x,BC,1} + v_{x,BC,2} \quad \textbf{[B-16]}$$

The maximum deflection in the *x* direction in Fig. **5-4(b)** occurs at $z = \frac{2L_f}{3}$. One obtains Eq. **6** in the text by substituting $z = \frac{2L_f}{3}$ into Eq. **B-16** and simplifying.

The force balance in the *y* direction in Fig. **5-4(b)** is same as the one in Fig. **5-4(a)** since the pair of Fq in Fig. **5-4(b)** cancel each other, except that the force amplitude changes and the force action points shift downward by $\frac{L_f}{3}$. Hence, one can obtain the lateral deflection v_y by replacing $\sqrt{3}F_q/2$ by $F_a/2$ and z by $z + \frac{L_f}{3}$ in Eq. **B-9**. However, only the *y* deflection of the actin filaments at $z = \frac{2L_f}{3}$, where T_n or F_q

is applied, is needed in the following analysis and it is apparent from the force balance in the *y* direction in Fig. **5-4(b)** that the deflection is zero at $z = \frac{2L_f}{3}$ due to symmetry.

B3. Force ratio $q_r = \frac{F_q}{T_n}$

When the central actin bundle is deformed, the distance between the attachment points of the individual fimbrin crossbridges at the adjacent outermost actin filaments, $z = \frac{2L_f}{3}$ in Figs. **5-4(a,b)** in the text, should remain constant at 12 nm, since fimbrin is assumed to be inextensible. Hence, one needs to obtain the radial (*x*) and lateral (*y*) deflections at $z = \frac{2L_f}{3}$ where F_q is applied (see Figs. **5-1** and **5-4(a,b)**) to satisfy this geometric constraint. This constraint is schematically shown in Fig. **B-1** and analytically given by

$$\sqrt{(x_0 - x_1)^2 + (y_0 - y_1)^2} = 12\ nm\,. \qquad \textbf{[B-17]}$$

(x_0, y_0) and (x_1, y_1) can be geometrically related to the *x* and *y* deflections of the actin filaments shown in Figs. **5-4(a,b)** These relations are given by

$$x_0 = \upsilon_{x,q},\ y_0 = \upsilon_{y,q};\quad x_1 = -6 + \frac{\sqrt{3}}{2}\nu_{x,q},\ y_1 = 6\sqrt{3} + \frac{1}{2}\nu_{x,q}. \qquad \textbf{[B-18a,b,c,d]}$$

Here $\upsilon_{r,q}$ and $\upsilon_{y,q}$ are the *x* and *y* deflections of the actin filament at $z = \frac{2L_f}{3}$ in Fig. **5-4(a)**; and $\nu_{r,q}$ is the *x* deflection of the actin filament at $z = \frac{2L_f}{3}$ in Fig. **5-4(b)**.

Substituting $z = \frac{2L_f}{3}$ into Eq **B-5**, one finds

$$\upsilon_{x,q} = \left(\frac{5}{1296} - \frac{q_r}{324}\right)\frac{T_n L_f^{\,3}}{EI_a}. \qquad \textbf{[B-19]}$$

Similarly, from Eq. **B-9** one finds

$$\upsilon_{y,q} = \frac{\sqrt{3}q_r T_n L_f^{\,3}}{972EI_a}. \qquad \textbf{[B-20]}$$

One substitutes $z = \frac{2L_f}{3}$ into Eq. **B-16** and finds

$$\nu_{x,q} = \frac{T_n L_f^{\,3}}{324EI_a}. \qquad \textbf{[B-21]}$$

Combining Eqs. B-**18~B-21,** one obtains

$$x_0 - x_1 = 6 + \left(\frac{5}{192} - \frac{q_r}{324} - \frac{\sqrt{3}}{628}\right)\beta; \quad y_0 - y_1 = \left(\frac{\sqrt{3}q_r}{972} - \frac{1}{628}\right)\beta - 6\sqrt{3}. \qquad \textbf{[B-22a, b]}$$

Here $q_r = \frac{F_q}{T_n}$ and $\beta = \frac{T_n L_f^{\,3}}{EI}$. Substituting Eqs. **B-22a**, **b** into Eq. **B-17** and solving, one obtains

$$q_r = \frac{1}{128\beta}\left[37324 + \left(120 - 64\sqrt{3}\right)\beta \pm 8\sqrt{2176782336 + \left(466560 - 746496\sqrt{3}\right)\beta + \left(240\sqrt{3} - 651\right)\beta^2}\right]$$

.

[B-23]

Note that the '+' root has no physical meaning since q_r is undefined as $\beta \to 0$. The physically meaningful solution for q_r using the − root is plotted as a function of β in Fig. **B-5**.

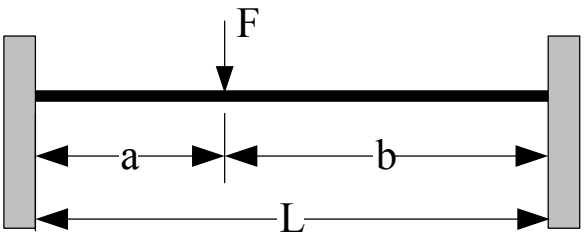

Figure B-1. A fixed-end uniform beam with a concentrated load.

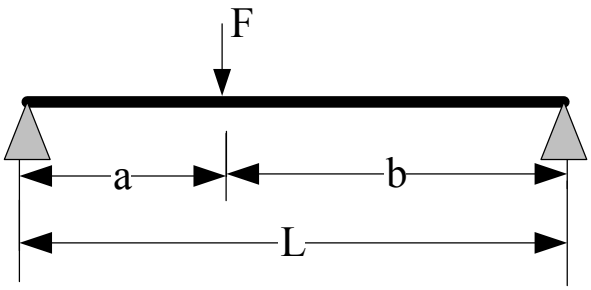

Figure B-2. A simply-supported uniform beam with a concentrated load.

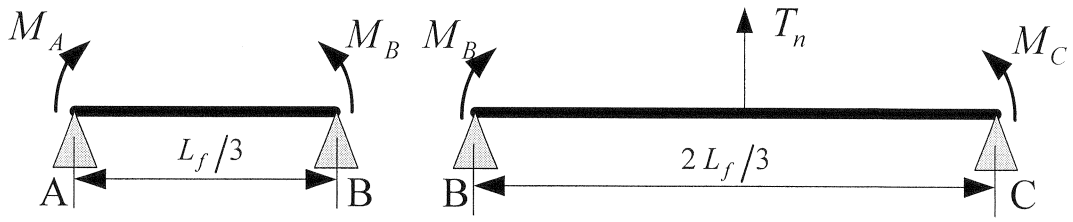

Figure B-3. The outer middle actin filament modeled as two simply-supported spans in the case of deflection in the x direction: span AB with applied bending moments, MA and MB and span BC with an applied concentrated load T_n and bending moments, MB and MC.

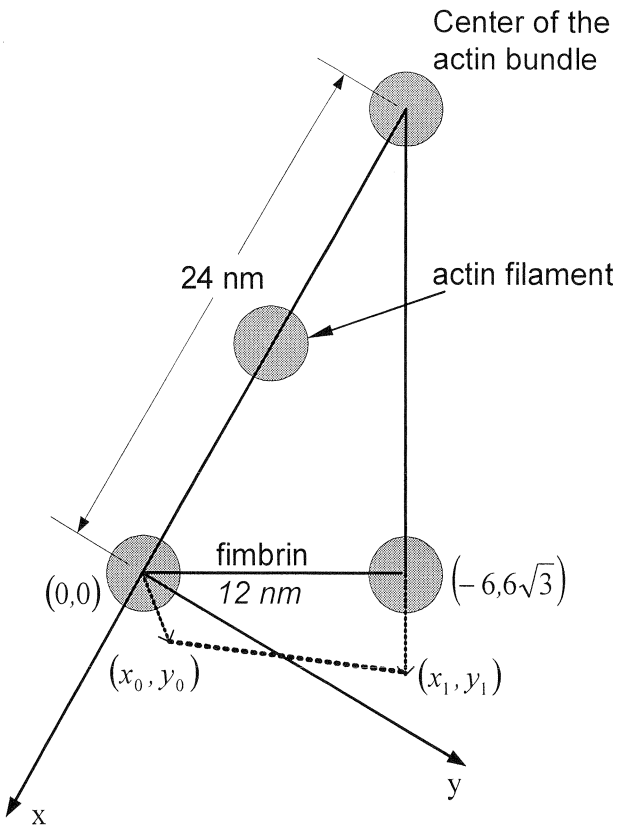

Figure B-4. A sketch of the geometric constraint of the deflections of the outermost actin filaments of the central actin bundle. The plane shown is at $z = \frac{2L_f}{3}$ in Figs. 5-4a, b. This constraint requires that the displaced fimbrin crossbridge have its length unchanged.

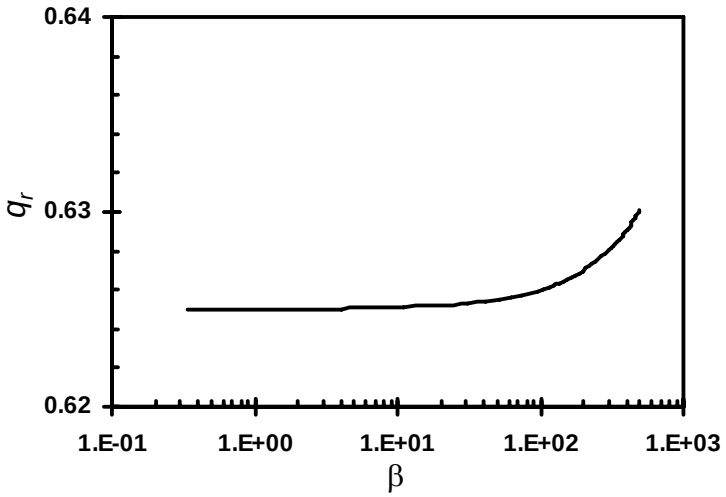

Figure B-5. $q_r = \frac{F_q}{T_n}$ as a function of $\beta = \frac{T_n L_f^{\,3}}{EI}$.

Bibliography

1. Adamson, R. H., Lenz, J. F., Zhang, X., Adamson, G. N., Weinbaum, S. and Curry, F. E. (2004) "Oncotic pressures opposing filtration across non-fenestrated rat microvessels." *J. Physiol.* **557**(Pt 3): 889-907.

2. Almekinders, L. C., Banes, A. J. and Ballenger, C. A. (1993) "Effects of repetitive motion on human fibroblasts." *Med. Sci. Sports. Exerc.* **25**(5): 603-607.

3. Bass, M. D. and Humphries, M. J. (2002) "Cytoplasmic interactions of syndecan-4 orchestrate adhesion receptor and growth factor receptor signalling." *Biochem. J.* **368**(Pt 1): 1-15.

4. Baylink, T. M., Mohan, S., Fitzsimmons, R. J. and Baylink, D. J. (1995). "Evidence that the mitogenic effect of prostaglandin E2 on human bone cells involves protein kinase C and calcium pathways." *J. Bone Miner. Res.* **9** (suppl 31): B23.

5. Blake, J. R. (1971) "A spherical envelope approach to ciliary propulsion." *J. Fluid Mechanics* **46**: 199 - 208.

6. Cheng, B., Zhao, S., Luo, J., Sprague, E., Bonewald, L. F. and Jiang, J. X. (2001). "Expression of functional gap junctions and regulation by fluid flow in osteocyte-like MLO-Y4 cells." *J. Bone Miner. Res.* **16**(2): 249-59.

7. Cherian, P. P., Cheng, B., Gu, S., Sprague, E., Bonewald, L. F. and Jiang, J. X. (2003) "Effects of mechanical strain on the function of Gap junctions in osteocytes are mediated through the prostaglandin EP2 receptor." *J. Biol. Chem.* **278**(44): 43146-43156.

8. Cherian, P. P., Siller-Jackson, A. J., Gu, S., Wang, X., Bonewald, L. F., Sprague, E. and Jiang, J. X. (2005) "Mechanical strain opens connexin 43 hemichannels in osteocytes: a novel mechanism for the release of prostaglandin." *Mol. Biol. Cell* **16**(7): 3100-3106.

9. Cowin, S. C., Weinbaum, S. and Zeng, Y. (1995) ″A case for bone canaliculi as the anatomical site of strain generated potentials.″ *J. Biomechanics* **28**(11): 1281-1297.

10. Damiano, E. R., Duling, B. R., Ley, K. and SKALAK, T. C. (1996) "Axisymmetric pressure-driven flow of rigid pellets through a cylindrical tube lined with a deformable porous wall layer." *J. Fluid Mech.* **314**: 163 - 189.

11. Damiano, E. R. (1998) "The effect of the endothelial-cell glycocalyx on the motion of red blood cells through capillaries." *Microvasc. Res.* **55**(1): 77-91.

12. Damiano, E. R. and Stace, T. M. (2002) "A mechano-electrochemical model of radial deformation of the capillary glycocalyx." *Biophys. J.* **82**(3): 1153-1175.

13. DeRosier, D. J., Tilney, L. G. and Egelman, E. (1980) "Actin in the inner ear: the remarkable structure of the stereocilium." *Nature* **287**(5780): 291-296.

14. Dinchuk, J. E., Car, B. D., Focht, R. J., Johnston, J. J., Jaffee, B. D., Covington, M. B., Contel, N. R., Eng, V. M., Collins, R. J., Czerniak, P. M. and et al. (1995). "Renal abnormalities and an altered inflammatory response in mice lacking cyclooxygenase II." *Nature* **378**(6555): 406-409.

15. Du, Z., Duan, Y., Yan, Q., Weinstein, A. M., Weinbaum, S. and Wang, T. (2004). "Mechanosensory function of microvilli of the kidney proximal tubule." *Proc. Natl. Acad. Sci. USA* **101**(35): 13068-13073.

16. Dupuis, D. E., Guilford, W. H., Wu, J. and Warshaw, D. M. (1997) "Actin filament mechanics in the laser trap." *J. Muscle Res. Cell Motil.* **18**(1): 17-30.

17. Evan, A. P., Satlin, L. M., Gattone, V. H., 2nd, Connors, B. and Schwartz, G. J. (1991) "Postnatal maturation of rabbit renal collecting duct. II. Morphological observations." *Am. J. Physiol.* **261**(1 Pt 2): F91-F107.

18. Feng, J. Ganatos, P. and Weinbaum, S. (1998) "Motion of a sphere near planar confining boundaries in a Brinkman medium." *J. Fluid Mech.* **375:** 265-296.

19. Feng, J. and Weinbaum, S. (2000) "Lubrication theory in highly compressible porous media: the mechanics of skiing, from red cells to humans." *J. Fluid Mechanics* **422**(1): 281-317.

20. Flanagan, A. M. and Chambers, T. J. (1992). "Stimulation of bone nodule formation in vitro by prostaglandins E1 and E2." *Endocrinology* **130**(1): 443-448.

21. Florian, J. A., Kosky, J. R., Ainslie, K., Pang, Z., Dull, R. O. and Tarbell, J. M. (2003) "Heparan sulfate proteoglycan is a mechanosensor on endothelial cells." *Circ. Res.* **93**(10): e136-e142.

22. Forwood, M. R. (1996). "Inducible cyclo-oxygenase (COX-2) mediates the induction of bone formation by mechanical loading in vivo." *J Bone Miner Res* **11**(11): 1688-1693.

23. Frisch-Fay, R. (1962) *Flexible Bar*. Washington, D. C., Butterworths Inc.

24. Fritton, S. P., McLeod, K. J. and Rubin, C. T. (2000) "Quantifying the strain history of bone: spatial uniformity and self-similarity of low-magnitude strains." *J. Biomech.* **33**(3): 317-325.

25. Genetos, D. (2005). ATP release and purinergic mechanotransduction in bone cells. Ph.D thesis at College of Medicine, The Pennsylvania State University.

26. Gere, J. M. and Timoshenko, S. P. (1990) *Mechanics of material*. Boston, PWS-KENT Publishing Company.

27. Gittes, F., Mickey, B., Nettleton, J. and Howard, J. (1993) "Flexural rigidity of microtubules and actin filaments measured from thermal fluctuations in shape." *J. Cell Biol.* **120**(4): 923-934.

28. Guilak, F., Ratcliffe, A. and Mow, V. C. (1995) "Chondrocyte deformation and local tissue strain in articular cartilage: a confocal microscopy study." *J. Orthop. Res.* **13**(3): 410-421.

29. Guo, P., Weinstein, A. M. and Weinbaum, S. (2000) "A hydrodynamic mechanosensory hypothesis for brush border microvilli." *Am. J. Physiol. Renal. Physiol.* **279**(4): F698-F712.

30. Han, Y., Ganatos, P. and Weinbaum, S. (2005) "Transmission of steady and oscillatory fluid shear stress across epithelial and endothelial surface layers." *Phys. of Fluids* **17**: 031508(1-13).

31. Han, Y., Cowin, S. C., Schaffler, M. B. and Weinbaum, S. (2004) "Mechanotransduction and strain amplification in osteocyte cell processes." *Proc. Natl. Acad. Sci. USA* **100**(13): 7988-7995.

32. Han, Y., Weinbaum, S., Spaan, J. A. and Vink, H. (2006) "Large deformation Analysis of the elastic recoil of the core protein in the endothelial glycocalyx." the 50th anniversary issue for *J. Fluid Mechanics*.

33. Harada, S. I., Balena, R., Rodan, G. A. and Rodan, S. B. (1995). "The role of prostaglandins in bone formation." *Connect Tissue Res.* **31**(4): 279-82.

34. Helmlinger, G., Berk, B. C. and Nerem, R. M. (1995) "Calcium responses of endothelial cell monolayers subjected to pulsatile and steady laminar flow differ." *Am. J. Physiol.* **269**(2 Pt 1): C367-C375.

35. Henry, C. B. and Duling, B. R. (2000) "TNF-alpha increases entry of macromolecules into luminal endothelial cell glycocalyx." *Am. J. Physiol. Heart. Circ. Physiol.* **279**(6): H2815-H2823.

36. Hillsley, M. V. and Tarbell, J. M. (2002) "Oscillatory shear alters endothelial hydraulic conductivity and nitric oxide levels." *Biochem. Biophys. Res. Commun.* **293**(5): 1466-1471.

37. Hu, J., Xu, Y., Schappert, K., Harrington, T., Wang, A., Braga, R., Mogridge, J. and Friesen, J. D. (1994) "Mutational analysis of the PRP4 protein of Saccharomyces cerevisiae suggests domain structure and snRNP interactions." *Nucleic Acids Res.* **22**(9): 1724-1734.

38. Hu, X., Adamson, R. H., Liu, B., Curry, F. E. and Weinbaum, S. (2000) "Starling forces that oppose filtration after tissue oncotic pressure is increased." *Am. J. Physiol. Heart Circ. Physiol.* **279**(4): H1724-H1736.

39. Hung, C. T., Pollack, S. R., Reilly, T. M. and Brighton, C. T. (1995) "Real-time calcium response of cultured bone cells to fluid flow." *Clin. Orthop.* **313**: 256-269

40. Ihrcke, N. S., Wrenshall, L. E., Lindman, B. J. and Platt, J. L. (1993) "Role of heparan sulfate in immune system-blood vessel interactions." *Immunol. Today* **14**(10): 500-505.

41. Jee, W. S., Ueno, K., Deng, Y. P. and Woodbury, D. M. (1985). "The effects of prostaglandin E_2 in growing rats: increased metaphyseal hard tissue and cortico-endosteal bone formation." *Calcif. Tissue Int.* **37**(2): 148-157.

42. Jiang, J. X. and Cherian, P. P. (2003) "Hemichannels formed by connexin 43 play an important role in the release of prostaglandin E(2) by osteocytes in response to mechanical strain." *Cell Commun. Adhes.* **10**(4-6): 259-264.

43. Keller, J., Klamer, A., Bak, B. and Suder, P. (1993). "Effect of local prostaglandin E2 on fracture callus in rabbits." *Acta Orthop. Scand.* **64**(1): 59-63.

44. Kishino, A. and Yanagida, T. (1988) "Force measurements by micromanipulation of a single actin filament by glass needles." *Nature* **334**(6177): 74-76.

45. Klein-Nulend, J., Burger, E. H., Semeins, C. M. Raisz, L. G. and Pileam, C. C. (1997) "Pulsating fluid flow stimulates prostaglandin release and inducible prostaglandin G/H synthase mRNA expression in primary mouse bone cells. " *J. Bone Miner. Res.* **12**: 45-51.

46. Klein-Nulend, J., van der Plas, A., Semeins, C. M., Ajubi, N. E., Frangos, J. A., Nijweide, P. J. and Burger, E. H. (1995). "Sensitivity of osteocytes to biomechanical stress in vitro." *Faseb J.* **9**(5): 441-445.

47. Knothe Tate, M. L. (2001). Bone Biomechanics. *Bone Biomechanics*. S. C. Cowin. Boca Raton, Florida, CRC Press.

48. Knothe Tate, M. L. (2001) "Mixing mechanisms and net solute transport in bone." *Ann. Biomed. Eng.* **29**(9): 810-811; author reply 812-816.

49. Ku, D. N., Giddens, D. P., Zarins, C. K. and Glagov, S. (1985) "Pulsatile flow and atherosclerosis in the human carotid bifurcation. Positive correlation between plaque location and low oscillating shear stress." *Arteriosclerosis* **5**(3): 293-302.

50. Latta, H., Maunsbach, A. and Madden, S. (1961) "Cilia in different segments of the rat nephron." *J. Biophys. Biochem. Cytol.* **11**: 248-252.

51. Liron, N. and Mochon, S. (1976) "The discrete-cilia approach to propulsion of ciliated micro-organisms." *J. Fluid Mechanics* **75**: 593 - 607.

52. Liron, N. and Shahar, R. (1978) "Stokes flow due to a Stokeslet in a pipe." *J. Fluid Mechanics* **162**: 157-170.

53. Liu, W., Xu, S., Woda, C., Kim, P., Weinbaum, S. and Satlin, L. M. (2003) "Effect of flow and stretch on the [Ca2+]i response of principal and intercalated cells in cortical collecting duct." *Am. J. Physiol. Renal Physiol.* **285**(5): F998-F1012.

54. Luft, J. H. (1966) "Fine structures of capillary and endocapillary layer as revealed by ruthenium red." *Fed. Proc.* **25**(6): 1773-1783.

55. Matsudaira, P. T. and Burgess, D. R. (1982) "Organization of the cross-filaments in intestinal microvilli." *J. Cell. Biol.* **92**(3): 657-664.

56. Michel, C. C. (1983). The effects of certain proteins on capillary permeability to fluid and macromolecules. *Pathogenicity of Cationic Proteins*. P. P. Lambert, P. Bergmann and R. Beauwens. New York, Raven Press**:** 125–140.

57. Michel, C. C. (1997) "Starling: the formulation of his hypothesis of microvascular fluid exchange and its significance after 100 years." *Exp. Physiol.* **82**(1): 1-30.

58. Mooseker, M. S. and Tilney, L. G. (1975) "Organization of an actin filament-membrane complex. Filament polarity and membrane attachment in the microvilli of intestinal epithelial cells." *J. Cell. Biol.* **67**(3): 725-743.

59. Mulivor, A. W. and Lipowsky, H. H. (2004) "Inflammation- and ischemia-induced shedding of venular glycocalyx." *Am. J. Physiol. Heart Circ. Physiol.* **286**(5): H1672-H1680.

60. Nagata, T., Kaho, K., Nishikawa, S., Shinohara, H., Wakano, Y. and Ishida, H. (1994). "Effect of prostaglandin E2 on mineralization of bone nodules formed by fetal rat calvarial cells." *Calcif. Tissue Int.* **55**(6): 451-457.

61. Owan, I., Burr, D. B., Turner, C. H., Qiu, J., Tu, Y., Onyia, J. E. and Duncan, R. L. (1997) "Mechanotransduction in bone: osteoblasts are more responsive to fluid forces than mechanical strain." *Am. J. Physiol.* **273**(3 Pt 1): C810-C815.

62. Pfaller, W. and Klima, J. (1976) "A critical reevaluation of the structure of the rat uriniferous tubule as revealed by scanning electron microscopy." *Cell Tissue Res.* **166**(1): 91-100.

63. Praetorius, H. A. and Spring, K. R. (2001) "Bending the MDCK cell primary cilium increases intracellular calcium." *J. Membr. Biol.* **184**(1): 71-79.

64. Pries, A. R., Secomb, T. W. and Gaehtgens, P. (2000) "The endothelial surface layer." *Pflugers. Arch.* **440**(5): 653-666.

65. Pries, A. R., Secomb, T. W., Jacobs, H., Sperandio, M., Osterloh, K. and Gaehtgens, P. (1997) "Microvascular blood flow resistance: role of endothelial surface layer." *Am. J. Physiol.* **273**(5 Pt 2): H2272-2279.

66. Qiu, Y. and Tarbell, J. M. (2000) "Numerical simulation of pulsatile flow in a compliant curved tube model of a coronary artery." *J. Biomech. Eng.* **122**(1): 77-85.

67. Reich, K. M. and Frangos, J. A. (1991) "Effect of flow on prostaglandin E2 and inositol trisphosphate levels in osteoblasts." *Am. J. Physiol.* **261**(3 Pt 1): C428-C432.

68. Reilly, G. C., Haut, T. R., Yellowley, C. E., Donahue, H. J. and Jacobs, C. R. (2003) "Fluid flow induced PGE2 release by bone cells is reduced by glycocalyx degradation whereas calcium signals are not." *Biorheology* **40**(6): 591-603.

69. Rubin, C. T. and Lanyon, L. E. (1984) "Regulation of bone formation by applied dynamic loads." *J. Bone Joint Surg. Am.* **66**(3): 397-402.

70. Rubin, C. T. and Lanyon, L. E. (1985) ″Regulation of bone mass by mechanical strain magnitude.″ Calcif. Tissue Int. **37**: 411-417.

71. Sangani, A. S. and Acrivos, A. (1982) "Slow flow past periodic arrays of cylinders with application to heat transfer." *Int. J. Multiphase Flow* **8**(3): 193-206.

72. Sangani, A. S. and Acrivos, A. (1982) "Slow flow through a periodic arrays of spheres." *Int. J. Multiphase Flow* **8**(4): 343-360.

73. Schmidt-Nielsen, B. and Graves, B. (1982) "Changes in fluid compartments in hamster renal pailla due to peristalsis in the pelvic wall." *Kidney Int.* **22**: 613-625.

74. Schwartz, E. A., Leonard, M. L., Bizios, R. and Bowser, S. S. (1997) "Analysis and modeling of the primary cilium bending response to fluid shear." *Am. J. Physiol.* **272**(1 Pt 2): F132-F138.

75. Secomb, T. W. and El-Kareh, A. W. (2001) "A theoretical model for the elastic properties of very soft tissues." *Biorheology* **38**(4): 305-317.

76. Secomb, T. W., Hsu, R. and Pries, A. R. (1998) "A model for red blood cell motion in glycocalyx-lined capillaries." *Am. J. Physiol.* **274**(3 Pt 2): H1016-H1022.

77. Secomb, T. W., Hsu, R. and Pries, A. R. (2001) "Effect of the endothelial surface layer on transmission of fluid shear stress to endothelial cells." *Biorheology* **38**(2-3): 143-150.

78. Secomb, T. W., Hsu, R. and Pries, A. R. (2001) "Motion of red blood cells in a capillary with an endothelial surface layer: effect of flow velocity." *Am. J. Physiol. Heart Circ. Physiol.* **281**(2): H629-H636.

79. Shin, D. and Athanasiou, K. (1999) "Cytoindentation for obtaining cell biomechanical properties." *J. Orthop. Res.* **17**(6): 880-890.

80. Smalt, R., Mitchell, F. T., Howard, R. L. and Chambers, T. J. (1997) "Induction of NO and prostaglandin E2 in osteoblasts by wall-shear stress but not mechanical strain." *Am. J. Physiol.* **273**(4 Pt 1): E751-E758.

81. Squire, J. M., Chew, M., Nneji, G., Neal, C., Barry, J. and Michel, C. (2001) "Quasi-periodic substructure in the microvessel endothelial glycocalyx: a possible explanation for molecular filtering?" *J. Struct. Biol.* **136**(3): 239-255.

82. Stace, T. M. and Damiano, E. R. (2001) "An electrochemical model of the transport of charged molecules through the capillary glycocalyx." *Biophys. J.* **80**(4): 1670-1690.

83. Sugihara-seki, M. (2005) ″A fluid-mechanical study for solute transport across the endothelial surface glycocalyx.″ *2005 Summer Bioengineering Conference of the ASME Bioengineering Division*, Vail, CO, USA, June 22-26.

84. Tanaka-Kamioka, K., Kamioka, H., Ris, H. and Lim, S. S. (1998) "Osteocyte shape is dependent on actin filaments and osteocyte processes are unique actin-rich projections." *J. Bone Miner. Res.* **13**(10): 1555-1568.

85. Thi, M. M., Kojima, T., Cowin, S. C., Weinbaum, S. and Spray, D. C. (2003) "Fluid shear stress remodels expression and function of junctional proteins in cultured bone cells." Am. J. Physiol. Cell Physiol. **284**(2): C389-403.

86. Thi, M. M., Tarbell, J. M., Weinbaum, S. and Spray, D. C. (2004) "The role of the glycocalyx in reorganization of the actin cytoskeleton under fluid shear stress: a "bumper-car" model." *Proc. Natl. Acad. Sci. USA* **101**(47): 16483-16488.

87. van den Berg, B. M., Vink, H. and Spaan, J. A. (2003) "The endothelial glycocalyx protects against myocardial edema." *Circ. Res.* **92**(6): 592-594.

88. Vink, H., Constantinescu, A. A. and Spaan, J. A. (2000) "Oxidized lipoproteins degrade the endothelial surface layer : implications for platelet-endothelial cell adhesion." *Circulation* **101**(13): 1500-1502.

89. Vink, H. and Duling, B. R. (1996) "Identification of distinct luminal domains for macromolecules, erythrocytes, and leukocytes within mammalian capillaries." *Circ. Res.* **79**(3): 581-589.

90. Vink, H. and Duling, B. R. (2000) "Capillary endothelial surface layer selectively reduces plasma solute distribution volume." *Am. J. Physiol. Heart Circ. Physiol.* **278**(1): H285-H289.

91. Vink, H., Duling, B. R. and Spaan, J. A. E. (1999) "Mechanical properties of the endothelial surface layer (Abstract)." *FASEB J.* **13**: A11.

92. Vink, H., Wieringa, P. A. and Spaan, J. A. (1995) "Evidence that cell surface charge reduction modifes capillary red cell velocity-flux relationships in hamster cremaster muscle." *J. Physiol.* **489**(Pt 1): 193-201.

93. Volkmann, N., DeRosier, D., Matsudaira, P. and Hanein, D. (2001) "An atomic model of actin filaments cross-linked by fimbrin and its implications for bundle assembly and function." *J. Cell. Biol.* **153**(5): 947-956.

94. Wang, L., Ciani, C., Doty, S. B. and Fritton, S. P. (2004) "Delineating bone's interstitial fluid pathway in vivo." *Bone* **34**(3): 499-509.

95. Weinbaum, S. (1998) "1997 Whitaker Distinguished Lecture: Models to solve mysteries in biomechanics at the cellular level; a new view of fiber matrix layers." *Ann. Biomed. Eng.* **26**(4): 627-643.

96. Weinbaum, S., Cowin, S. C. and Zeng, Y. (1994) "A model for the excitation of osteocytes by mechanical loading-induced bone fluid shear stresses." *J. Biomech.* **27**(3): 339-360.

97. Weinbaum, S., Guo, P. and You, L. (2001) "A new view of mechanotransduction and strain amplification in cells with microvilli and cell processes." *Biorheology* **38**(2-3): 119-142.

98. Weinbaum, S., Zhang, X., Han, Y., Vink, H. and Cowin, S. C. (2003) "Mechanotransduction and flow across the endothelial glycocalyx." *Proc. Natl. Acad. Sci. USA* **100**(13): 7988-7995.

99. Welling, L. W. and Welling, D. J. (1975) "Surface areas of brush border and lateral cell walls in the rabbit proximal nephron." *Kidney Int.* **8**(6): 343-348.

100. Wiederhielm, C. A. and Black, L. L. (1976) "Osmotic interaction of plasma proteins with interstitial macromolecules." *Am. J. Physiol.* **231**(2): 638-641.

101. Williams, J. L., Iannotti, J. P., Ham, A., Bleuit, J. and Chen, J. H. (1994) "Effects of fluid shear stress on bone cells." *Biorheology* **31**:163-170.

102. Wu, R. and Weinbaum, S. (1982) "On the development of fluid trapping beneath deformable fluid-cell membranes." *J. Fluid Mech.* **121**: 315-343.

103. You, L., Cowin, S. C., Schaffler, M. B. and Weinbaum, S. (2001) "A model for strain amplification in the actin cytoskeleton of osteocytes due to fluid drag on pericellular matrix." *J. Biomech.* **34**(11): 1375-1386.

104. You, L. D., Weinbaum, S., Cowin, S. C. and Schaffler, M. B. (2004) "Ultrastructure of the osteocyte process and its pericellular matrix." *Anat. Rec.* **278A**(2): 505-513.

105. You, J., Yellowley, C. E., Donahue, H. J., Zhang, Y., Chen, Q. and Jacobs, C. R. (2000) "Substrate deformation levels associated with routine physical activity are less stimulatory to bone cells rela tive to loading-induced oscillatory fluid flow." *J. Biomech. Eng.* **122**(4): 387-393.

106. Zeng, Y., Cowin, S. C. and Weinbaum, S. (1994) "A fiber matrix model for fluid flow and streaming potentials in the canaliculi of an osteon." *Ann. Biomed. Eng.* **22**(3): 280-292.

107. Zhao, Y., Chien, S. and Weinbaum, S. (2001) "Dynamic contact forces on leukocyte microvilli and their penetration of the endothelial glycocalyx." *Biophys. J.* **80**(3): 1124-1140.